Phase transformations and crystalline quality of $CuInS_2$ thin films

Dissertation

zur
Erlangung des Doktorgrades
der Naturwissenschaften
(Dr. rer. nat.)

dem
Fachbereich Physik
der Philipps-Universität Marburg
vorgelegt von

Eveline Rudigier

aus Mainz

Marburg / Lahn 2004

Vom Fachbereich Physik der Philipps-Universität Marburg als Dissertation

angenommen am: 20.10.2004

Erstgutachter: Prof. Dr. W. Fuhs

Zweitgutachter: Prof. Dr. H. Ries

Tag der mündlichen Prüfung: 10.11.2004

Kurzreferat

Dünnschichtkonzepte bieten eine interessante Alternative zu herkömmlichen Solarzellentechnologien, da solchen Konzepten erhebliches Potential eingeräumt wird, kostengünstige, großflächige und effiziente Energieumwandlung zu gewährleisten. Zumeist wird ein solches Dünnschichtkonzept mit Heterosolarzellen realisiert. Die derartigen Solarzellen zugrundeliegende Struktur besteht im wesentlichen aus einer für das Sonnenspektrum weitgehend transparenten, hoch n-dotierten Fensterschicht in Kombination mit einem hochabsorbierenden, p-leitenden Absorber. Insbesondere Verbindungshalbleiter auf der Basis von Cu-Chalkopyriten sind mittlerweile als Absorberschichten in solchen Dünnschichtsolarzellen etabliert, da diese eine direkte Bandlücke aufweisen und aufgrund ihres Absorptionskoeffizienten das Sonnenlicht in einer nur wenige Mikrometer dicken Schicht absorbieren können. Insbesondere die Verwendung des Verbindungshalbleiters $CuInS_2$ ist für photovoltaische Anwendungen vielversprechend, da dieses Material zum einen keine Elemente wie beispielsweise Se enthält, die aus Umweltgesichtspunkten bedenklich sind, und zum anderen eine dem Sonnenspektrum optimal angepasste Bandlücke (E_g = 1.5 eV) aufweist. Im Labormaßstab wurden für solche $CuInS_2$-basierten Solarzellen bereits Wirkungsgrade von bis zu 12 % erreicht.

Für die Herstellung solcher $CuInS_2$ Absorberschichten wurde ein für die industrielle Produktion relevanter sequentieller Prozess angewandt. Im Kernstück dieses Prozesses werden sogenannte Cu-In Vorläuferschichten in einer reaktiven Schwefelatmosphäre angelassen. Dabei sind die strukturelle Qualität der fertigen Schichten sowie die elektrischen Eigenschaften der späteren Solarzellen wesentlich von den Präparationsbedingungen abhängig. Von besonderer Bedeutung während des Wachstums dieser Schichten sind das gewählte Cu/In-Verhältnis der Vorläuferschichten, die Temperatur während der Sulfurisierung, das Einbringen von Dotierelementen und die resultierende Schichtdicke. Die Optimierung solcher Prozessparameter im Hinblick auf die Funktionsweise der späteren Solarzelle beruht allerdings im wesentlichen auf empirischen Erfahrungen.

In-situ Charakterisierungsmethoden versprechen nun ein tieferes Verständnis solcher Einflussparameter. Im Rahmen dieser Arbeit konnte erstmals Ramanspektroskopie als eine solche *in-situ* Charakterisierungsmethode etabliert werden. Diese Methode ermöglicht unter anderem die Detektion einer Defektphase des $CuInS_2$, die sogenannte CuAu-Ordnung. Außerdem ist Ramanspektroskopie sensitiv für oberflächennahe Schichten, welche von besonderem Interesse sind, da diese mit der Region der fertigen Solarzellen korrespondieren, welche den Wirkungsgrad der Energiekonversion wesentlich mitbestimmt. Mit Röntgenbeugung (XRD) kann hingegen das gesamte Volumen der entsprechenden Schichten untersucht werden. Die Kombination dieser sich ergänzenden Methoden gewährleistet einen Gesamtüberblick über das Schichtwachstum. Neben der Identifikation der während des Wachstums auftretenden Phasen bietet Ramanspektroskopie die Möglichkeit, die strukturelle Qualität von $CuInS_2$ Schichten anhand der Linienform der auftretenden Ramanbanden zu untersuchen. So ist beispielsweise eine Verbreiterung der Ramanbande mit der in der Schicht vorhandenen Defektdichte verbunden, wie in dieser Arbeit erstmals gezeigt werden konnte.

Im folgenden seien die wichtigsten Ergebnisse dieser Arbeit kurz zusammengefasst:

- Die *in-situ* Untersuchungen des Kristallwachstums ergeben signifikant abweichende Wachstumspfade in Abhängigkeit des gewählten Cu/In-Verhältnisses und des Dotierens mit Natrium.
- Es wurde erstmals die experimentelle Evidenz erbracht, dass unabhängig von der Komposition das Wachstum von $CuInS_2$ mit der CuAu-Ordnung beginnt, während die Bildung der Chalkopyritordnung erst bei deutlich höheren Temperaturen stattfindet, wohingegen der Anteil der sich bildenden Chalkopyritordnung abhängig von der Komposition ist. Diese Ergebnisse konnten in einem Modell, das den Einfluss des Schwefeleinbaus in die Schicht beschreibt, zusammenfassend beschrieben werden.
- Erstmals konnte der Einfluss von Natrium als Dotiermaterial auf den Wachstumspfad direkt untersucht werden. Die Rolle des Natriums konnte ebenfalls anhand des oben genannten Modells erklärt werden.
- Aus den Temperexperimenten konnte der Grüneisenparameter des $CuInS_2$ berechnet werden.

- Die Ramanuntersuchungen an verschiedenartig präparierten Proben ergaben eine unterschiedliche Linienbreite der Hauptramanmode des $CuInS_2$. Dies konnte mit dem für $CuInS_2$ erstmals verifizierten Modell des sogenannten Phonon-Confinements in Einklang gebracht werden. Auf diesem Modell basierende Annahmen konnten mit dem Auftreten entsprechender Defektdichten in Zusammenhang gesetzt werden.
- Die Kombination von *ex-situ* Ramanmessungen und Messungen der elektrischen Eigenschaften von $CuInS_2$-basierten Solarzellen zeigte einen deutlichen Zusammenhang: je breiter die Ramanlinien der Hauptmode, desto schlechter die elektrischen Eigenschaften der Solarzellen. Ebenfalls konnte in Abhängigkeit der Verbreiterung der Ramanlinien eine Änderung des Rekombinationsmechanismus in den entsprechenden Solarzellen identifiziert werden. Es wurde versucht, diese Ergebnisse mit einem Rekombinationsmodell zu erklären, welches die strukturellen und elektrischen Eigenschaften miteinander verbindet.
- Zusätzlich konnte an dieser Stelle der direkte Einfluss der Prozessparameter bei der Herstellung solcher $CuInS_2$-basierten Schichten auf deren strukturelle Qualität untersucht werden.

Im Rahmen dieser Arbeit wurden wesentliche Erkenntnisse bezüglich der Strukturbildung des $CuInS_2$ gewonnen. Außerdem konnte der Einfluss der auf empirischen Erfahrungen beruhenden Prozessparameter auf die strukturelle Qualität der Absorberschichten deutlich nachgewiesen werden. Die erarbeitete Korrelation zwischen der strukturellen Qualität der Absorberschichten und den Solarzelleneigenschaften zeigt das hohe Potential der Ramanspektroskopie, als Prozesskontrolle in einer Fertigungslinie. Dies wird zum gegenwärtigen Zeitpunkt evaluiert. Für die Zukunft wäre es wünschenswert, die in den Schichten auftretenden Defekte zu identifizieren und damit die Ergebnisse dieser Arbeit zu vervollständigen.

Acknowledgements

At this point I would like to say thank you to all the people who have generously given their time throughout this thesis.

First of all I would like to thank Prof. Dr. W. Fuhs for his ongoing support and many helpful suggestions especially during the last months.
I would also like to thank Prof. Dr. H. Ries for his great interest in this work and for reviewing this thesis.
Special thanks to Dr. Roland Scheer for giving me the opportunity to realize this thesis in his group at the Hahn-Meitner Institut, his advice and encouragement and for all the valuable discussions. Without his guidance this work would not be what it is.
Special thanks also to Dr. I. Luck for introducing me into the wide field of chalcopyrite solar cells and the great time in our office.
Many thanks to our coworkers in Barcelona, especially Beatriz Barcones and Jacobo Alvarez-Garcia for many helpful discussions and sharing the enthusiasm when realizing the first *in-situ* Raman experiments.
Jovana Djordevic (Turbo2), Dr. Christian Pietzker and Dr. Felix Porsch thank you for the hours and hours together at beamline F3 in the HasyLab.
A big thank you to all the members of the department SE3 at the Hahn-Meitner Institut for the nice and convenient working atmosphere. Without the help and experiences of Jo Klaer, Ernst Müller, Kerstin Jacob, Bianca Bunn, Petra Pollow, and Norbert Blau the sample preparation would have last for ever. Not to mention Martin Wilhelm for his great support at the SEM, Joachim Liebig and Axel Boden for their technical support, Andrea Gibhardt the best secretary on earth and Tobias Enzenhofer and Jacob Lauche for their helpfulness. Many thanks also to Dr. Susanne Siebentritt and Dr. Reiner Klenk for their helpful discussions and to Carola Kelch, Michael Kirsch and Tim Münchenberg for the buffer and window layer preparation.
Big thanks to Jovana Djordjevic and Steffen Schuler for the fruitful discussions about death and life of chalcopyrites, Joachim Reiss, Oskar Hallatschek, Stefan Mechler, Wolfgang Eisele, Markus Strobl, Chris Milne, Christian Kaufmann, the Spanish

community, Niklas Rega, Olga Papathanasiou, Alex Meeder, Anne Rumberg and Nico Meyer for all the fun at and after work and to Jan Hinze for all the sunshine.

A very big thank you to Stefan Mechler, Silke Kister, Torsten Voigt, Jovana Djordjevic and Steffen Schuler for carefully reading this thesis and for the critical remarks.

My deepest thanks to my family for their generous support, encouragement and patience.

Finally, big thanks to Torsten for bearing my moods and all my friends for the never ending encouragement.

Contents

5 Real-time structural analysis on the growth of Cu-In-S thin films 65

6 Relating structural material properties and electric device properties of $CuInS_2$-based thin film solar cells 103

Chapter 1

Introduction

In recent years, due to the growing interest in alternative energies, photovoltaics has become an active field for research. Today's commercial solar cells are predominantly fabricated on the basis of crystalline silicon wafers. Economically, thin film solar cells offer an interesting alternative [1]. Here, technology based on amorphous silicon is already established on the market, while thin film solar cells based on CdTe and $Cu(In,Ga)(S,Se)_2$ are in the pilot-line stage [2].

Cu-chalcopyrite semiconductor materials are used as absorber layers in heterojunction solar cell devices [3]. These materials exhibit a direct band gap and absorb the sunlight within a layer of a few microns thickness due to their high absorption coefficients. In the laboratory a conversion efficiency as high as 19 % has been achieved with $Cu(In,Ga)(S,Se)_2$–based thin film solar cells [4]. Industrially fabricated modules of this type have been realized with an efficiency up to 12.7 % [5]. Compared to the knowledge accumulated on classical semiconductors such as silicon, the understanding of the physical properties of chalcopyrite materials is rather limited.

The chalcopyrite semiconductor $CuInS_2$ (CIS) is particularly promising for photovoltaic applications as it is Se-free and its band gap (1.5 eV) is well adapted to the solar spectrum. Conversion efficiencies above 12 % [6] on a laboratory scale and up to 10.2 % [7] on a mini-module scale have been demonstrated. Recently, the installation of a pilot-line using this technology has been announced for commercial solar modules [8].

In $CuInS_2$-based thin film solar cells the photo collection and charge carrier generation mainly occurs in the p-absorber ($CuInS_2$), whereas the n-type layer is transparent and only needed to form the pn-junction. The $CuInS_2$-based absorber layers studied within this thesis are fabricated in a sequential process. In such a process the Cu/In metal stacks, so-called precursor layers, are annealed in sulfur atmosphere. Important parameters for the preparation of these absorbers are the

Cu/In ratio of the precursor layers, the peak temperature during the sulfurization process and the final thickness of the absorber layers.

The performance of $CuInS_2$-based photovoltaic devices is currently limited by the open circuit voltage V_{oc}. This value is significantly below the theoretical limit calculated for an ideal solar cell with a direct band gap of 1.5 eV. In order to overcome this limitation recent research has focused on modifications, such as the preparation of $CuInS_2$ thin films with different Cu/In-ratios and with different doping elements. In the course of these investigations it has been found that both, different Cu/In-ratios as well as the presence of doping elements, have an influence on the structural and electronic properties [6,9]. For example, Cu-rich prepared $CuInS_2$ absorber layers show a good device performance in contrast to Cu-poor prepared films. Theoretical calculations on polytypes and defect structures of chalcopyrites [10,11] motivated the investigation of those crystalline phases in order to explain the dependence of the device performance on the composition. Previously, it has been found that in Cu-poor prepared $CuInS_2$ films the so-called CuAu-phase is highly dominating. It is discussed if the CuAu phase induces a deterioration of the solar cell performance [12]. Nevertheless, a promising approach to use Cu-poor prepared absorbers has been introduced by Watanabe et al. [13], who showed that the incorporation of sodium in those films results in a significant improvement of the solar cell conversion efficiency. Moreover, it has been found for epitaxial $CuInSe_2$ films, the selenide analogue to $CuInS_2$, that incorporated sodium leads to a suppression of detrimental structural phases within the films [14].

At present the understanding of this material with respect to these variations, in particular the role of sodium during the growth, is far from being complete. In addition, device development of chalcopyrite-based solar cells is often based on empirical experiences. Detailed knowledge of the structural properties and their dependence on the different process parameters is required for a classification of those empirical experiences into an overall picture of the functionality of $CuInS_2$-based thin film solar cells.

The main focus of this thesis is on the structural analysis of $CuInS_2$ films. Real-time experiments during the sulfurization of precursor layers with different Cu/In-ratios have been performed as well as studies on the influence of sodium on the growth of Cu-poor prepared Cu/In precursor layers. Energy dispersive X-ray diffraction (EDXRD) as a bulk sensitive method and Raman spectroscopy as a surface sensitive method have been combined in *in-situ* experiments. While real-time X-ray diffraction (XRD) has been introduced before, it was one goal of this work to introduce Raman spectroscopy as an additional *in-situ* investigation method for chalcopyrite growth studies. One advantage of Raman spectroscopy is that the different crystalline phases of $CuInS_2$, such as the chalcopyrite- and the CuAu-phase are observable [15]. Therefore, the growth of $CuInS_2$ films especially with respect to these phases has been investigated in detail.

Electronic defects in the absorbing layer determine the energy conversion efficiency of a heterojunction solar cell. For an industrial production application it is important to relate defect densities to specific process parameters and to the performance of the solar cells. Raman spectroscopy is well suited to assess the crystal quality of semiconductor materials [16]. The line shape of a Raman band has been related to the defect density within the films. This defect density manifests itself in a coherent volume of scatterers, which gives rise to an activation of non-centered phonons in the films and leads to an asymmetric line broadening [17,18].

In this work not only single $CuInS_2$ layers but also completed solar cells have been investigated *ex-situ* with Raman spectroscopy. It will be shown that the spectroscopic line shape of an intense $CuInS_2$-Raman band correlates with the electric properties of the completed devices. These results demonstrate the possibility to introduce Raman spectroscopy as an in-line process control for solar cell fabrication. Raman spectroscopy allows the investigation of the structural quality of the absorber layers directly after their preparation without the need of completing the whole device in order to assess its quality. Furthermore, as with Raman spectroscopy the relevant regions of the absorber layers can be investigated, it will be shown, how the structural quality is related to the recombination mechanism of the devices.

This thesis is divided into the following chapters:

Chapter 2 gives a brief introduction into the theory of elastic and inelastic light scattering in solids. Additionally, the basic aspects of Raman spectroscopy and EDXRD are presented. As the understanding of Raman spectroscopy in solids and the assignment of the Raman bands require group theory, a short section dealing with the basics of group theory is included.

Chapter 3 is concerned with the vibrational properties of Cu-based chalcopyrites with focus on $CuInS_2$. A detailed deduction of the specific movements of the single atoms in the chalcopyrite unit cell for the specific Raman modes is presented. The occurring polytypes of chalcopyrites are briefly discussed. After that, a short introduction to thin film solar cells is followed by a discussion of the dependence of the open circuit voltage on the band gap of the absorber in terms of dominating recombination mechanisms in heterojunction diodes.

Chapter 4 depicts the general design of a heterojunction solar cell and the device structure of chalcopyrite solar cells. This is followed by a short description of the sequential process steps for solar cells as used within this work. Additionally, the experimental setups for the different *in-situ* investigation methods are presented.

Chapter 5 presents structural *in-situ* experiments. These are important for a detailed understanding of the growth processes. At first *in-situ* Raman experiments of completed absorber layers are presented with respect to the temperature-induced line shift and increase of the line width. Differences between differently prepared absorber layers are pointed out. Then, the sulfurization of pure Cu and In layers is presented as Cu-S and In-S binaries may occur as intermediate phases during the growth of $CuInS_2$. This is followed by the investigation of the growth of $CuInS_2$ thin films simultaneously with *in-situ* EDXRD and *in-situ* Raman spectroscopy. Here, the influence of the precursor composition as well as the effect of sodium is discussed with regard to the phase transformations. Furthermore, the role of the CuAu-phase during the growth is investigated.

Chapter 6 reports on the investigation of $CuInS_2$-based heterojunction solar cells. This chapter especially deals with the question how the structural properties influence the device performance on the one hand and the recombination mechanism on the other hand. The structural quality of the films has been investigated with *ex-situ* Raman experiments and PL measurements, while the devices have been characterized by means of jV-characteristics and spectral response. Additionally, the influence of the process parameters on the structural properties is presented.

Chapter 7 summarizes the main results and conclusions of this work and closes with an outlook.

Chapter 2

Structural Investigation Methods for the Characterization of $CuInS_2$ Thin Films

The purpose of the following chapter is to give a brief introduction into the theoretical aspects of Raman Spectroscopy and Energy Dispersive X-Ray Diffraction (EDXRD). These two methods have been chosen to study the structural properties of chalcopyrite thin films as Raman spectroscopy allows the investigation of the near surface region, while EDXRD is a bulk-sensitive method. The information depth of Raman spectroscopy is due to the absorption coefficient of $CuInS_2$ and depends on the chosen excitation wavelength. Besides accurate ex-situ analysis, the sulfurization process of $CuInS_2$ films can be studied in real-time with both methods.

The first part of this chapter is focused on the macroscopic theory of the Raman effect for solids. The inelastic light scattering process is discussed by developing an expression for the polarization of the medium and for the scattering cross section. The latter leads to selection rules for the Raman effect, which can be determined by the use of group theory. Therefore, a brief introduction into the notations of group theory will be given as well as an outline for the identification of the $CuInS_2$ Raman modes. Furthermore, phenomena, such as temperature and stress effects are discussed with regard to the later shown experiments. The second part of this chapter gives an insight into the basics of X-ray scattering in crystalline solids.

2.1 Raman Spectroscopy

For light scattering processes the elastic one is the most dominant, well-known as Rayleigh scattering. During elastic light scattering the frequency of the scattered light is equal to the frequency of the incident light, no matter if the medium is in an excited or in its ground state. During his investigations Rayleigh found the fundamental correlation for the elastic scattering cross section $\sigma_S \propto \nu^4 \propto \lambda^{-4}$.

In 1928 Raman succeeded in observing experimentally inelastic light scattering, the so-called **Raman effect** [19]. Already in 1923 Smekal [20] predicted this process and formulated a theoretical description. Inelastic scattering processes are two-photon events that involve the simultaneous annihilation and creation of photons [21]. In contrast to the elastic scattering process it is characteristic for the inelastic case that the energy of the incident photon ($h\omega_i$) is different from the energy of the scattered photon ($h\omega_S$). Two possibilities arise for the inelastic light scattering: a quantum of energy $h(\omega_i - \omega_S)$ is added to (**Stokes process**) or subtracted from (**anti-Stokes process**) the scattering medium.

The Raman effect is a consequence of the spatial and time-dependent fluctuation in the electronic contributions to the electric susceptibility [22]. The coupling of incident and scattered light to the medium can be understood as the modulation of the electric susceptibility by excitations, such as phonons, magnons or impurity vibrations [23]. First-order events dominate the Raman scattering process, where only a single quantum of excitation participates. Nevertheless, higher-order scattering processes involving two or more such excitations are as well observable. The Raman scattering cross section is much smaller than the elastic one and only 1 Raman photon per 10^7 incident photons is emitted [24]. Thus, in order to achieve the highest possible Raman intensity, laser light is needed as an excitation source. In the following, only the interaction between photons and lattice vibrations will be considered.

2.1.1 Inelastic Light Scattering by Phonons in Solids

Inelastic light scattering processes fulfill energy and momentum conservation. Considering a perfect crystal, elementary excitations (here, lattice vibrations) in the medium can be labeled by the crystal momentum $h\mathbf{q}$, also called quasi momentum. In general there is no linear dependence between the phonon frequencies $?_f$ and their respective wave vectors $\mathbf{q}_f$. The relation $?(\mathbf{q})$ is known as dispersion relation. The magnitude of the propagation vector ($\mathbf{k}_i$) of the incident radiation is $|\mathbf{k}_i| = ?_i n(?_i)/c$ with $n(?_i)$ the refractive index. In analogy, for the scattered wave the magnitude of the propagation vector is expressed by $|\mathbf{k}_S| = ?_s n(?_s)/c$. Then the phonon frequency that results from the scattering process is given by $? = ?_i – ?_s$ and the scattering wave vector reads $\mathbf{k} = \mathbf{k}_i - \mathbf{k}_S$. Momentum conservation is fulfilled, when the scattering wave vector is equal to the wave vector of the excitation

$$\mathbf{k} = \mathbf{q} \ , \qquad \textbf{(Eq. 2.1 a)}$$

while energy conservation requires

$$? = ?_f \ . \qquad \textbf{(Eq. 2.1 b)}$$

Fig. 2.1 depicts the inelastic scattering process. In the case of backscattering configuration (T=180 °) the largest value for the scattering wave vector **k** is obtained. A typical value for $\mathbf{k}_{max}$ is approximately 10^5 cm^{-1} at typical excitation wavelengths in the range of 400 - 1000 nm (visible and near-infrared light). This means $\mathbf{k}_{max}$ is around two orders of magnitude smaller than the size of the Brillouin zone of typical crystals. Hence, only phonons at or near the center of the Brillouin zone (G-point) take part in inelastic light scattering processes. If more excitations participate in the scattering process **(Eq. 2.1 a)** and **(Eq. 2.1 b)** transform into $\mathbf{k} = \sum_j \mathbf{q}_j$ and $\omega = \sum_j \omega_{fj}$ where j is the order of the process.

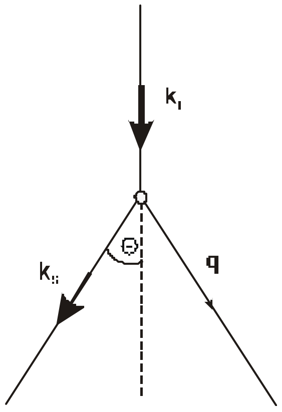

Fig. 2.1: Schematic diagram of the inelastic light scattering process, where $\mathbf{k}_i$ denotes the wave vector of the incident light, $\mathbf{k}_S$ the wave vector of the scattered light and q the wave vector of the excited phonons.

Within the **harmonic approximation model** phonons can be described as an ensemble of oscillators. The crystal potential is assumed to be a central potential and only terms quadratic in the Hamiltonian of the crystal are allowed as contributions to the total energy. These terms describe the displacements of the nuclei. Such a treatment can only be applied by introducing the **Born-Oppenheimer** or **adiabatic approximation**. Within this approach the electronic motion is separated from the ionic motion and the energies of the electrons can be expressed as functions of their corresponding ion positions. Thus, phonons can be described as displacements of the nuclei in periodic crystals and are solely expressed by planar waves, defined by the positions of the lattice atoms, and the force constants of the crystal. Then the dynamic equations of a crystal transform into an eigenvalue problem and the lattice vibrations are solutions of

$$(\mathrm{F} -\omega_f^2\mathbf{M})\ \mathbf{e}(f) = 0\ . \qquad \textbf{(Eq. 2.2)}$$

F is the so-called force constants matrix, the second derivative of the crystal potential, with the elements $\Phi_{ij}(?\kappa,?'\kappa') = \partial^2V(u)/(\partial u_i(?\kappa)\partial u_j(?'\kappa'))$. V(**u**) is the crystal potential, while **u** are the atomic displacements. $u_i(?\kappa)$ denotes the displacement in i-direction of the κ^{th} atom in the $?^{th}$ unit cell. For example, the force in j-direction on atom $(?\kappa)$ due to the displacement $u_i(?'\kappa')$ of the $(?'\kappa')$ atom in i-direction is given by $\Phi_{ij}(?\kappa,?'\kappa')u_i(?'\kappa')$. The matrix elements of **M** are defined by $M_{ij}(?\kappa,?'\kappa') = M(\kappa)d_{?\kappa i}d_{?'\kappa' j}$ with $M(\kappa)$ being the mass of the κ^{th} atom in the unit cell [25]. The presented expression has been chosen, as in the following (cf. **chapter 2.1.3**) the perturbation of the force constants and **M** will be discussed separately. **e**(f) in **(Eq. 2.2)** are the eigenvectors and fulfill the requirements of completeness and orthonormality. Since F shows translational symmetry, the Bloch theorem can be applied and these eigenvectors are represented by planar waves. Now, any collective atomic displacement reads as a linear combination of the eigenvectors with the normal coordinates Q_f: $\mathbf{u}(\mathbf{r},t) = \sum_f \mathbf{e}(f)Q_f$.

The incident radiation leads to the presence of an electric field **E**(**r**,t) in the medium, which will be considered to be monochromatic with the frequency ω_i and the wave vector $\mathbf{k}_i$. This incident electric field induces a polarization **P**(**r**,t) in the medium. Assuming a linear response, the polarization can be written as

$$\mathbf{P}(\mathbf{r},t) = \tfrac{1}{2} \sum_j \varepsilon_0(\chi_{ij}\exp[-i(\mathbf{k}_i\mathbf{r}-\omega_i t)]+\chi_{ij}^*\exp[+i(\mathbf{k}_i\mathbf{r}+\omega_i t)])\mathbf{E}_j(\mathbf{r},t)\ . \qquad \textbf{(Eq. 2.3)}$$

e_0 is the dielectric constant of the medium and χ_{ij} is the electric susceptibility characterizing the macroscopic medium. In other terms the polarization is represented by a modulation of the electric susceptibility of the medium induced by elementary excitations of the frequency ω_f. The modulation is determined by the atomic displacements as typically the frequencies of electronic transitions are much higher than the vibrational frequencies of the lattice. Considering this and assuming only small displacements from equilibrium, χ_{ij} can be expanded as a Taylor series in **u**. Here, only first-order terms will be considered

$$\chi_{ij}(\mathbf{u}) = \chi_{ij}(0) + \Sigma_f\, \chi_{ij,f}\mathbf{u}_f(\mathbf{r},t) \qquad \text{with} \qquad \chi_{ij,f} = \partial\chi_{ij}(\mathbf{u})'. \qquad \textbf{(Eq. 2.4)}$$

$\chi_{ij}(0)$ denotes the electric susceptibility of the medium with no fluctuations and $\chi_{ij,f}$ represents the oscillating susceptibility induced by the normalized lattice wave $\mathbf{u}_f$. Substituting **(Eq. 2.4.)** into **(Eq. 2.3)** results in an expression for the polarization of the medium in the presence of atomic vibrations

$$\begin{aligned}
&\mathbf{P}(\mathbf{r},t,Q_f) = \mathbf{P}_0(\mathbf{r},t) + \mathbf{P}_{ind}(\mathbf{r},t,Q_f)\,, \qquad \text{with}\\
&\mathbf{P}_0(\mathbf{r},t) = \tfrac{1}{2}\,\varepsilon_0\, \Sigma_j\, (\chi_{ij}(0)\exp[-i(\mathbf{k}_i\mathbf{r}-\omega_i t)] + \chi_{ij}(0)^*\exp[+i(\mathbf{k}_i\mathbf{r}+\omega_i t)])\mathbf{E}_j(\mathbf{r},t)\\
&\mathbf{P}_{ind}(\mathbf{r},t,Q_f) = \tfrac{1}{2}\,\varepsilon_0\, (\ \Sigma_{j,f}\, (\chi_{ij,f}\, Q_f \exp[-i[(\mathbf{q}_f-\mathbf{k}_i)\mathbf{r}-(\omega_i-\omega_f)t]] + \text{c.c.})\mathbf{E}_j(\mathbf{r},t)\ +\\
&\qquad\qquad \Sigma_{j,f}\, (\chi_{ij,f}\, Q_f \exp[-i[(\mathbf{q}_f+\mathbf{k}_i)\mathbf{r}-(\omega_i+\omega_f)t]] + \text{c.c.})\mathbf{E}_j(\mathbf{r},t)\ )\,,
\end{aligned} \qquad \textbf{(Eq. 2.5)}$$

where c.c. denotes the complex conjugate.

It follows from **(Eq. 2.5)** that $\mathbf{P}_0(\mathbf{r},t)$ describes a time-dependent polarization in phase with the incident radiation. This gives rise to elastic light scattering (Rayleigh). $\mathbf{P}_{ind}(\mathbf{r},t,Q_f)$ in **(Eq. 2.5)** denotes a polarization wave induced by a phonon. This describes the Raman effect (inelastic case) and is due to the non vanishing change of the polarizability and due to the induced electric dipole moment, respectively. $\mathbf{P}_{ind}(\mathbf{r},t,Q_f)$ consists of two contributions which are referred to as a Stokes shifted wave with the wave vector $\mathbf{k}_{Stokes} = \mathbf{q}_f - \mathbf{k}_i$ and the frequency $\omega_{Stokes} = \omega_i - \omega_f$ and an anti-Stokes shifted wave with the wave vector $\mathbf{k}_{AStokes} = \mathbf{q}_f + \mathbf{k}_i$ and the frequency $\omega_{AStokes} = \omega_i + \omega_f$.

The macroscopic theory of the Raman effect can be employed to reveal the scattering cross section. The scattering cross section is defined by the power radiated into a solid angle dΩ and divided by the incident intensity

$$\frac{ds}{d\Omega} = \frac{w_i^4 V^2}{(4pe_0)^2 c^4} \left| \sum_{ij} e_{si} c_{ij,f} e_{ij} \right|^2 . \qquad \textbf{(Eq. 2.6)}$$

V is the effective scattering volume of the medium; $\mathbf{e}_i$ and $\mathbf{e}_S$ are the polarization unitary wave vectors of the incident and scattered light. The contradiction of $\chi_{ij,f}$ with $\mathbf{e}_i$ and $\mathbf{e}_S$, respectively determines the existence of “selection rules”, which are given by the symmetry of the crystal. Measuring the dependence of the scattering cross section on the incident and scattered polarization, the symmetry of the corresponding Raman active phonon can be deduced. The symmetry of both, the medium and the vibrations leads to requirements on $\chi_{ij,f}$. This means that the scattered radiation vanishes for certain choices of the polarization vectors and scattering geometries. These requirements are the so-called **Raman selection rules**.

The description of the lattice dynamics and the inelastic scattering process was restricted to the harmonic approximation model. Despite the fair agreement of this model with the experiment, there exist some important limitations. For example, phenomena, which are due to anharmonic effects, require a modification of the model. As with the *in-situ* Raman technique the temperature dependence of the phonon modes can be investigated (cf. **chapter 5**), these phenomena will be shortly discussed in **chapter 2.1.3**.

2.1.2 Symmetry Considerations

In the previous section it has been explained that the Raman scattering cross section is dependent on the polarization vectors of the incident and scattered light. This dependence has its origin in the symmetry properties of the modulated susceptibility $\chi_{ij,f}$ and gives rise to the Raman selection rules. For Raman spectroscopy group theory offers a mathematical tool to classify the vibrations of the crystal under the respective symmetry operations and it allows the deduction of the Raman selection rules, i.e. the experimental configurations for which Raman modes are allowed or forbidden. The task of group theory is to find the group of translational and other symmetry operations leaving $\chi_{ij,f}$ invariant. At first, the group theoretical notations will be introduced.

2.1.2.1 Basics of Group Theory

The most important symmetry of a crystal is its invariance under specific translations. In addition to such translational symmetry most crystals possess both, rotational and reflection symmetries. Hence, group theory allows the systematization of those symmetry operations. A group **G** is defined as a set of elements {*a,b,c, ...*} for which an operation O(a,b) = *ab* between any two elements *a* and *b* of the group is defined. This operation must satisfy the following requirements:

- *Closure*: the result of the operation *ab* on any two elements *a* and *b* in **G** must belong to **G**,
- *Associativity*: for all elements *a, b* and *c* in **G** *(ab)c = a(bc)*,
- *Identity*: **G** must contain an element *e* such that *ae* = *a* for all elements *a* in **G**,
- *Inverse element*: for every element *a* in **G** there exist a corresponding element a^{-1} such that $aa^{-1} = e$, a^{-1} is known as the inverse of *a*.

In the case of *commutativity* of any elements *a, b* the group is **abelian**.

To simplify the description of the occurring non-translational symmetry operations, these are divided into five main groups and labeled by the **Schönflies notation**. These symmetries are rotation (C_n), where n denotes the n-fold of the rotation, reflection about a plane (*s*), inversion (*i*), rotoinversion (S_n) and the identity operation (*E*). The symmetry operations are completely specified by defining the corresponding axis of rotation or plane of reflection. **Point groups G_P**, as already indicated by the name, consist of symmetry operations in which at least one point remains fixed and unchanged in space. Therefore point groups contain only non-translational symmetry operations. In contrast, groups which contain both, translational and non-translational symmetry operations are known as **space groups G**. If point groups are compatible with a lattice with translational symmetry, these groups are called **crystallographic point groups**. In total there exist 32 distinct crystallographic point groups in 3-dimensional space [26].

The effect of a symmetry operation on a coordinate system can be represented by a transformation matrix. The set of such transformation matrices corresponding to a group of symmetry operations is also a group and is said to form a **representation** of the group. Such a representation can be generated by choosing some function f(x,y,z) and generating a set of functions $\{f_i\}$ by applying the symmetry operations O_i of the group to f(x,y,z) so that $f_i = O[f_i]$. As a group has to satisfy closure, $O[f_i]$ can be expressed by a linear combination of the functions f_i. The resulting coefficients form a square matrix, which will be referred to as the transformation matrix and the set of these matrices forms a representation of the group. However, the choice of functions $\{f_i\}$, known as **basis functions**, is not unique.

Obviously, there will be some transformation matrices being equal or zero. A representation of such transformation matrices is said to be **reducible**. These matrices can now be reduced by similarity transformations. If the matrices of a representation cannot be reduced anymore, the representation is said to be **irreducible**. However, the choice of irreducible representations of a group is not unique, but the set of traces of these equivalent irreducible representations is unique since unitary transformations preserve the traces. These traces are said to be **characters**.

In order to determine the characters of an irreducible representation the concept of **classes** is useful. A set of elements *T* in a group is said to form a class if for any element *a* in this group: *aT* = *Ta*. Thus, in a given representation all elements in a class have the same character. In addition, the number of inequivalent irreducible representations of **G** is equal to the number of classes. This means that if the elements of a group can be divided into j classes the characters of its j irreducible representations can be tabulated to form a table with j columns and j rows. Such a table is known as a **character table**.

2.1.2.2 Group Theoretical Aspects in Raman Spectroscopy

The following should serve as an outline for the identification of the Raman modes by the use of group theory. The analysis of the symmetry properties of $\chi_{ij,f}$ by group theory can be reduced to the problem that the scattering cross section in its scalar form should be invariant under any symmetry operation of the corresponding crystal. For this purpose it is useful to introduce the Raman tensor $R_{ij,f}$ which is defined by the contraction of Q_f with the first derivative of $\chi_{ij,f}$ with respect to Q_f. With **(Eq. 2.6)** the Raman scattering efficiency can be written as $dS/d\Omega \propto |\sum_{ij} R_{ij,f} e_i e_j Q_f|^2$. Thus, one has to find all linear combinations containing $e_i e_j Q_f$ which remain invariant under the symmetry operations of the corresponding crystal. The number of these linear combinations then represents the number of independent components of $R_{ij,f}$. Following the approach proposed by Callen [27] the form of the Raman tensor can be generated from the character tables of the corresponding point groups.

The so-called "nuclear site group analysis“ method [28] can be used to identify the number of Raman-allowed modes and their scattering tensors (symmetries) if the crystal structure is known: First, the space group of the corresponding crystal and the precise location of each atom in the unit cell has to be identified. Thereby, the Wyckoff notation [29] which designates the various possible atomic sites and the site symmetry can be used. In Ref. [30] a complete description of all space groups and allowed atomic sites can be found. Second, the irreducible representations of the zone-centered phonons that result from each of the non-equivalent, occupied sites in the unit cell have to be determined. In the last step the Raman tensors for the irreducible representations that are Raman allowed have to be identified and classified. Corresponding tables for the identification can be found in Ref. [31]. A common procedure for the classification of the normal modes is the following: Consider Γ_a to be an irreducible representation of the crystal space group, then **(Eq. 2.6)** can be written as

$$\Gamma_s = \Gamma_s \otimes \Gamma_a \otimes \Gamma_i \quad , \qquad \textbf{(Eq. 2.7)}$$

where Γ_s and Γ_i represent the symmetry of the polarization vectors. Due to the form of **(Eq. 2.7)**, Γ_s contains at least one totally symmetric irreducible representation. An important result of group theory is the so-called **matrix-element theorem**. For **(Eq. 2.7)** this theorem reads that Γ_a must be contained in the direct product $\Gamma_s \otimes \Gamma_i$. Hence, the Raman active modes belong to the irreducible representations which transform like Cartesian products with the form {x^2, y^2, z^2, $x\cdot y$, $x\cdot z$, $y\cdot z$}.

2.1.3 Anharmonic Effects

While the harmonic approach as described in **(Eq. 2.2)** is a good approximation for semiconductors, anharmonic contributions cannot be neglected considering some important effects such as temperature or stress dependence of the phonon frequencies, impurities or alloying. Perturbations of this kind will change the force constant and/or the matrix containing the masses of the atoms in the unit cell, so that **(Eq. 2.2)** turns into

$$[(F + \Delta F) - \omega_f^2(\mathbf{M} + \Delta\mathbf{M})]\, e(f) = 0 \quad . \qquad \textbf{(Eq. 2.8)}$$

The most obvious consequence due to the anharmonicity of the lattice is the following: Although the description of the phonons (Bloch waves) remains the same, the phonon lifetimes become finite. This means that in the harmonic approximation the shape of the phonon modes can be described by Dirac-Delta functions since there phonons are exact solutions of the Hamiltonian. However, a finite lifetime results in a non-vanishing line width of the measured Raman peaks.

The description of the influence of the anharmonicity requires higher-order terms of the potential function. However, these terms are very complex and many material constants are needed which makes the investigation complicated. So far the best results in calculating and predicting such effects have been achieved by ab initio calculations within density functional theory [32-34]. The description of these calculations is beyond the scope of this work, therefore a more phenomenological approach has been chosen.

2.1.3.1 Temperature Dependence

The influence of the anharmonicity is directly reflected by thermal expansion effects. In other words the amplitudes of the lattice vibrations increase and the influence of the anharmonic potential on the atoms is getting stronger. The increase of temperature is usually accompanied by an increase of the inter-atomic spacings. For a phenomenological description the approach proposed by Grüneisen has been chosen. This approach utilizes the relation between the thermal expansion and thermodynamic variables. Due to the anharmonicity of the inter-atomic potential the free energy F is dependent on the volume [35].

$$F = -k_B T \ln Z = \frac{V_0}{2k}\left(\frac{dV}{V_0}\right)^2 + \sum_{q,f}\left[k_B T \ln\left(1 - \exp(-\hbar w_{q,f} / k_B T)\right) + \frac{1}{2}\hbar w_{q,f}\right] \qquad \textbf{(Eq. 2.9)}$$

The first expression for the free energy is the general form of the equation of state for a harmonic oscillator expressed with the partition function Z. In the second expression of **(Eq. 2.9)** the sum combines the contributions of all existing oscillators with their respective zero point energies, while the first contribution describes the elastic energy caused by a small change in volume $\delta V = (V - V_0)$. $\kappa = -(V^{-1})(?V/?p)_T$ is known as the isothermal compressibility. Differentiating **(Eq. 2.9)** with respect to the volume results in an expression for the pressure p:

$$p = -\left(\frac{\partial F}{\partial V}\right)_T = -\frac{1}{k}\left(\frac{dV}{V}\right) - \hbar\sum_{q,f}\frac{\partial w_{q,f}}{\partial V}\left[\frac{1}{\exp(\hbar w_{q,f}/k_B T)-1}+\frac{1}{2}\right] .$$

(Eq. 2.10)

Because of only small changes in volume V_0 has been replaced by V. Considering anharmonicity, it follows from **(Eq. 2.10)**, that a change in volume involves a change in oscillator (phonon) frequencies. In the case of a harmonic potential, $(??_{q,f}/?V)$ would be equal to zero. Within the Grüneisen approach the relative change in the phonon frequency, $\delta(\Delta ?_{q,f})/?_{q,f}$, is assumed to be proportional to the relative change of the volume ($\delta(\Delta ?_{q,f})/?_{q,f} = -\gamma(\delta V/V)$), but independent from the frequency and mode of the respective phonon. Introducing the Grüneisen parameter ? in **(Eq. 2.10)**, the second contribution is an expression for the energy of all excited phonons, i.e. their inner energy including the energy at the zero point.
Therefore **(Eq. 2.10)** can be written as

$$pV = -\frac{dV}{k} + gU(T) \ ,$$

(Eq. 2.11)

and the thermal expansion coefficient α can be expressed by:

$$a = \frac{gkC_V}{3V} \ ,$$

(Eq. 2.12)

with $C_V = (?U/?T)_V = V/?(?p/?T)_V$ the specific heat capacity. The temperature dependence of α is only determined by the behavior of C_V, as κ can be assumed constant. With the expressions for κ, C_V and **(Eq. 2.11)**, the temperature dependence of the phonon frequency can be written as

$$\frac{\partial w}{\partial T} = \left(\frac{\partial w}{\partial V}\right)\left(\frac{\partial V}{\partial T}\right) = \left(\frac{\partial w}{\partial V}\right)\left(\frac{\partial V}{\partial p}\right)\left(\frac{\partial p}{\partial T}\right) = -3gaw \ .$$

(Eq. 2.13 a)

If ? has a positive value then it follows from **(Eq. 2.12)** that at constant wave vector a decrease of frequency with temperature will occur. Usually for high temperatures the expansion coefficient of solids is approximately constant. Therefore a shift of the Raman frequency proportional to the temperature is expected. For most of the semiconductors such a behavior has experimentally been observed. Vice versa this shifting of the Raman peak can be used to monitor the temperature of the specimen. However, the simplification that the thermal expansion coefficient a is approximately constant, is not valid for low temperatures. Thus, **(Eq. 2.13 a)** transforms into

$$\frac{\partial w}{\partial T} = w_0 \exp\left[-3g \int_0^T a(T')dT' \right] , \qquad \textbf{(Eq. 2.13 b)}$$

with ω_0 the phonon frequency at 0K and a as the integral over the respective temperature range.

To monitor the temperature via the temperature-dependent Raman shift, care has to be taken to verify that the Raman shift observed under local heating agrees with the shift determined for samples without any temperature gradients. For example films grown on a substrate often show a temperature dependent lattice mismatch which adds an additional stress contribution to the phonon frequencies. In those cases phonon decay processes cannot be neglected. Expanding the temperature-dependent peak shift as a Taylor series, higher-order terms have to be considered. Then the phonon population of the single decay channels determines the temperature dependence.

Besides the Raman shift, also the Raman intensity, and the Raman line width are dependent on the temperature. One advantage of temperature-dependent line width measurements is that here stress effects represent a second order perturbation, provided that there are no stress gradients leading to inhomogeneous broadening. A commonly used model to describe the temperature dependence of the line width has been developed by Klemens [36]. The model is based on the assumption that the only contributions to the line width arise from terms which represent the decay of the Raman phonon into two phonons of opposite **q** vector belonging to the same branch in the phonon dispersion curve. A more complete calculation is given by Cowley [37], where all possible phonon decay processes are taken into account and a realistic anharmonic potential is used. In **Fig. 2.2** the Feynman graphs of the lowest-order phonon decay processes are presented. Following Cowley's model Menéndez and Cardona formulated an expression for the full width at half maximum (FWHM: G) of the Raman peak corresponding to LO phonons in tetrahedral semiconductors [38]. In the simplest case of phonon decay into two phonons this can be expressed by

$$\Gamma(T) = \Gamma_{in} + \Gamma(0)[1 + n(w(\vec{q}, j_1)) + n(w(-\vec{q}, j_2))]. \qquad \textbf{(Eq. 2.14)}$$

The first contribution (G_{in}) is a temperature independent broadening of the line width that is due to defects or inhomogeneities. The second expression in **(Eq. 2.14)** describes the decay of optic phonons, where n is the thermal occupation number. At very high temperatures (>1000 K) **(Eq. 2.14)** no longer holds because then higher-order anharmonicity cannot be neglected anymore.

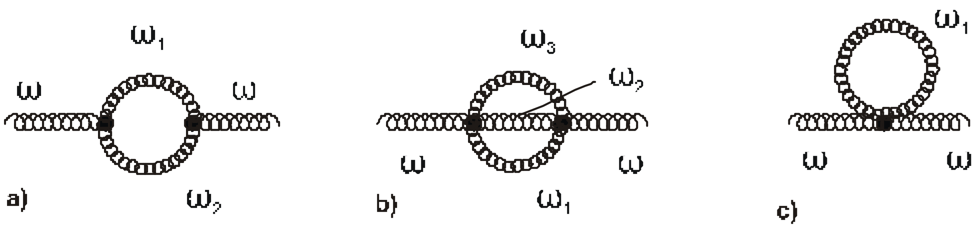

Fig. 2.2: Feynman diagrams of the lowest-orders in anharmonicity: decay of a phonon into **a)** two phonons and **b)** three phonons. Sketch **c)** depicts the fourth order anharmonic contribution to the real part of the self-energy.

2.1.3.2 Pressure Dependence

A similar procedure as for the case of thermal expansion can be applied to determine the pressure dependence of the phonon frequencies. Using the expressions for the Grüneisen parameter and the compressibility, the pressure dependence can be written as

$$\frac{\partial w}{\partial p} = \left(\frac{\partial w}{\partial V}\right)\left(\frac{\partial V}{\partial p}\right) = gkw = \frac{3aV}{C_V} w \quad . \qquad \textbf{(Eq. 2.15)}$$

In contrast to the temperature effect, here an increase of the phonon frequencies with increasing pressure takes place at constant wave vector and with ? having a positive value. This behavior has been observed for many semiconductors [39].

2.1.3.3 Stress Effects

The application of stress leads to a modification of the phonon structure due to the anharmonicity of the interatomic potential. The strain associated with the applied stress changes the equilibrium positions of the atoms in the crystal. Within the **quasi-harmonic approximation** the phonon frequencies corresponding to the deformed crystal potential can be calculated. Thereby the force constants are calculated at the new equilibrium positions. For small values of strain, it can be assumed that ΔF is linear in the strain. A Taylor expansion of ΔF in the force constants will give rise to higher-order terms of the interatomic potential. However, at this point only the linear case will be discussed. To determine ΔF Callen's method (cf. **chapter 2.1.2.2**) can be used [27] straight forward. Typical values of stress induce relative frequency shifts in the order of 0.1 % [28]. Therefore the stress effect can be considered as a small perturbation of the force constant matrix, cf. **(Eq. 2.8)**. In the presented case no perturbation of the mass matrix occurs ($\Delta\mathbf{M} = 0$) and the problem is to find the diagonalized form of the perturbed force constant matrix. Further calculations will be omitted and the reader is referred to the work of Anastassakis and Burstein [40] and to the work of Anastassakis and Cardona [41], respectively.

2.1.3.4 Effects due to Impurities

The presence of impurities can affect Raman spectra in different ways. First, the vibrational modes which are associated with motions of impurity atoms can produce new Raman peaks. The intensity ratios of the impurity and host Raman modes depend on the volume density of the impurity atoms. Thus, Raman spectroscopy can be used to estimate impurity concentrations.

Second, the Raman peaks of the host material can change. The impurity atoms can induce a shift or broadening of the Raman lines of the host material. In this case, it is necessary to distinguish atomic effects (change in mass and bond length) and electronic effects due to the presence of donors and acceptors (interaction of the carriers with the lattice). The atomic effects can be described with perturbation theory, but here both, perturbation in mass and strain must be considered when solving **(Eq. 2.8)**. The change in mass can be estimated to be uniformly distributed over all atoms in the crystal. Additionally, the different radii of the impurity and host atoms, which will give rise to a strain contribution, lead to a change in volume that is uniformly distributed over the crystal. With these approximations the shift of the phonon frequency is a function of the fractional impurity concentration. In the case of substitutional impurities (same valence state, but different mass) the sign of the mass difference determines the position of the local mode. If the impurity atom has a smaller mass than the host atom, frequency shifts of the host modes towards higher will result. Within the atomistic picture the heavier host atoms cannot follow the fast motion of the light impurity. When the impurity mass is larger than the host mass, the mode couples to the host continuum and a broadening of the Raman line is found [42].

For alloy semiconductors two different types of Raman spectra can be distinguished. The first type is characterized by vibrations of an “average” crystal – as the spatial distribution of the intermixing atomic species can be assumed to be nearly random. In the second type the occurring peaks can be related to vibrations of the respective pure materials – host and impurity material. The behavior of these two types is referred to as “one-mode” versus “two-mode” behavior. Nevertheless, changes between these two types as a function of composition can occur and have already been reported [43].

2.2 Energy-Dispersive X-Ray Diffraction

X-ray diffraction (XRD) represents an example of elastic light scattering in condensed matter. Within this process high energy-photons interact with the charge densities of the atoms in the crystal planes of the medium. In general the investigation of crystal structures is limited by the spatial resolution. It is well known from optics that diffraction can only be observed if the wavelength of the incident light is comparable to the characteristic dimensions of the medium. The minimal distance d_{min} which can be observed is proportional to the shortest wavelength of the incident white light. As distances between atoms in solids are usually in the range of a few tenths of nanometers, the energy has to be in the range of keV. Therefore X-ray diffraction allows the investigation the lattice d-spacings of the different crystalline phases and the distribution of the atoms in the unit cell. This method is used as a standard tool for phase identification. To facilitate the interpretation of XRD data table works are available [44].

2.2.1 Basics of Scattering Theory

The task of scattering theory is to find the relationship between the anisotropic scattering intensity and the scattering density ρ(**r**), i.e. the distribution of the scatterers. The knowledge of this relationship allows the identification of the structure of the sample. The observed scattered wave is a superposition of the contributions of all involved atoms. If the Bragg law is fulfilled, then a phase difference will occur between the incident and the scattered wave during the scattering process. As the value of the phase difference can be traced to the different positions of the scatterers, this value contains information on the structure. For the elastic scattering process $|\mathbf{k}_S| = |\mathbf{k}_I|$ holds. Thus, the phase difference is given by $(\mathbf{k}_S-\mathbf{k}_I)\mathbf{r}$ and the amplitude of scattering A can be written as the integral over the sample volume V:

$$\mathrm{A}(\vec{k}) = \int_V \rho(\vec{r})\exp(-i\vec{k}\vec{r})\,dV\,, \qquad \textbf{(Eq. 2.16)}$$

where the scattering wave vector is denoted by $\mathbf{k} = \mathbf{k}_s - \mathbf{k}_i$. Obviously, **(Eq. 2.16)** is a Fourier-transformation of the scattering density ρ(**r**):

$$\rho(\vec{r}) = \frac{1}{(2\pi)^3}\int \mathrm{A}(\vec{k})\exp(i\vec{k}\vec{r})\,d^3k \qquad \textbf{(Eq. 2.17)}$$

Taking the translational symmetry of the crystal structure into account when analyzing the scattering spectra, the periodic scattering density can be expanded in a Fourier series. Then, the 3-dimensional density ρ(**r**) is a sum of Fourier coefficients. That gives rise to vectors $\mathbf{G}_{hkl} = h\mathbf{b}_1+k\mathbf{b}_2+l\mathbf{b}_3$, where $\mathbf{b}_i$ are the vectors of a new coordinate system. As h, k and l are discrete values, $\mathbf{G}_{hkl}$ represent the points of the reciprocal lattice. The choice of the basis vectors of the new coordinate system has to fulfill the requirement of translational invariance of the original lattice. This periodicity of the scattering density can be expressed by

$$r(\vec{r}) = r(\vec{r} + \vec{R}) \, , \qquad \textbf{(Eq. 2.18)}$$

with **R** = $n_1\mathbf{a}_1+n_2\mathbf{a}_2+n_3\mathbf{a}_3$ the lattice vector and $\mathbf{a}_i$ the basis vectors of the crystal. Therefore translation invariance is only fulfilled when $\mathbf{b}_j\cdot\mathbf{a}_i = 2\pi\delta_{ij}$, where δ_{ij} is the Kronecker symbol and b_i are the vectors of the so called dual basis. This results directly in the relation for the basis vectors of the reciprocal lattice:

$$\vec{b}_1 = \frac{2p}{V_C}(\vec{a}_2 \times \vec{a}_3) \qquad \vec{b}_2 = \frac{2p}{V_C}(\vec{a}_3 \times \vec{a}_1) \qquad \vec{b}_3 = \frac{2p}{V_C}(\vec{a}_1 \times \vec{a}_2) \, , \qquad \textbf{(Eq. 2.19)}$$

with V_C = $(\mathbf{a}_1 \text{ x } \mathbf{a}_2)\ \mathbf{a}_3$ being the volume of the elementary cell of the original lattice. For the description of lattice planes or directions in a crystal Miller indices are used. In this notation lattice planes are defined by (hkl) and the [hkl]-direction is the direction of the vector, such that [hkl] = $h\mathbf{a}_1+k\mathbf{a}_2+l\mathbf{a}_3$. The relation between the Miller indices and the reciprocal lattice is given by the following expression for the distance d between two neighbored, equivalent planes

$$d_{hkl} = \frac{2p}{\left|\vec{G}_{hkl}\right|} \quad . \qquad \textbf{(Eq. 2.20)}$$

From **(Eq. 2.20)** it follows that the reciprocal lattice vector represents the set of lattice planes (hkl). $\mathbf{G}_{hkl}$ is orthogonal to these planes and its contribution is determined by the reciprocal distance of the lattice planes. Like in the original lattice, it is possible to define a Wigner-Seitz cell (Brillouin zone) for the reciprocal lattice. Usually points of high symmetry in the Brillouin zone are termed via group theory, like G, L, X. The G-point for example denotes the origin of the cell.

With **(Eq. 2.20)** the common Bragg law can be written as

$$\vec{k} = \left|\vec{k}_s - \vec{k}_i\right| = 2k_i \sin\Theta = G_{hkl} = 2p / d_{hkl} \quad , \qquad \textbf{(Eq. 2.21)}$$

where T denotes the angle between the incident or diffracted wave and the lattice planes. Therefore **(Eq. 2.21)** determines the angles at which reflections occur in an experiment.

2.2.2 The Scattered Intensity

Usually the intensity of the scattered signal is proportional to the amplitude of scattering $A(\mathbf{k})$. This means that the observed scattered intensity can be expressed by

$$I(\vec{k}) \propto \left|A(\vec{k})\right|^2 = \left|\int_V r(\vec{r})\exp(-i\vec{k}\vec{r})dV\right|^2 . \qquad \textbf{(Eq. 2.22)}$$

Within the approach of the reciprocal lattice the intensity of the reflections is given by the Fourier coefficients ρ_{hkl} of the scattering density and provides therefore information about the crystal basis. In general a crystal basis consists of more than one atom and interference between contributions of different atom sites leads to variations in the intensities of the reflections. Thus, the specific scattering properties of the single atoms must be considered. The atomic contributions can be expressed by the atomic scattering factor f_α. The position of an atom is expressed by $\mathbf{r}_\alpha = u_\alpha\mathbf{a}_1+v_\alpha\mathbf{a}_2+w_\alpha\mathbf{a}_3$, where the components u_α, v_α and w_α are given by the structure of the basis. Applying the concept of atomic scattering factors to **(Eq. 2.22)**, the scattered intensity can be written as

$$I(\vec{k}) \propto \left|F_{hkl}\right|^2 \text{ with } \quad F_{hkl} = \sum_a f_a(\vec{G})\exp(-i\vec{G}\vec{r}_a). \qquad \textbf{(Eq. 2.23)}$$

F_{hkl} is called the structure factor. In conclusion, the “content” of the unit cell can be determined from the intensity of the XRD-reflections, while the shape and dimension can be deduced from the scattering wave vectors of the reflections.

The standard method to analyze the distances of the lattice planes of solids with XRD is the method of Bragg-Brentano. In this case, the incident angle T and the angle 2T between incident radiation and detector are varied synchronously. In this work the method of EDXRD is used. In contrast to Bragg-Brentano, here the angle T and therefore 2T remains constant, while the varied parameter is the energy, or the wavelength, of the incident light. For this continuous spectral radiation is needed which can be realized for example with synchrotron radiation. For monocrystalline materials Bragg’s law **(Eq. 2.21)** is only fulfilled for specific angles T because d, the distance between the lattice planes, produces a reflection within a fixed angle in space.

Chapter 3

Fundamental Structural Properties of $CuInS_2$ Thin Films and $CuInS_2$-based Devices

There exist a large group of ternary semiconductors with the molecular formula ABC_2. These ternaries can be divided into two major groups: chalcopyrites ($A^{I}B^{III}C^{VI}{}_2$) and pnictides ($A^{II}B^{IV}C^{VI}{}_2$). Compounds with a chalcogenide basis such as for example $CuInSe_2$ and $Cu(In,Ga)(S,Se)_2$ are known as technologically significant device materials. They are of high interest for example in photovoltaic applications (both single-crystal materials as well as polycrystalline thin films), light-emitting diodes, and various nonlinear optical devices. The isoelectronic analogues of chalcopyrites are II-VI binary compound semiconductors. The respective analogue compound can be derived by incorporating the cation that is situated in the periodic table between the two cation atoms. In the case of $CuInS_2$, this results in $Zn_{0.5}Cd_{0.5}S$. In total there exist 36 known ternary chalcopyrites which are a combination of A = Cu, Ag, B = Al, Ga, In, Ti and C = S, Se, Te. Due to the variety of involved elements, different masses and bond lengths result. In addition these semiconductors cover a broad range of optical band gaps - from 1 eV ($CuInTe_2$) up to 3.5 eV ($CuAlS_2$) - and carrier mobilities.

In this chapter the main structural and vibrational aspects of chalcopyrites are discussed with emphasis on $CuInS_2$. The crystal structure, the Brillouin zone and the dispersion relation are presented and a detailed explanation of the calculation and assignment of the Raman modes is given. In the second part of this chapter polytypes of the chalcopyrite structure are presented. These are detectable with Raman spectroscopy and play an important role during the growth of $CuInS_2$ films as will be shown later (**cf. chapter 5**). Additionally, a brief overview of the electric properties of $CuInS_2$-based heterojunction solar cells is given as well as some remarks to the current state-of-the-art of these photovoltaic devices.

3.1 Vibrational and Structural Properties of Chalcopyrites

The crystal structure of ternary chalcopyrites can be derived from the zincblende structure in accordance to the Grimm-Sommerfeld rule by introducing two different atoms in the cation sublattice. Each anion is coordinated by two A and two B cations, whereby the A and B cations are alternately ordered on the (201) planes of the metal sublattice. Each cation is tetrahedrally coordinated by four anions. The chalcopyrite structure belongs to the space group I-42d (D^{12}_{2d}) with two formula units ABC_2 (eight atoms) per primitive unit cell. The space group of the zincblende structure is T^2_d with two atoms per primitive unit cell. The corresponding unit cell is tetragonal for the chalcopyrite structure and cubic for the zincblende structure. **Fig. 3.1** illustrates the chalcopyrite unit cell and the zincblende unit cell. The latter is roughly doubled along the c-axis. The C-atoms are white in the figure, while the A- and B-atoms are light gray and dark gray, respectively.

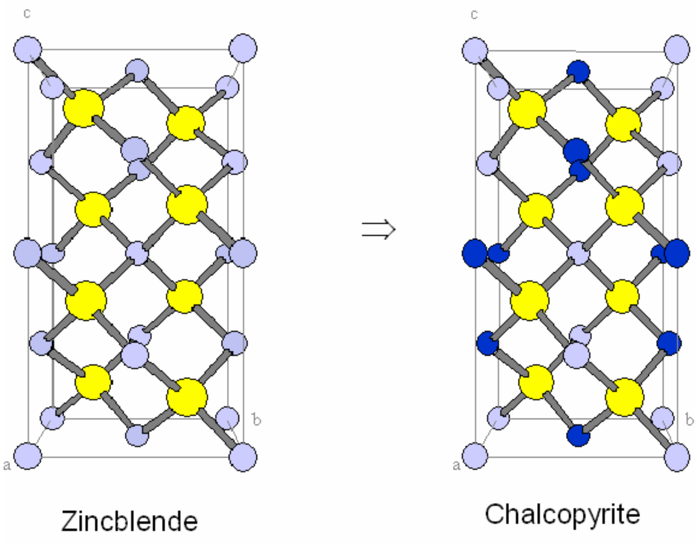

Zincblende
Chalcopyrite

Fig. 3.1: Zincblende (T^2_d, left side) and chalcopyrite (D^{12}_{2d}, right side) structure. The zincblende structure contains two atoms per unit cell and the chalcopyrite structure eight atoms per unit cell. C-atoms are white, A-atoms light gray and B-atoms dark gray.

Chalcopyrites consist of two different cation sublattices. The c-axis is roughly doubled compared to the zincblende structure. It is typical for the chalcopyrite structure that the chemical bond lengths R_{AC} and R_{BC} within the chalcopyrite structure might be different (R_{AC} ? R_{BC}). The bond lengths depend on the atomic radii and electronegativity of the cation species. In the case of R_{AC} ? R_{BC} the anions are displaced from their ideal sites and the chalcopyrite unit cell is distorted from the regular arrangement of an ideal tetragonal structure. The anion displacement can be expressed by the distortion parameter u ($u = \frac{1}{4} + (R_{AC}^2 - R_{BC}^2)/a^2$). The tetragonal compression ? of the unit cell is defined along the c axis (? = c/2a ? 1). Thus, the two nearest-neighbor bond distances are given by

$$R_{AC} = a\sqrt{u^2 + \frac{(1+h)^2}{16}} \quad \text{and} \quad R_{BC} = a\sqrt{(u-\frac{1}{2})^2 + \frac{(1+h)^2}{16}} \qquad \textbf{(Eq. 3.1)}$$

and the mismatch of the bond lengths a results in

$$a \equiv R_{BC}^2 - R_{AC}^2 = (u - \frac{1}{4})a^2 \ . \qquad \textbf{(Eq. 3.2)}$$

A zincblende-like undistorted anion sublattice has u = ¼ and a = 0. Hence, chalcopyrite structures compared to zincblende structures have additional structural (?, u) and chemical (A ? B) degrees of freedom [45]. In **Tab. 3.1** the values of a, c, ?, and u are listed for some Cu-chalcopyrite compounds [45,46]. It can be seen in the table that the tetragonal distortion parameter is close to 1, while the anion displacement shows a significant deviation from the ideal case – the largest deviation can be stated for $CuInS_2$.

Tab. 3.1: Values of the lattice constants a and c, the tetragonal distortion parameter ? = c/2a, and the anion displacement u = $¼+(R_{BC}^2-R_{AC}^2)/a^2$ (in units of a) for some $A^IB^{III}C^{VI}_2$ semiconductors [45,46].

Compound	a [Å]	c [Å]	?	u [a]
$CuInSe_2$	5.784	11.614	1.004	0.224
$CuGaSe_2$	5.614	11.032	0.9835	0.250
$CuGaS_2$	5.356	10.433	0.974	0.275
$CuInS_2$	5.523	11.118	1.0065	0.214

The band gaps of ternary I-III-VI_2-compounds are significantly smaller than those of their binary II-VI analogues. The reduced band gap ?E_g of chalcopyrites compared to their binary analogues is called band gap anomaly. Jaffe and Zunger [47] calculated the band gaps of chalcopyrites and found that the band gap anomaly is caused by a chemical ?E_g^{chem} and a structural ?E_g^S contribution:

$$\Delta E_g = \Delta E_g^{chem} + \Delta E_g^S \ . \qquad \textbf{(Eq. 3.3)}$$

The chemical contribution $?E_g^{chem}$ consists of two parts. One part describes the *d-p* hybridization $?E_g^{d}$ and the other part the cation electronegativity $?E_g^{CE}$. $?E_g^{d}$ considers the increase of the valence band maximum due to level repulsion between the cation (A^{I}) *d*-orbital and the anion (C^{VI}) *p*-orbital. This effect is significant for chalcopyrite-like compounds, while it is small for II-VI compounds. For the latter the cation *d*-orbitals are energetically lower than the anion *p*-orbitals. $?E_g^{CE}$ reflects the ability of the charge to separate on the two cation sublattices. The structural contribution $?E_g^{S}$ of the band gap anomaly is mainly caused by the anion displacement u. Only a small contribution comes from the tetragonal distortion ?.

The two basis atoms of the primitive unit cell of cubic zincblende compounds are located at X(0,0,0) and Y(¼,¼,¼) and these compounds exhibit 6 vibrational eigenmodes. Since chalcopyrite compounds contain two formula units per primitive unit cell, i.e. 8 atoms, 24 vibrational eigenmodes are expected at the G point of the Brillouin zone: 21 optical modes and 3 acoustic modes.

The precise location of each of the eight basis atoms of the chalcopyrite unit cell can be derived from **Fig. 3.1** (right side):

A_I: (0,0,0) A_{II}: (0,½,¼)
B_I: (0,0,-½) B_{II}: (0,½,-¼)
C_I: (-¼,u,-?) C_{II}: (-¼,u,-?) C_{III}: (u,-¼,?) C_{IV}: (u,¼,?) . **(Eq. 3.4)**

The number of atoms per unit cell is four times larger for the tetragonal unit cell of the chalcopyrite compound than for the zincblende unit cell. Thus, a reduced (folded) Brillouin zone (BZ) appears for the chalcopyrite structure in comparison to the zincblende structure. This means that the chalcopyrite BZ is four times smaller in **k**-space than the zincblende BZ. The Brillouin zones are shown in **Fig. 3.2** [48]. The eigenstates of chalcopyrite compounds can be classified into two groups: first-order-like and folded-like. For first-order-like eigenstates all the states have a direct counterpart at the same **k** value in the zincblende compounds. In the case of folded-like eigenstates, the X(0, 0, 2p/a), W(2p/a, 0, p/a) and W(0, 2p/a, p/a) points of the zincblende BZ are folded to the zone-center (G point) of the Brillouin zone of the chalcopyrite structure. Thus, the 24 chalcopyrite eigenmodes are classified into three groups: six modes of G[G], six modes of G[X] and twelve modes of G[W].

There are different ways to classify the large number of optical phonons in chalcopyrites. In a first approximation the chalcopyrite eigenmodes can be obtained

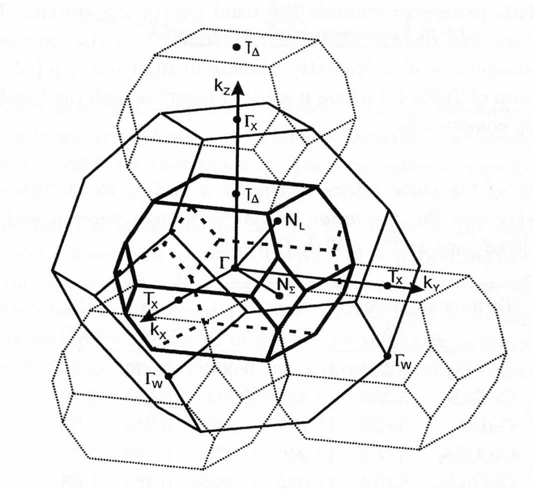

Fig. 3.2.: Chalcopyrite and zincblende Brillouin zone from Ref. [48]. The large polyhedra show the zincblende reciprocal-space regions that fold into the chalcopyrite Brillouin zone (small polyhedra).

starting from the Brillouin zone of the zincblende structure. Second, group theoretical considerations on the group symmetry of the optical phonons (cf. **chapter 2.1.2.2**) allow a classification of these modes. On the other hand, a variety of phenomenological models have been suggested to calculate the phonon dispersion relations of semiconducting materials, such as the force constant model [21], the shell model [49] and different bond models [50].

In the following the group theory, as introduced in **chapter 2.1.2**, will be used to determine the different Raman modes and their corresponding symmetries for the chalcopyrite structure. For that the *nuclear site group analysis* procedure as proposed by Callen (cf. **chapter 2.1.2.2**) will be used. For the sake of simplicity the case of an ideal chalcopyrite structure with $u = \frac{1}{4}$ shall be considered. In total eight symmetry operations can be defined for the chalcopyrite space group:

- *identity* operation: E
- *rotoinversion* operation and its inverse element: $2S_4$
- *rotation* operation about a screw axis along the z axis of the crystal, and two rotation operations about screw axes along the x+y and the x-y axis of the crystal including a non-translational vector: C_2 and $2C'_2$
- two *reflection* operations about glide planes normal to the crystallographic directions x+y and x-y including a non-translational vector: $2s_d$

In order to find the characters of the reducible representation of the normal modes of the chalcopyrite structure, the symmetry operations must be applied upon each atom of the crystal basis. This results in a set of transformation matrices for the chalcopyrite structure. The traces of these transformation matrices, which are associated with the symmetry operations, will give rise to the characters of the representation. Remarkably, only atoms, which remain unchanged after applying a given symmetry operation, contribute to the traces. The reducible representation of the crystal G_T is composed by the coordinates of each atom remaining unchanged, while a change in sign of a coordinate will be counted as –1. In **Tab. 3.2** the characters of the single transformations of chalcopyrites for the reducible representation G_T of the crystal as well as those of the basis atoms (G_A, G_B, G_C), are given.

Tab. 3.2: Characters of the reducible representation for the chalcopyrite structure (G_T) and the corresponding basis atoms (G_A, G_B, and G_C)

	E	$2S_4$	C_2	$2C'_2$	$2s_d$
G_T	24	-4	-4	-2	0
G_A	2	2	2	0	0
G_B	2	2	2	0	0
G_C	4	0	0	4	0

With the aid of the character table of the corresponding point group the irreducible representation can be determined and the symmetry of the zone-center phonons (**q** = 0) can be deduced. The point group for chalcopyrite–like compounds is D_{2d} and the corresponding character table is given in **Tab. 3.3**. Here, the irreducible representations for the point group D_{2d} are listed together with their corresponding Cartesian symmetry coordinates. Additionally, the activities (Raman- (R) and infrared- (IR) active) of the irreducible representations are given. Five different types of irreducible representations are known, namely A_1, A_2, B_1, B_2 and E. Only the E representation of these is double degenerated. Triple degenerated representations do not exist for this point group because of the inequivalence of the x-y and z directions.

Tab. 3.3: Character table for the point group D_{2d}, together with the symmetries and activities

D_{2d} (chalcopyrite)	E	$2S_4$	C_2	$2C'_2$	$2s_d$	Symmetry	Activity
$G_1(A_1)$	1	1	1	1	1	x^2+y^2, z^2	R
$G_2(A_2)$	1	1	1	-1	-1		Inactive
$G_3(B_1)$	1	-1	1	1	-1	x^2-y^2	R
$G_4(B_2)$	1	-1	1	-1	1	xy; z	R; IR
$G_5(E)$	2	0	-2	0	0	xz, yz; x, y	R; IR

Thus, expressing the representations in **Tab. 3.2** with the aid of **Tab. 3.3**, the irreducible representation of the zone-centered phonons of the crystal and the irreducible representations of the basis atoms are

$$G_T = 1A_1 \oplus 2A_2 \oplus 3B_1 \oplus 4B_2 \oplus 7E$$
$$G_A = 1A_1 \oplus 1A_2$$
$$G_B = 1A_1 \oplus 1A_2$$
$$G_C = 1A_1 \oplus 1B_1 / 1E\ . \qquad \textbf{(Eq. 3.5)}$$

G_T contains all 24 modes at the zone-center, acoustic as well as optical modes. As the acoustic modes are only described by translational vectors, it follows from **Tab. 3.3**:

$$G_{ac} = 1B_2 \oplus 1E$$
$$G_{opt} = G_T - G_{ac} = 1A_1 \oplus 2A_2 \oplus 3B_1 \oplus 3B_2 \oplus 6E \quad . \qquad \textbf{(Eq. 3.6)}$$

All optical modes in **(Eq. 3.6)** are Raman active and partially infrared-active except the two A_2-modes, these are inactive (cf. **Tab. 3.3**). The corresponding Raman tensors for the irreducible representation of the chalcopyrite structure [51] have the form

$$A_1 = \begin{pmatrix} a & 0 & 0 \\ 0 & a & 0 \\ 0 & 0 & b \end{pmatrix} \qquad B_1 = \begin{pmatrix} d & 0 & 0 \\ 0 & -d & 0 \\ 0 & 0 & 0 \end{pmatrix} \qquad B_2 = \begin{pmatrix} 0 & e & 0 \\ e & 0 & 0 \\ 0 & 0 & 0 \end{pmatrix}$$
$$E_x = \begin{pmatrix} 0 & 0 & f \\ 0 & 0 & 0 \\ g & 0 & 0 \end{pmatrix} \qquad E_y = \begin{pmatrix} 0 & 0 & 0 \\ 0 & 0 & f \\ 0 & g & 0 \end{pmatrix} \quad . \qquad \textbf{(Eq. 3.7)}$$

A mode transforming like B_2 or E is associated with a finite dipole moment and shows a change in polarizability. Therefore these modes are infrared as well as Raman-active. Due to the polar character of their vibrations, these two modes exhibit LO-TO splitting. This means, using **(Eq. 3.6)** the total number of Raman-active modes is 22.

It is left now to assign the identified modes to specific vibrations of the anion and cation sublattices. On the one hand a first hint for this assignment will be given when exchanging the participating anion (C^{VI}) or cations (A^I, B^{II}), e.g. the anion S by Se [52]. On the other hand the symmetry coordinates of each vibration can be derived from the relevant normal modes of the zincblende structure, which have been calculated by several authors [53], folded into the zone-center and combined in such a way that the coordinates of the symmetry are given as required in **Tab. 3.3** [54]. In the presented case the calculation of the symmetry coordinates of each mode is based on the atomic displacement vectors of the single atoms combined with the symmetry properties of the mode. The entire set of symmetry coordinates for chalcopyrite-like structures is shown in **Tab. 3.4**. The subscripts of E_x and E_y refer to the E-mode coordinates with x and y dipole moments. It should be noted that the displacements of any two atoms of the same species are symmetry related, while this is not valid for atoms of different species.

Tab. 3.4: Calculated Cartesian symmetry coordinates of the 21 optical phonon modes in $A^IB^{III}C^{VI}_2$-chalcopyrites, the atomic positions are given by **(Eq. 3.4)**.

Mode	**A^I**	**B^{III}**	**C^{VI}**
A_1	0	0	$y_1-y_2-x_3+x_4$
A_2^1	0	0	$x_1-x_2+y_3-y_4$
A_2^2	0	0	$z_1+z_2-z_3-z_4$
B_1^1	z_1-z_2	$-z_1+z_2$	$y_1-y_2+x_3-x_4$
B_1^2	z_1-z_2	z_1-z_2	0
B_1^3	z_1-z_2	$-z_1+z_2$	$-y_1+y_2-x_3+x_4$
B_2^1	z_1+z_2	z_1+z_2	$-z_1-z_2-z_3-z_4$
B_2^2	z_1+z_2	$-z_1-z_2$	$-x_1+x_2+y_3-y_4$
B_2^3	z_1+z_2	$-z_1-z_2$	$x_1-x_2-y_3+y_4$
E_x^1	x_1+x_2	x_1+x_2	$-x_1-x_2-x_3-x_4$
E_x^2	$x_1-y_1+x_2+y_2$	$-x_1+y_1-x_2-y_2$	$-z_1+z_2$
E_x^3	y_1-y_2	y_1-y_2	$x_1+x_2-x_3-x_4$
E_x^4	$x_1+y_1+x_2-y_2$	$-x_1-y_1-x_2+y_2$	0
E_x^5	$x_1-y_1+x_2+y_2$	$-x_1+y_1-x_2-y_2$	z_1-z_2
E_x^6	y_1-y_2	y_1-y_2	$-x_1-x_2+x_3+x_4$
E_y^1	y_1+y_2	y_1+y_2	$-y_1-y_2-y_3-y_4$
E_y^2	$x_1+y_1-x_2+y_2$	$-x_1-y_1+x_2-y_2$	z_3-z_4
E_y^3	$-x_1+x_2$	$-x_1+x_2$	$-y_1-y_2+y_3+y_4$
E_y^4	$-x_1+y_1+x_2+y_2$	$x_1-y_1-x_2-y_2$	0
E_y^5	$x_1+y_1-x_2+y_2$	$-x_1-y_1+x_2-y_2$	$-z_3+z_4$
E_y^6	$-x_1+x_2$	$-x_1+x_2$	$y_1+y_2-y_3-y_4$

It can be seen in **Tab. 3.4** that the A_1-mode exhibits pure anion movement. The coordinate $y_1-y_2-x_3+x_4$ for the C^{VI}-atoms - as defined in **(Eq. 3.4)** - indicates that the C_I-atom moves in y-direction, the C_{II}-atom in -y-direction, the C_{III}-atom in -x-direction, and the C_{IV}-atom in x-direction. Although the two A_2-modes are inactive, they are included in **Tab.3.4**. They are also characterized by pure anion movement. The B_1^2 as well as the $E_{x,y}^4$-modes are, in contrast, due to pure cation movement. For the B_1^2-mode the two cations species vibrate in phase while for the $E_{x,y}^4$-modes in anti-phase. All other modes involve a combined movement of both, cations and anions. As an example the atomic movements of the A_1-and B_2^1-modes are presented in **Fig. 3.3**. The sulfur atoms are white, while the Cu-atoms are marked light gray and the In-atoms dark gray. The directions of the atomic movements are indicated by the arrows.

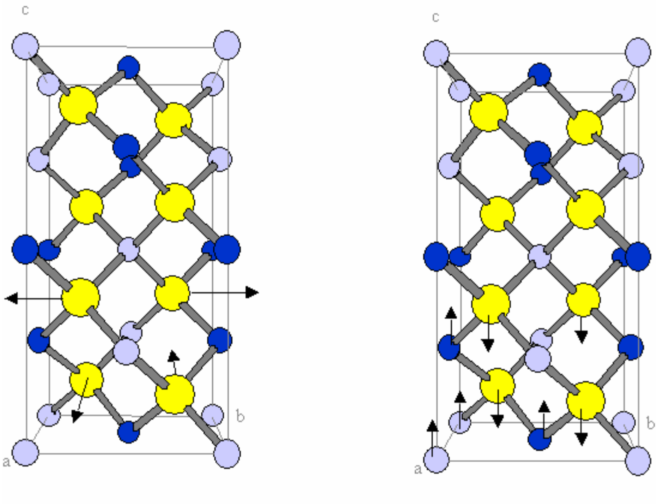

A_1-mode

B_2^1-mode

Fig. 3.3: Atomic movements of the A_1- and B_2^1-modes of $CuInS_2$. The arrows indicate the directions of the respective movements, while the colors reflect the different atoms; S: white, Cu: light gray, and In: dark gray.

For the calculation of the mode frequencies and the better understanding of the behavior of the vibrations it is helpful to consider the dynamical properties such as the phonon dispersion relation. Phonon dispersion relations are usually investigated by neutron scattering experiments. Unfortunately, for $CuInS_2$ no such experiments have been performed yet. However, different approaches have been developed to calculate the phonon dispersion relation of chalcopyrite-like compounds. For example the chalcopyrite structure can be described by a *tetra-atomic linear chain*[54]. In this highly simplified model the cations are connected only by nearest-neighbor forces to the anions. Thus, the chalcopyrite structure can be considered as a perturbation of the zincblende structure. In this case the mode frequencies depend only on the force constants (k_{AC}, k_{BC}) and on the masses of the participating atoms. Obviously, no long-range Coulomb interactions are included within this model.

In the *shell model* proposed by Cochran [55] such long-range Coulomb interaction can be included. The main idea of this model is the assignment of charges to shells (valence electrons) and the introduction of dipole moments caused by the displacement of the shell relative to the core (rigid ion). Thus, the interaction between induced dipoles simulates the long-range Coulomb interaction and the short-range interaction can be limited to nearest neighbors. Although the actual valence electron distribution differs from such spherical shells, good agreement has been found for non-covalent solids, see Refs. [37,55,56].

In order to find a model using parameters with a clear physical meaning the *valence force field method* has been developed. Within this approach the crystal structure is described by stretching bonds and changing angles between the bonds (bond bending). Long-range forces due to Coulomb interaction must be added. Within this model the displacements of the ions are directly related to the bond coordinates while the stretching and bending parameters are characteristics of the bonds; exemplary calculations can be found in Refs. [57-59]. The parameters can be obtained by calculating the elastic constants. Obviously, the valence force field model requires a large amount of parameters. Keating developed a model, where the bond stretching and bond bending parameters are reduced with an additional charge parameter for ionic crystals [60]. Keating's approach is widely used due to its simplicity. Neumann et al [61] proposed a further simplification of the Keating model for high energy modes. Within this approach only the bond-stretching parameters are taken into account as these are significantly larger than the bond-bending parameters. However, for low energy modes the bond-bending parameters cannot be neglected. In order to consider polar modes, which have a non-vanishing dipole momentum per unit cell, so-called localized effective charges must be introduced. These result in reduced bond stretching parameters. Using Neumann's model it is possible to calculate the mode frequencies. Reliable results for the mode frequencies at the zone-center of the Brillouin-zone have been obtained with this approach. Nevertheless the phonon dispersion relations could not be described conveniently.

Recently, *ab initio* calculations have been performed for $CuInS_2$ lattice dynamics by Lazewski and coworkers [62]. **Fig. 3.4** shows their results for the phonon dispersion relation of $CuInS_2$. Former *ab initio* calculation for the lattice dynamics of $CuInSe_2$

performed by these authors [63] gave good agreement with the data from neutron scattering experiments. In the *ab initio* calculations the long-range macroscopic field, which is accompanied by the displacements of the atoms, is introduced in the dynamical matrix by a nonanalytical contribution. This contribution considers the polar character of the infrared active vibrations and results in LO-TO splitting. In principle, the phonon branches in **Fig. 3.4** can be separated into two frequency regions. On the one hand the region below 4.5. THz which mainly represents Cu and In vibrations and on the other hand a high frequency region which reflects S vibrations. The phonon branches of the A_1-mode around the G-point are marked by arrows in **Fig. 3.4**. It is well visible that this branch exhibits a positive slope in G ? Z and G ? X direction. The implications of this behavior will be discussed later in **chapter 6.2.1**. In order to illustrate the LO-TO splitting at the G point also the B_2^2 mode has been marked in the figure (X ? G: 6.93 THz B_2^2(TO) and G ? Z:7.67 THz B_2^2(LO)).

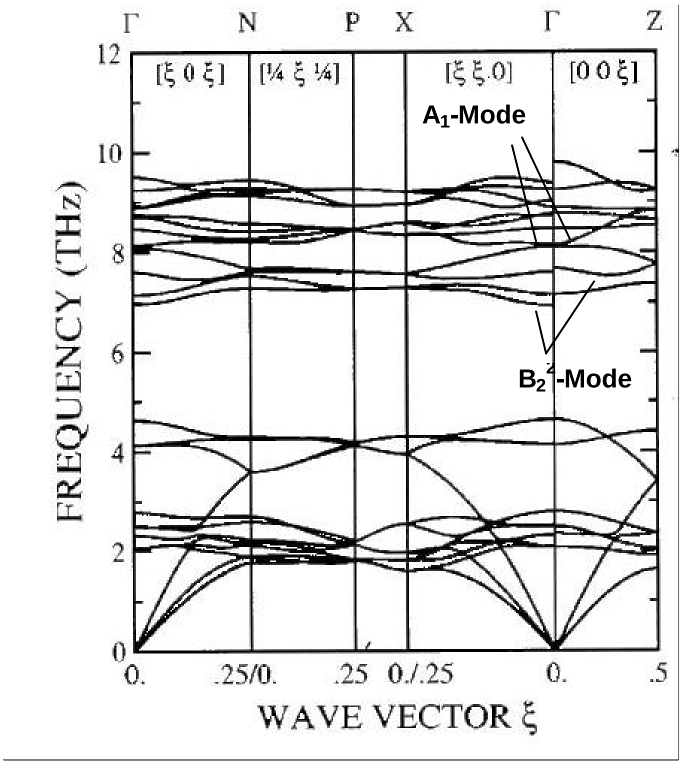

Fig. 3.4: Phonon dispersion relation of $CuInS_2$ as calculated by Lazewski and coworkers [62]. The A_1- and the B_2^2-mode are marked by arrows.

For $CuInS_2$ a large number of experimentally determined Raman frequencies has been reported. The values of the Raman modes and their assignment are partially differing. Ohrendorf and Haeuseler [65] systematized the literature data and found the experimentally determined Raman frequencies of Koschel and Bettini [64] the most reliable.

In this thesis all measurement were performed on polycrystalline $CuInS_2$ thin films. **Fig. 3.5** shows a typical $CuInS_2$ Raman spectrum of a polycrystalline film at room temperature as measured within this work. The low frequency range is not shown because no Raman peaks were detectable within this range. In general the Raman scattering efficiency of $CuInS_2$ is low, which might be due to its high absorption coefficient [65,66]. In the presented experiment only 9 out of 22 predicted modes could be clearly identified. This was expected as, for example, the B_1-modes are reported to appear very weak. Besides the high intense mode at around 290 cm^{-1}, which corresponds to the totally symmetric A_1-mode, six peaks at 237, 240, 259, 323, 338 and 345 cm^{-1} have been detected. These could be assigned to the B_2^2(TO), E^3(TO), B_2^2(LO)/E^3(LO), B_2^1(TO)/E^1(TO), E^1(LO) and B_2^1(LO) modes. The peaks at around 259 and 323 cm^{-1} are assigned to overlapping E- and B_2-modes. A characteristic signature for many chalcopyrite compounds – an exception is $CuInTe_2$ [68] – is the dominance of the totally symmetric A_1-mode in the Raman spectrum as can be seen in **Fig. 3.5** .

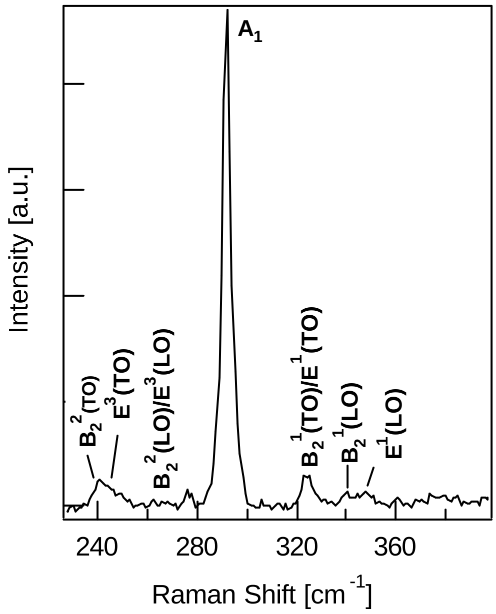

Fig. 3.5: Typical Raman spectrum of a polycrystalline $CuInS_2$ film as recorded within this thesis. All visible Raman peaks are assigned according to Koschel and Bettini [64].

The mode frequencies obtained by Koschel and Bettini (at 78 K) for $CuInS_2$ (single crystal) [64] together with the values of this work (polycrystals) are listed in **Tab. 3.5**. As already mentioned, the classification of the Raman active modes often takes place via symmetry considerations starting from the zincblende structure.

Therefore the symmetries of the chalcopyrite modes as well as the corresponding symmetries of the zincblende modes are added in the table. In order to test the experimental data of this work, the test criteria as formulated by Ohrendorf and Haeuseler [65] can be found in the last two rows.

Tab. 3.5: Experimentally determined Raman active frequencies in $CuInS_2$ of this thesis and by Koschel and Bettini [64]. Additionally, the CH- and ZB-symmetries together with the test criteria (in the last two rows) as formulated by Ohrendorf and Haeuseler [65] are listed.

CH symmetry	Mode	Koschel $?_0$ [cm^{-1}]	This work $?_0$ [cm^{-1}]	ZB symmetry
$G_{4L,T}$	B_2^1(L/T)	352/323	345/323	$G[G_{15}]$
$G_{5L,T}$	E^1(L/T)	339/321	338/323	$G[G_{15}]$
G_3	B_1^1	-	-	$G[W_2]$
$G_{5L,T}$	E^2(L/T)	314/295	-	$G[W_4]$
G_1	A_1	294	290	$G[W_1]$
$G_{4L,T}$	B_2^2(L/T)	266/234	259/237	$G[W_2]$
$G_{5L,T}$	E^3(L/T)	260/244	259/240	$G[X_5]$
G_3	B_1^2	-	-	$G[X_3]$
$G_{5L,T}$	E^4(L/T)	-/140	-	$G[W_3]$
$G_{5L,T}$	E^5(L/T)	-/88	-	$G[W_4]$
$G_{4L,T}$	B_2^3(L/T)	-/79	-	$G[W_2]$
G_3	B_1^3	-	-	$G[W_2]$
$G_{5L,T}$	E^6(L/T)	-/67	-	$G[X_5]$
	$E^1:B_2^1$	0.994	0.979	
	$E^3:B_2^2$	1.043	1.006	

Comparing the frequencies and the test criteria in **Tab. 3.5**, good agreement between the experimentally determined Raman modes of this thesis and of Koschel and coworkers has been achieved.

3.2 Polymorphism in Chalcopyrites

Depending on the stoichiometry, the growth of $CuInS_2$ from the elements proceeds via various chemical phases. The phase triangle or Gibbs diagram (**Appendix A.3**) for the Cu-In-S system proposed by Metzner and coworkers at room temperature [69,70] includes binary and ternary phases.

In chalcopyrites the distribution of non-isovalent A^{I}-B^{III} atoms exhibits a first-order phase transition between the high-temperature disordered zincblende superstructure and the ordered chalcopyrite structure. The transition temperature T_c is in the range of 800 to 1300 K for chalcopyrites [71]. In the disordered zincblende superstructure the cation atoms are randomly distributed, while the anions remain in an fcc sublattice. Due to the random distribution the originally tetragonal unit cell becomes cubic. The order-disorder transition only occurs below a critical anion displacement ($u_c < 0.265$) or above a critical tetragonal compression (?$_c$ > 1.95). Otherwise the highly destabilizing microscopic strain in the disordered phase can not be compensated and the phase would melt before the order-disorder transition can take place [47,72].
However, below T_c the Grimm-Sommerfeld rule can also be fulfilled by cation orderings which are different from the chalcopyrite structure (I-42d). Alternating A^{I} and B^{III} cations in (100) planes lead to the so-called “copper-gold” (CuAu) phase (P-4m2), while the “copper-platinum” (CuPt) phase arises from alternating A^{I} and B^{III} atoms in the [111] direction (R-3m). The names CuAu and CuPt refer to atomic orderings in metallic superstructures [73]. In the CuAu phase the tetrahedra which surrounds the C atom is still of the A_2B_2 type and therefore identical as for the chalcopyrite phase. However, in the CuPt-like structure the C atom is surrounded by an A_1B_3 or an A_3B_1 tetrahedra . The unit cells for the chalcopyrite (CH), the CuAu (CA) and the CuPt ordered structures are shown in **Fig. 3.6**.

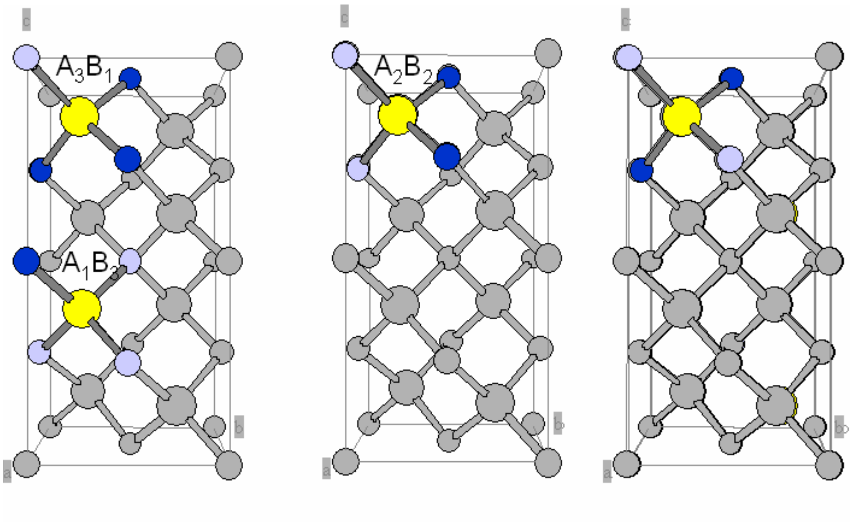

CuPt Chalcopyrite CuAu

Fig. 3.6: Unit cells of the CuPt-(left), CH-(middle), and CA-phases (right) of $CuInS_2$. The different colors indicate the different atoms of $CuInS_2$: C^{VI}-atoms: white, A^{I}: light gray, B^{III}: dark gray.

Wei et al. [10] listed all possible C-centered A_nB_{4-n} cation tetrahedra and their combinations. They calculated the corresponding formation energies E_f. The calculations show that the formation energy difference between CA and CH is 8 meV per 4 atoms, while for the CuPt-phase this value is 213 meV per 4 atoms [11,74].

Additionally, the CA- and CuPt-phases are accompanied by a reduction in the direct band gaps relative to the chalcopyrite phase [75]. **Tab. 3.6** gives the values of the relative formation energies of the 3 crystallographic $CuInS_2$ orderings and their relative band gaps.

Tab. 3.6: Calculated formation energies and band-gaps for CH-, CA- and CuPt-modification in relation to the values of CH-ordered $CuInS_2$.

Type	Relative Formation Energy [meV/atom]	Band Gap Reduction [eV]
CH	0	0
CuAu	+2	-0.03
CuPt	+65	-1.09

The formation energy difference of the CA- and the CH-phase $E_f(CA) - E_f(CH)$ is small. Thus, the growth of $CuInS_2$ below T_c might result in a metastable mixture of CH- and CA-phases. Su and coworkers [76,77] proposed the following simple expression to describe the actual structure of vapor-phase grown $A^IB^{III}C^{VI}_2$ films by means of correlation functions of the chalcopyrite structure f_{CH} and the CuAu-like structure f_{CuAu}

$$f = af_{CH} + bf_{CuAu} \quad , \qquad \textbf{(Eq. 3.8)}$$

with $a < 1$, $b < 1$ and $a + b = 1$. These parameters vary when the growth kinetics change.

Indeed, the coexistence of the CH- and CA-phases is well known for epitaxial as well as for polycrystalline films. For example, the CuAu structure has been identified to occur in single crystalline films due to specific substrate orientation [69]. For epitaxial III-V semiconductors those coexisting phases can be induced by surface effects [78,79], where dimerization leads to an energetical stabilization of the metastable crystalline phases.

The CuPt-phase has experimentally not been found in $CuInS_2$ specimen. Its absence can be explained by the formation energy as shown in **Tab. 3.6**. Furthermore, the

CuPt-phase deviates from the octet rule and therefore contains electronically noncompensated tetrahedra [76].

The relative band gap reduction for the CA-phase E_g(CA) - E_g(CH) is small. Therefore the difference between the optical properties of the CuAu structure and the CH structure will not be large. In contrast, the relative band gap reduction for the CuPt-phase is high, which would lead to a strong fingerprint on the optical properties compared to the chalcopyrite structure.

Raman spectra of polycrystalline $CuInS_2$ films exhibit sometimes an additional Raman mode at 306 cm^{-1} next to the $CuInS_2$ chalcopyrite A_1-mode at 290 cm^{-1} [80]. However, this additional Raman band could not be assigned to zone-centered phonons. At first it was assumed that this mode belongs to an In-rich defect spinel, as it often appears in In-rich films. Meanwhile this assignment is assumed to be incorrect, because further peaks related to this defect phase could no be observed [81]. In addition, it has been found that the mode at 306 cm^{-1} does not appear only in In-rich sample, but as well when the films are grown at too low temperatures [82]. Kondo et al. [83] performed polarization measurements and found this peak to be related to a localized, totally symmetric mode. Alvarez et al. [15] identified a second additional Raman band at 60 cm^{-1}, and found a direct correlation between these two modes. They assigned these two modes to zone-centered phonon modes of the CuAu modification of $CuInS_2$. Furthermore, combined Raman and XRD measurements, which have been performed by the same group, revealed a direct correlation between the Raman A_1-mode intensities of the CA- and CH-ordered structure and characteristic XRD intensities of these two phases. Based on these results it is obvious to assign the additional Raman mode at 306 cm^{-1} to the A_1-mode of the CA-phase. Besides, Riedle and Fritsch [84] identified this mode by calculations of the lattice dynamics of the CA-ordered structure. In **Tab. 3.7** the different modes of the CuAu structure are listed together with their Raman frequencies.

Within XRD studies the peaks related to the CuAu structure are usually of small intensity and sometimes even below the detection limit. In contrast, Raman spectroscopy is a powerful tool to detect this phase. Within this thesis the CA-related Raman band at around 305 cm^{-1} has been found for samples grown under different conditions. *In-situ* Raman experiments on the growth of $CuInS_2$ films will show the relationship between the presence of this mode and the growth conditions (cf. **chapter 5.3**).

Tab. 3.7: The 6 optical phonon modes in CA-ordered CuInS$_2$ and their Raman frequencies as calculated by Riedle and Fritsch [84].

Mode (CA-phase)	?$_0$ [cm^{-1}]
E^3	69
B_2^2	145
E^2	236
B_2^1	287
E^1	299
A_1	305

3.3 Solar Cells based on CuInS$_2$

In a semiconductor the absorption of an incoming photon flux leads to an excitation of electrons across the band gap, if the photon energy is greater than the band gap energy. In general these excited electrons will recombine with a hole after a material specific life time. In solar cells the light generated electron-hole pairs are spatially separated, for example by the internal electrical field of a pn-heterojunction, before they can recombine.

The current transport across a pn-junction is characterized by two currents: the drift current caused by the electrical field in the space charge region of the junction and the diffusion current which flows in the opposite direction and is driven by the concentration gradient of the charge carriers across the junction. In thermal equilibrium the two currents cancel out each other. The jV-characteristics of an ideal diode in the dark can be described by an expression found by Shockley [85], the so called *ideal-diode equation*:

$$j(V) = j_{01}\left[\exp\left(\frac{V}{V_T A}\right) - 1\right],$$

with

$$j_{01} = \left(\frac{qD_p}{L_p} p_n + \frac{qD_n}{L_n} n_p \right) \qquad \textbf{(Eq. 3.9)}$$

Ideal diode means that no parasitic series or shunt resistances are considered and that recombination of the charge carriers within the space charge region of the junction are neglected. j_{01} refers to the saturation current density, which is determined by specific material properties of the semiconductors constituting the junction. The minority carrier concentrations are p_n and n_p, the diffusivities D_n and D_p and the diffusion lengths $L_x = (D_x t_x)^{-1/2}$ in emitter and base. t_x is the minority carrier life time. $V_T = kT/q$ is the thermal voltage and A is the so-called diode quality factor. j_{01} and A depend on the recombination mechanism which dominates the photovoltaic device. For qV >> AkT at room temperature **(Eq. 3.9)** can be approximated to

$$j(V) = j_{01} \exp\left(\frac{qV}{AkT} \right) \qquad \textbf{(Eq. 3.10)}$$

In **Fig. 3.7** a typical jV-characteristic of a solar cell is shown as it has been measured within this thesis. The jV-curve has been recorded in the dark (upper curve) and under illumination (curve at the bottom).

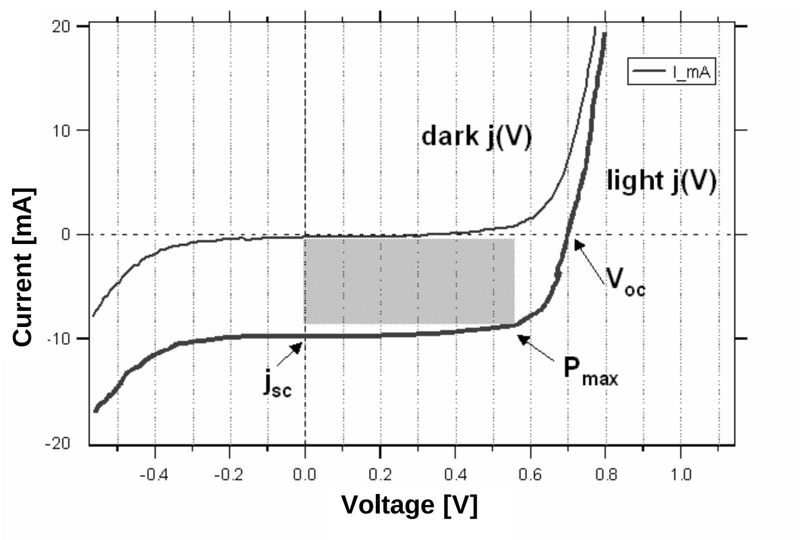

Fig. 3.7.: jV-characteristics in the dark (upper curve) and under illumination (bottom curve) of a typical $CuInS_2$-based solar cell as recorded within this thesis. The gray shaded rectangle gives the maximum area inscribed in the curves.

Under illumination excess charge carriers are generated in the solar cell. These non-equilibrium carriers will either recombine or be separated by the internal field in the space charge region. Thereby they cause an additional current density, j_{ph}, superimposed onto the diode current density. In this case **(Eq. 3.10)** turns into

$$j(V) = j_{01}\left[\exp\left(\frac{qV}{AkT}\right)-1\right]-j_{ph} \quad . \qquad \textbf{(Eq. 3.11)}$$

Here, the light generated current is assumed to be independent of the voltage across the junction. This photo current is also called short circuit current j_{sc} as it corresponds to the current observed at V = 0 mV in **Fig. 3.7**. Additionally, the open circuit voltage V_{oc} corresponds to the voltage at j = 0 mA. The maximum power which can be extracted from the solar cell is determined by the rectangle of maximum area inscribed in the jV-curve, indicated by the gray shaded rectangle in **Fig 3.7**. The efficiency ? of the solar cell is defined as

$$h = \frac{FF * j_{sc} * V_{oc}}{P} \quad , \qquad \textbf{(Eq. 3.12)}$$

where P refers to the incident power and FF, the fill factor, describes the shape of the jV-characteristics. The latter value is given by

$$FF = \frac{j_{\max} * V_{\max}}{j_{sc} * V_{oc}} \qquad \textbf{(Eq. 3.13)}$$

with j_{max} and V_{max} the current density and the voltage at the maximum power point, respectively.

If the pn-heterojunction is formed by different semiconductor materials band discontinuities might occur at the interface. In the case of $CuInS_2$-based solar cells the p-type material (absorber) is $CuInS_2$, while the n-type material consists of two layers: a buffer layer (CdS), and a transparent top layer (ZnO). These materials are characterized by their different optical band gaps: $CuInS_2$ 1.52 eV, CdS 2.4 eV and ZnO 3.2 eV. For details of the design of these solar cells see **chapter 4.1**. Depending on the conduction band offset ($?E_C$) two types of heterojunctions can be distinguished: type I or spike-like interfaces ($?E_C>0$) and type II or cliff-like interfaces ($?E_C<0$). $CuInS_2$-based photovoltaic devices are of type II. **Fig. 3.8** shows the schematic band diagram for a $CuInS_2$/ZnO heterojunction. The different locations of recombination, namely interface, space charge region, and bulk recombination (due to injection) are marked by vertical arrows, while possible tunneling enhanced recombination is indicated by horizontal arrows. The single recombination mechanisms will be elucidated at the end of this section. The shown diagram is based on data determined by Hengel et al. [86].

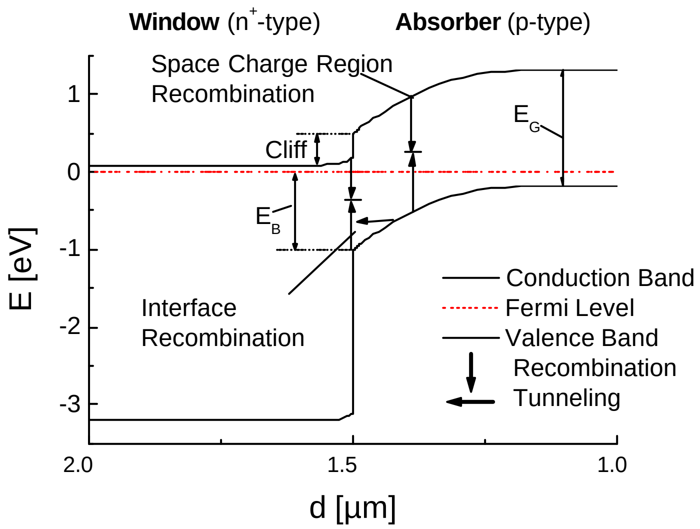

Fig. 3.8: Energetic band line-up of a $CuInS_2$/ZnO interface. The conduction bands at the interface show a cliff-like discontinuity. The recombination mechanisms are indicated by arrows (vertical: thermally activated, horizontal: tunneling enhanced).

The theoretical energy conversion efficiency of an ideal solar cell with a band gap of 1.52 eV has been calculated to be around 30 % [87]. However, the best conversion efficiencies currently reached by $CuInS_2$-based photovoltaic devices are 12.7 % [88, 89]. In **Tab. 3.8** the solar cell parameters j_{SC}, V_{OC}, FF and ? are listed for an ideal device with a band gap of 1.52 eV as calculated by Blieske et al. [87] and for a $CuInS_2$-based solar cell as measured within this thesis. It has been found that the device performance of $CuInS_2$-based solar cells is mainly limited by the open circuit voltage V_{OC}, which shows the largest deviation from the theoretical possible value (40%).

Tab. 3.8: Solar cell parameters calculated by Blieske et al. [87] for an ideal solar cell with E_g = 1.52 eV and measured solar cell parameters for a $CuInS_2$-based device from this work.

	ideal $CuInS_2$ solar cell	polycrystalline $CuInS_2$-based solar cell
j_{SC} [mA/cm²]	27.1	24.3
V_{OC} [mV]	1249	729.4
FF [%]	90.1	71.7
? [%]	30.5	12.7

To overcome this "V_{OC}-limitation" is a main task of the current research. So far, different attempts have been pursued.

a) Variation of the Cu/In ratio: The most efficient $CuInS_2$-based thin film solar cells have been achieved for a Cu-rich growth regime, where a secondary Cu-S phase is present during the film formation process. The existence of this copper-chalcogen binary phase has been found to be advantageous for the crystalline quality of the films, this will be discussed in detail in chapter **5.3**. The Cu-S phase segregates on top of the $CuInS_2$ layer and has to be removed by an etching step before buffer deposition (cf. **chapter 4.1**). In order to avoid this additional preparation step the stoichiometry of the metallic precursor layers has been varied down to the Cu-poor regime. Unfortunately Cu-poor prepared $CuInS_2$ films suffer from low carrier densities. However, with an additional doping step and using a stacked layer concept Watanabe et al. [90-92] achieved a photovoltaic energy conversion of around 10.6 % for those devices. An efficiency of approximately 8.3 % has been reported for Cu/In $\tilde{}$ 1 in case of coevaporation with no additional doping step by Scheer et al. [93]. Nevertheless, both attempts did not succeed in increasing V_{oc} significantly.

However, the improvement of chalcopyrite-based photovoltaic devices is still mainly based on empirical experiences, as the influence of the preparation conditions on the device performance is poorly understood. To close this gap it is important to investigate the growth of the material under different conditions. *In-situ* investigations carried out within this thesis will give a detailed insight into the growth mechanisms and clarify for example the role of Cu-S phases during the growth (cf. **chapter 5.3**). Furthermore, a systematic structural investigation of completed films in combination with a characterization of the photovoltaic devices has been performed. This will detail how the structural quality of the films influences the device performance (cf. **chapter 6**).

b) Incorporation of doping elements: It has been shown for $CuInSe_2$ that alloying and doping is a promising way to achieve higher V_{oc} values. Best $CuInSe_2$-based devices have been achieved by substituting In partially by Ga and by a controlled Na doping. Braunger et al [94] could explain this improvement by an enhanced affinity of Na and Ga towards Se, i.e. a better Se incorporation in the films. Furthermore the Ga contribution leads to a shift of the band gap towards higher values.

In general the incorporation of an isovalent or non-isovalent atom influences the effective defect concentration [95]. This is partly due to Fermi level dependent defect formation which is characteristic for this type of compound semiconductors [96,97]. However, self compensation restricts the doping of these materials to certain limits [98].

For $CuInS_2$-based thin films several authors [92,99-101] succeeded with the concept of Ga incorporation into the absorber layer using different growth techniques. Neisser achieved the highest value for V_{oc} of around 830 mV. Further concepts have been pursued by doping with a variety of impurities. For example, small amounts of Zn in the $CuInS_2$ layers lead to higher V_{oc}-values in the device [102]. For the incorporation of sodium in the films Watanabe and coworkers found an improvement of the solar cell parameters for Cu-poor prepared devices. However, for Cu-rich devices this approach did not lead to an increased V_{oc} [9]. Based on the work of Watanabe and the findings for $CuInSe_2$, sodium seems to play an important role during the growth of Cu-poor prepared films. However, the mechanism how sodium can influence the crystal growth is still unclear. Thus, *in-situ* experiments on the growth of $CuInS_2$ films doped with sodium have been performed in order to detail this point (cf. **chapter 5.3**).

c) Modification of the interface: Obviously, in heterojunction devices the energetic band line-up of the absorber/window layer interface plays an important role for the behavior of the diode. Numerical device simulations performed by Klenk [103] pointed out the importance of the interplay between electronic properties and the band line up. Hence, a modification of the n-type side might be successful. For that the deposition of the buffer layer [104] and the buffer layer material itself [105-107] have been modified. Especially with the adjustment of the deposition conditions of the buffer layer Braunger et al. achieved a significant increase of V_{oc}. However, none of the buffer layer modification attempts succeeded in a V_{oc} above 740 mV.

In addition to a detailed investigation of the growth mechanism of $CuInS_2$ films, it is desirable to identify and quantify these factors which cause a deterioration of the open circuit voltage. Defects in the absorber layer, the recombination mechanism at the absorber/window interface and their interplay have consequences on the electronic properties of the photovoltaic device. For polycrystalline thin film materials it is well established that the films are characterized by a high defect density. Therefore the dominating loss mechanism is due to recombination via defects. In $CuInS_2$ 12 different intrinsic point defects exist - 6 antisites (Cu_{In}, Cu_S, In_{Cu}, In_S, S_{Cu}, S_{In}), 3 vacancies (V_{cu}, V_{In}, V_S), and 3 interstitials (Cu_i, In_i, S_i) - which form electronic states within the band gap. In **Tab. 3.9** the defects are listed together with their corresponding assignment to acceptor or donator states and their formation energies E_f [108-112]. The occupation of S-sites with one of the metal atoms and vice versa, respectively, is unlikely due to the high formation energies [108,113]. Therefore those defects are not listed in **Tab. 3.9**. Some defects show a high tendency to form complexes. Zhang and coworkers [114], for example, predicted for the $CuInSe_2$ system an electrically neutral defect complex ($In^{2+}_{Cu}+2V^{-}_{Cu}$) with very low formation energy. They further assumed that the periodic repetition of this defect complex leads to so-called "ordered vacancy compounds" (OVC) like $CuIn_3Se_5$ or $CuIn_2Se_{3.5}$.

Tab. 3.9: Possible point defects in $CuInS_2$ together with their respective state and formation energy.

Defect	Cu_{In}	In_{Cu}	V_{Cu}	V_{In}	V_S	Cu_i	In_i	S_i
State	A	D	A	A	D	D	D	A
E_f [meV]	150	110	100	150	35	?	70	150

As mentioned before, the value of j_{01}, especially its temperature dependence, and the value of the diode quality factor A are dependent on the dominating recombination mechanism. In general different recombination mechanisms are possible (cf. **Fig. 3.8**), such as for example recombination in the space charge region and at the interface. Additionally, the recombination can be of thermally activated or tunneling enhanced character. It is possible to introduce this temperature dependence by an additional exponential term. Then the diode equation **(Eq. 3.10)** turns into

$$j(V) = j_{00} \exp(-E_A/AkT) \exp(qV/AkT) \quad \textbf{(Eq. 3.14)}$$

The resulting dependence of the activation energy E_A and the diode quality factor are listed in **Tab. 3.10**. The simplest case (a) is given for an abrupt pn-junction. Then the jV-characteristic is diffusion limited and recombination takes only place in the neutral region of the absorber. For this the width of the space charge region must be small compared to the neutral region. Usually, this is not the case for thin film solar cells. A diode quality factor A of 2 is given if Shockley-Read-Hall recombination in the space charge region is dominant [115] (case (b) in **Tab. 3.10**). If the recombination centers are exponentially distributed (case (c)), then the diode quality factor is additionally determined by the characteristic energy E* of this distribution [116]. If tunneling enhanced recombination is possible (case (d)), then A is dependent on the characteristic tunneling energy E_{00}. A similar behavior for thermally activated and tunneling enhanced recombination is found if the recombination takes place at the interface (case (e) and (f)) [116-118]. Then the activation energy is not determined by E_g anymore, but by F_b, the difference between the Fermi level and the upper valence band at the heterojunction.

Tab. 3.10: Diode quality factor A and activation energy for different recombination mechanisms. For details see text.

Dominating Recombination Mechanism	Diode Quality Factor A	Activation Energy E_A
(a) recombination in neutral region	1	E_g
(b) recombination in space charge region	2	E_g
(c) – via band tails	$2/(1+kT/E^*)$	E_g
(d) – tunneling enhanced	$2/(1+kT/E^*-E_{00}^2/3(kT)^2)$	E_g
(e) recombination at the interface	1	F_b
(f) – tunneling enhanced	$(E_{00}/kT)\coth(E_{00}/kT)$	F_b

Reiss [119] found for sequentially prepared $CuInS_2$-based solar cells tunneling enhanced interface recombination for the dark current voltage characteristics and a combination of tunneling enhanced and thermally activated interface recombination for the jV-curves under illumination. For interface recombination the open circuit voltage can be written as

$$V_{oc} = \frac{\Phi_b}{q} - \frac{kT}{q}\ln\left(\frac{qS_p N_V}{j_{ph}}\right) \quad , \qquad \textbf{(Eq. 3.15)}$$

where S_p is the surface recombination velocity of the holes and N_V is the effective density of states in the valence band. It follows from **(Eq. 3.15.)** that V_{oc} is determined by the rate of recombination of the minority charge carriers. It is remarkable that here, in contrast to the case of recombination within the space charge region, the activation energy (E_A) of the saturation current density is given by the value of F_b. In the case of thermally activated interface recombination the diode quality factor is given by

$$A = 1 + \frac{N_A^*}{N_D} \quad . \qquad \textbf{(Eq. 3.16)}$$

However, an asymmetric doping ($N_D > N_A$*) is a good assumption for the investigated CuInS$_2$/CdS heterojunctions. N_A* describes the effective doping by acceptors. In this case A is between 1 and 2. For tunneling enhanced recombination the diode quality factor is temperature-dependent and can take values larger 2. Then, using **(Eq. 3.15)** the diode quality reads

$$A = \frac{E_{00}}{kT} \coth\left(\frac{E_{00}}{kT}\right) \quad , \qquad \textbf{(Eq. 3.17)}$$

and V_{oc} is expressed by

$$V_{oc} = \frac{\Phi_b}{q} - \frac{AkT}{q} \ln\left(\frac{J_{oo}}{J_{ph}}\right) \quad , \qquad \textbf{(Eq. 3.18)}$$

where E_{00} is the characteristic energy of tunneling. E_{00} is determined by N_A* and J_{00} is the saturation current density.

Considering the discussed transport properties of CuInS$_2$-based solar cells the interface recombination and the enhancement of tunneling have been identified to be important factors, which influence and limit the open circuit voltage. However, it is still an open question how the structural quality of the absorber layers can influence the recombination mechanism. In this thesis the diode quality factors A, which give a clear indication for the dominating recombination mechanism, and the crystal quality - as determined with Raman spectroscopy - of a large sample set has been investigated to answer this question (cf. **chapter 6.2**).

Chapter 4

Experimental procedure

In the first part of this chapter a short introduction into the design of chalcopyrite-based heterojunction solar cells is given. This will be followed by a description of the fabrication process of the samples. Two different methods for the sulfurization of Cu/In precursor layers were used, namely rapid thermal and conventional thermal processing (RTP and CTP). While *ex-situ* measurements on absorber layers and completed solar cells have been performed on RTP sulfurized samples, the design of the sulfurization chamber for the *in-situ* experiments during the growth of the films requires a CTP process. It was part of this work to design a sulfurization chamber in order to perform *in-situ* Raman experiments. In the second part of this chapter the experimental setup of *in-situ* and *ex-situ* measurements is given in detail.

4.1 Preparation of $CuInS_2$-based Thin Film Solar Cells

In general solar cells consist of light absorbing material interlaced by a front and a back contact. Electron-hole pairs can be generated in the absorber layer by absorption of light. Thus, the absorption process can be understood as the conversion of heat (heat radiation of the sun) into chemical energy. In order to separate these charge carriers and to allow a constant electric current to the contacts, the solar cells must contain a so-called semi-permeable membrane (SPM). Within such a membrane the conversion of chemical into electric energy takes place.

Such SPMs can be realized with different concepts. Often found concepts are pn-junctions. These are known as heterojunctions if the p- and n-layer are of different materials. The layer - p- or n-type -, where most of the light is absorbed, is called the absorber layer. Such a pn-junction leads to the formation of an internal electric field, which can be understood as the origin for the separation of the generated electron-hole pairs. Important for this concept is that the separation of the charge carriers takes place before they can recombine. The separation of the charge carriers results in an electrical potential, which can be used to drive an electric load.

In the case of chalcopyrite-based solar cells, the pn-junction is a heterojunction formed by a p-type chalcopyrite absorber layer and a transparent n-type window layer. Typically, such chalcopyrite heterojunction solar cells show the layer sequence as depicted in **Fig. 4.1**.

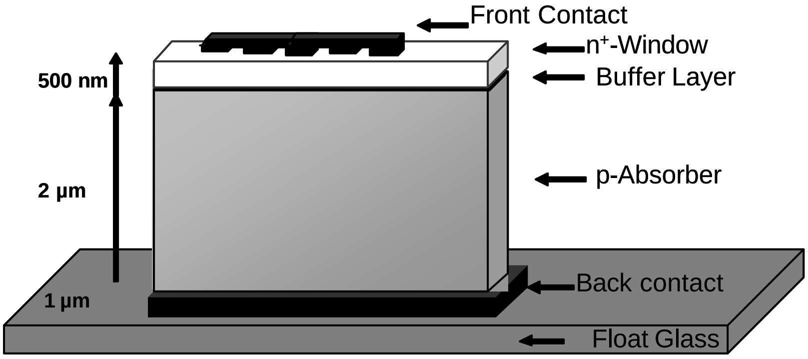

Fig. 4.1: Schematic design of a $CuInS_2$-based heterojunction solar cell.

Conventional float glass with a thickness of around 1 mm serves as the substrate to ensure mechanical stability of the later device. The glass is coated by sputtering technique with an approximately 1 µm thick molybdenum (Mo) layer, which has the function of a back contact. Mo is usually preferred as its thermal expansion coefficient is similar to that of glass. Then, large stress gradients along the Mo/glass interface can be avoided after completion of the device. Such stress gradients might lead to a lower mechanical stability (adhesion) of the device and might therefore influence the electrical behavior of the absorber.

The absorber layer consisting of p-type $CuInS_2$ is located on top of the Mo back contact. Due to the high absorption coefficient of this material, a thickness of around 2 µm is sufficient to absorb the incident sun light. The heterojunction is completed by a thin (0.05 µm) n-type cadmium sulfide (CdS) buffer layer and an n/n^+ type zinc oxide (ZnO) double-layer (0.1 µm/0.5 µm). The CdS- and ZnO-layers are transparent for light in the visible range as their optical band gaps are 2.4 eV and 3.2 eV, respectively. Therefore the combination of the CdS- and the ZnO-layer is referred to as the window layer. Finally, an additional Ni/Al grid, acting as front contact, is deposited.

In the following the different preparation steps of a standard baseline process as it was developed by Klaer and coworkers [6,89,120-123] are outlined, cf. **Fig. 4.2**.

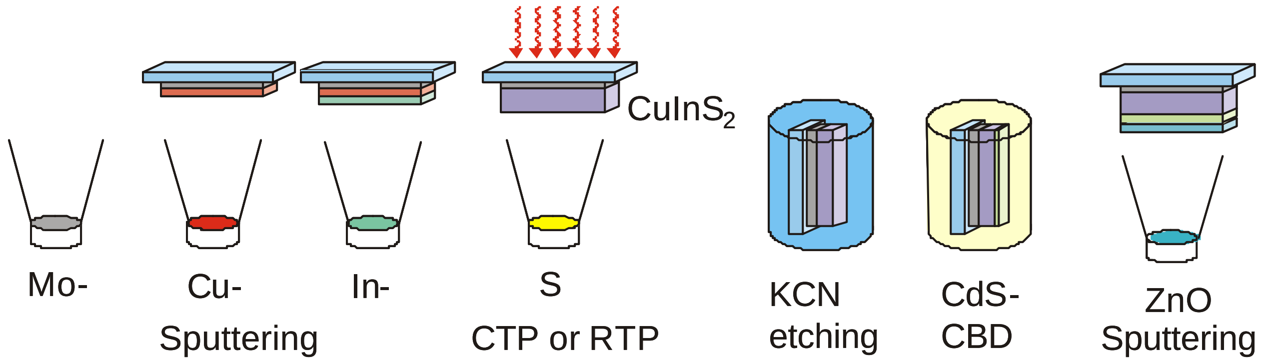

Fig. 4.2: Schematic presentation of the fabrication procedure of CuInS$_2$-based thin film solar cells as developed by Klaer and coworkers [6,89,120-123].

The metal layers (Mo, Cu and In) are deposited subsequently on top of each other by a DC magnetron sputtering process. The layer thickness is determined by time and power used for the sputtering process. The chosen thicknesses of the Cu and In layers determine the Cu/In ratio of the so-called precursor films. The sputtering process is followed by a sulfurization step of the metallic Cu and In layers. The formation of CuInS$_2$ takes place during heating the metallic precursor layers in sulfur atmosphere. Two different sulfurization processes have been used within this work: conventional thermal processing (CTP) and rapid thermal processing (RTP). The main difference between these two techniques is the design of the heater.

In the RTP small pieces of elemental sulfur are put beside the precursors and both are heated together by a lamp field. Because of the low thermal mass of this system rapid heating (10 K/sec) can be realized. At the peak of highest temperature of around 500 °C the samples are annealed for approximately 3 minutes. The cooling of the samples is passive. This sulfurization process is characteristic for the so-called standard baseline process, which has been developed in order to allow an up-scaling to large areas. The samples investigated *ex-situ* have been prepared by such a RTP process.

For the *in-situ* investigation of the sulfurization process a modified chamber (cf. **Fig. 4.3**) has been used. In this system the sulfurization proceeds slowly and sulfur vapor is provided by a Knudsen source from elemental sulfur. At a working temperature of around 190 °C this source provides a sulfur partial pressure of around $1 \cdot 10^{-4}$ mbar. The heating of the substrates up to around 500-550 °C (0.5 K/sec) has been realized in this case by thermal radiation of a graphite heater followed again by passive cooling. For the temperature measurement a thermocouple was placed between the backside of the substrate and the heater. In contrast to the RTP process, in a CTP process the sulfur partial pressure and the substrate temperature are independent from each other.

Depending on the deviation of stoichiometry of the elemental composition, the growth regimes are divided into Cu-poor (Cu_xIn with $x < 1$) and Cu-rich (Cu_xIn with $x > 1$) ones. It has been reported by several authors [7,89] that Cu-rich prepared $CuInS_2$-based solar cells exhibit the best device performance. Therefore the conventional preparation of $CuInS_2$ absorber layers occurs with copper excess. Due to this Cu excess CuS forms on the surface of nearly stoichiometric $CuInS_2$ layers. This Cu-S binary phase can be easily removed via etching with KCN (l). Nevertheless, within this thesis Cu-poor growth processes have also been analyzed, in order to investigate the differences to the Cu-rich ones. It has been pointed out in **chapter 3.3** that doping with sodium can yield better device performances for Cu-poor grown films. In order to investigate its influence on the growth path of $CuInS_2$, sodium has been introduced as a layer of NaF between Mo and Cu by thermal evaporation.

Apart from Mo sputtering, the process steps described so far are known as the absorber preparation. In the next step a thin CdS buffer layer is deposited by chemical bath deposition at a temperature of 60 °C. The ZnO-layers are sequentially deposited by RF magnetron sputtering from a ZnO and a ZnO:Al target, respectively. Finally; for the deposition of the front contacts (Ni/Al) e-gun evaporation is used.

4.2 *In-situ* Raman and EDXRD Process and Measurement Setup

4.2.1 The Sulfurization Chamber

The sulfurization chamber used for real-time analytical experiments during growth and annealing of absorber layers at various conditions has been constructed in order to satisfy the experimental requirements of the EDXRD and Raman measurements. The setup had to be flexible as different experimental systems - EDXRD and Raman - have been used. Also the experiments were performed at different locations. **Fig. 4.3** shows a sketch of the portable sulfurization chamber. For sake of clarity the XRD (left) and Raman (right side) modifications of the chamber are not shown together. The core of the setup is the vacuum chamber connected with a turbo molecular pump. Inside the chamber a substrate holder with a graphite heater has been installed. The chamber has two windows made of capton foils through which x-ray radiation can be coupled in and out. An additional optical window has been mounted, through which the Raman laser light is coupled into the chamber. As the Raman measurements were performed in a backscattering geometry the incident and scattered beam passes the same window.

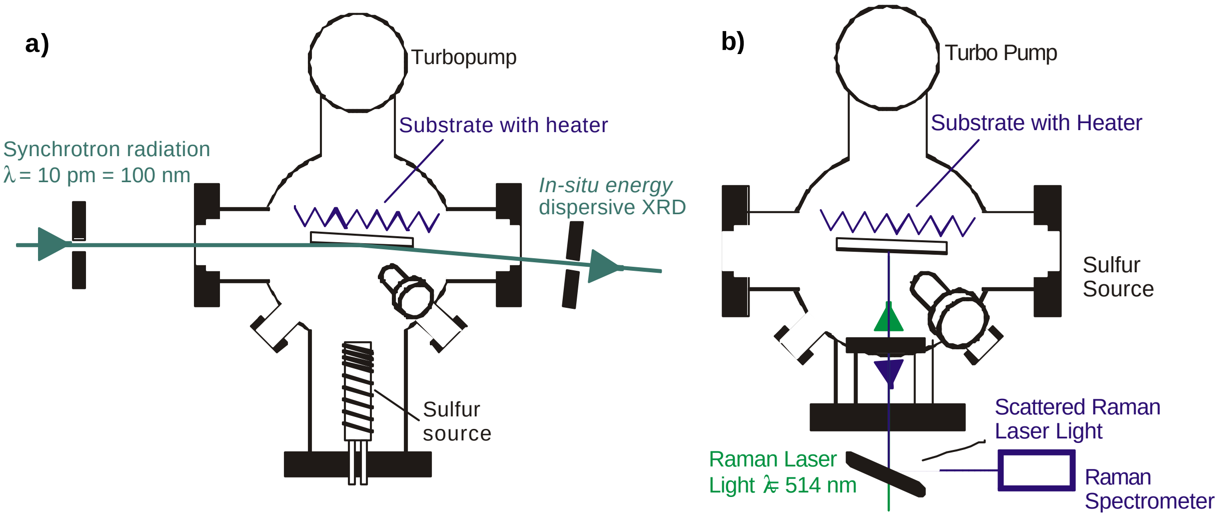

Fig. 4.3 a), b): Sketch of the sulfurization chamber with the possibility of *in-situ* EDXRD **a)** and *in-situ* Raman **b)** measurements. A simultaneous recording of EDXRD and Raman spectra required the mounting of additional flanges.

4.2.2. The EDXRD Setup

For the EDXRD *in-situ* experiments white synchrotron radiation has been used [124]. These measurements were performed at the beamline F3 of the “Hamburger Synchrotron Laboratory” (HASYLAB) at DESY (“Deutsches Elektron Synchrotron”). The HASYLAB is connected with the positron storage ring DORIS. The positrons emit photons in a continuous energy range and energies between a few meV and 100 keV are available. A characteristic value for X-ray radiation sources is their brilliance B. The brilliance is determined by the number of emitted photons N per time t, divided by the solid angle dO, the area of the emission dF and the relative energetic resolution dE/E

$$B = \frac{N/t}{d\Omega dF(dE/E)} \quad . \qquad \textbf{(Eq. 4.1)}$$

With a photon energy of around 20 keV and dF ˜ 1 mm^2 typical values of brilliance for the synchrotron radiation at DORIS are ˜ $2 \cdot 10^{13}$ photons / (sec·mm^2·0.1 % energy range). Thus, the brilliance value produced by the synchrotron radiation is a few magnitudes higher than those achieved by conventional radiation sources, such as X-ray tubes. Because of this high value of brilliance and this high intensity from the synchrotron radiation it is possible to achieve a time resolution of 15 sec per spectrum for the EDXRD measurements.

A germanium-based crystal has been used as the detector. The relative energetic resolution of the photon energy is around 1 %, and is determined by the quality of the germanium crystal [125]. For further details to this detector see Ref. [126]. A multi-channel analyzer is connected to the detector, in order to record the data. This analyzer consists of 2048 channels and has an energetic resolution of 26 eV per channel. The number of reflected photons at a different energy E were detected under an angle of 2T, which is defined by the direction of the incident and reflected beam, respectively, to the sample. Using Bragg's law **(Eq. 2.21)**, the d-spacings can be calculated from their energetic positions with the following equation

$$d[nm] = \frac{0.6199}{\sin \Theta E[keV]} \quad . \qquad \textbf{(Eq. 4.2)}$$

The diffraction angle T has been defined by the intersection point of the centerline of the primary (synchrotron) beam with the sample. For the investigated samples it has been chosen to be 3.7° in order to avoid an overlap between fluorescence and diffraction peaks.

For maximum intensity at the needed resolution a width of 300 µm for the collimator slit as well as for the detector slit has been used. The error of the aperture is proportional to the slit width. Therefore the diffraction angle calibration had to be carried out in reflection configuration. This configuration has been used for the *in-situ* experiments. However, for such a configuration T depends on the angle between the primary beam and the substrate surface. Due to the experimental conditions, the sample position inside the chamber is not well defined, as the rotational axis of the sample is unknown. Rotation of the sample changes the active sampled volume of the measurement. By the use of a Mo-coated glass substrate, the sample position and rotation have been adjusted due to the maximum intensity of the Mo_{Ka} fluorescence line. For this configuration the maximal intensity corresponds to T = 3.7 °. The calibration of the diffraction angle has been performed by means of the positions of the diffraction reflexes of gold powder on a Mo coated glass substrate.

The intensity of the synchrotron beam changes with time as a result of collision between the positrons and the residual gas inside the storage ring. Therefore all spectra have been normalized with respect to the intensity of the Mo_{Ka} fluorescence line. The recorded energy range was between 7 and 56 keV, which covers the energetic position of the peaks of interest for the investigated samples. The analysis of the spectra has been performed by the use of the program EDXPowd (RTI GmbH).

Theoretically, the shape of fluorescence lines and diffraction peaks are represented by Lorentzians. However, the observed line shapes are determined by the energetic resolution of the detector, which results in a broadening of the lines. Therefore the fluorescence lines as well as the diffraction peaks are fitted by a Gaussian. Only the Mo (110)-reflex, the most intense peak, required a Voigt profile for its fitting.

4.2.3 The Raman Setup

For the *in-situ* Raman experiments two different Raman systems have been used. The setup required a flexible coupling of the Raman laser light into the sulfurization chamber and onto the sample. One part of the *in-situ* Raman experiments, the annealing experiments (cf. **chapter 5.1**), have been performed at the university of Barcelona using a macro-Raman system. The second part of the *in-situ* experiments, the growth experiments, took place at the HASYLAB (DESY), in order to perform simultaneously *in-situ* EDXRD and *in-situ* Raman experiments (cf. **chapter 5.3**). The latter Raman system (Renishaw) was equipped with a fiber optic. All *in-situ* Raman experiments have been performed in backscattering geometry (cf. **Fig. 2.1**).

In general Raman systems consist of four main components: an excitation source, an optical filter which rejects the intense Rayleigh scattered light, a spectrometer which disperses the Raman scattered light into its components, and a detector which is connected to the spectrometer. Excitation is achieved by a laser source. As mentioned in **chapter 2.1** the intensity of Rayleigh scattered light is much higher than the intensity of Raman scattered light. Thus, if the Rayleigh scattered light enters the Raman spectrometer unattenuated, it will generate stray light which obscures the Raman spectrum. Different techniques to attenuate the Rayleigh light can be used. The choice of a technique depends on the spectral range of interest. In the following a few examples for optical methods are mentioned, as those are usually used when exciting with light in the visible spectral range. A band pass or band rejection filter serves as the simplest Rayleigh rejection device. These devices allow the measurement of Raman frequency shifts larger than 200 cm^{-1}. Holographic notch filters are available for the visible and near IR spectral regions. These filters typically permit Raman spectral measurements of frequency shifts > 100 cm^{-1}. A holographic notch filter selectively rejects a narrow band of light via Bragg diffraction. For more details about these filters see Ref. [127]. Multistage Raman spectrometers are typically required to measure Raman shifts in the range of 50 cm^{-1} when using excitation light in the visible. These so called pre-monochromators contain multiple dispersive elements (gratings) and spatial filters (slits). The different spectrometer stages reduce the Rayleigh light successively, while a triple monochromators enables a decrease of the stray light by a factor of 10^{-12}. However, the high rejection efficiency of that method is accompanied by a loss of the intensity of the Raman scattered light. For more details see Refs. [128,129]. The actual Raman spectrometer separates the Raman scattered light into its component frequencies. The most common concept for such a Raman spectrometer utilizes a holographic dispersive grating and a CCD (charge coupled device) multi-channel detector. The resolution of these spectrometers is determined by their optical focal lengths as well as the ruled line density of the grating.

The *in-situ* Raman annealing experiments have been performed at the University of Barcelona using a T64000 Jobin Yvon Raman setup. This Raman system provides a spectral resolution of 0.4 cm^{-1}. An excitation wavelength of 514.5 nm of an Ar^+ laser has been used. For light of this wavelength a penetration depth of 150 nm in $CuInS_2$ has been calculated [66]. The laser spot size on the sample was around 1.0 μm^2. The Jobin Yvon system consists of a multistage spectrometer. Three diffraction grids with 1800 lines/mm each build up the optical dispersive system, while simultaneously attenuating the Rayleigh scattered light. The system has been used in the additive mode. This means that the scattered light passes the three grids sequentially. At the exit of the third dispersive stage a multi-channel CCD detector is installed.

For the experiments a balance between the recording time and the density of power of the laser on the sample must be found. A too high power can lead to damages of the sample, which might change the chemical or structural properties. It has been found empirically that the damage threshold for the power on the sample is around 85 mW, which corresponds to an area density of laser power on the samples of around $6 \cdot 10^7$ W/cm^2. Higher values lead to macroscopic changes of the sample surface, which can be detected with a light microscope. In **Fig. 4.4** an example for such a change of the surface is shown. The deformation indicated by the dark area is in the range of the laser spot size (around 1 µm^2) and resulted from a laser power of around 100 mW. Thus, compromising between time resolution and signal intensity, the Raman pattern could have been taken with a time resolution of 60 sec.

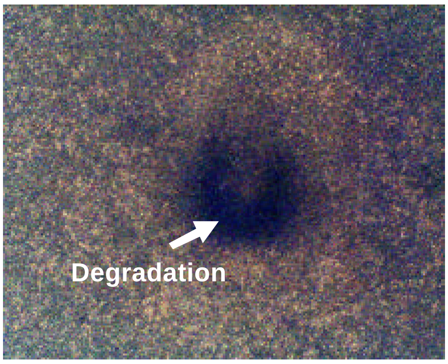

Fig. 4.4: Light microscope picture of the surface of a $CuInS_2$ sample after applying a laser power of around 100 mW with a magnification of 100. The dark patch corresponds to the damaged film area.

For the *in-situ* growth experiments a portable Renishaw System 100 Raman Analyzer was used. Again an Ar$^+$ laser (514.5 nm, Spectra-Physics) has been used as excitation light. The laser power on the sample was around 7 mW which corresponds to an area density of power on the samples of around $2 \cdot 10^6$ W/cm^2, assuming a spot size of 1 µm^2. The control unit of this system houses an additional light source (HeNe 100) which is used as a wavelength calibration standard, a single-stage spectrometer and the detector. The spectrometer has f/1.4 optics, and a single diffraction grating mounted on a Renishaw encoded grating stage. The detector was a Renishaw RenCam electrically-cooled (-70 °C) CCD, which offers a high signal-to-noise ratio.

The fiber optic probe, through which the Raman laser light was coupled in the chamber, has been especially designed for the chamber and specified for the used laser wavelength. Lenses of different focal lengths can be connected with the probe. For the shortest recording times at highest signal intensity a lens of 5 cm focus length has been chosen. Thus, a time resolution for the Raman spectra of 60 seconds has been achieved. The spectra have been recorded with the WIRE software GRAMS/32 provided by Renishaw.

4.3 *Ex-situ* Raman Measurement Setup

For the ex-situ Raman measurements a micro-Raman spectrometer DILOR/ISA LabRAM 010 with a microscope objective was used. The DILOR/ISA system consists of a tripel monochromator which is used in the additive mode. The gratings were chosen to 1800 lines/mm with a slit size of 100. A spectral resolution of 1 cm^{-1} has been achieved.

Raman spectra of absorber layers and completed solar cells have been recorded using this setup. In the case of solar cells, the laser light was applied to the absorber layer through the ZnO/CdS window layer. For best signal-to-noise-ratio the red light of a HeNe-Laser with an excitation line of 632.82 nm has been used. The light absorption in the ZnO-, respectively the CdS-layer can be estimated from the spectral response as will be shown later (cf. **chapter 6**). Considering the absorption coefficient of $CuInS_2$ from Ref. [66] as an approximate value, the penetration length of the laser light has been calculated to approximately 200 nm. Thus, the sampled depth of the absorber film roughly corresponds to the width of the space charge region within $CuInS_2$ [130]. Nominally, the spot diameter of the excitation light is around 1 µm on the sample surface. The area density of power on the samples has been calculated to be around $7{\cdot}10^5$ W/cm^2. Up to this laser power no changes of the sample surfaces or degradations have been observed. All *ex-situ* Raman experiments took place at room temperature and in ambient air. The spectra were accumulated twice at 300 sec.

The experiments were analyzed using a Lorentzian as underlying fitting function for the shape of the Raman peaks. A typical Raman spectrum of a $CuInS_2$ sample as recorded within this thesis is shown in **Fig. 4.5**. Such a Raman spectrum is usually not only composed of isolated spectral lines. Additional disturbing signals like fluorescence, cosmic radiation, or electronic noise of the detector appear. In **Fig. 4.5** exemplary signals related to cosmic radiation have been marked, while the background of the spectrum is due to fluorescence. For a consistent analysis of the spectral lines – for example the intense peak at around 300 cm^{-1} in **Fig. 4.5** - these disturbing signals must be separated from the Raman scattering intensities in order to obtain the “undisturbed” Raman spectrum. Signals due to cosmic radiation are characterized by high intense peaks of only few pixels. These as well as the electronic noise can be easily removed with a computational algorithm. The fluorescent background varies from sample to sample. A linear background removal has been performed on selected ranges of interest.

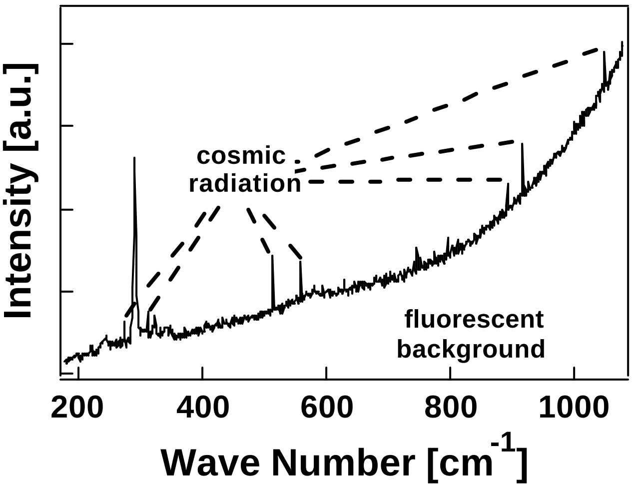

Fig. 4.5: Typical Raman spectrum of a chalcopyrite-based solar cell with a broad fluorescent background and some signals related to cosmic radiation.

The Raman peak shapes from the corrected Raman spectrum sensitively depend on the type of background removal: Using different correction procedures might result in different line shape profiles – for example a Voigt- or Gauss-profile instead of a pure Lorentzian profile - for the actual Raman bands. In order to assure comparability of the analyzed samples and consistency of the analysis, it is important on the one hand to have identical or at least very similar conditions during the measurements and on the other hand to use the identical correction procedures. This has been carefully done for the investigated samples and the Raman peaks are well represented by Lorentzian line shapes. On the basis of these Lorentzians the peak position, the full width at half maximum (FWHM), and the integrated (areal) intensity, in the following just referred to as intensity, have been calculated.

Chapter 5

Real-time Structural Analysis of the Growth of Cu-In-S Thin Films

The growth regime - Cu-poor or Cu-rich - of the absorber layers is known to influence the performance of $CuInS_2$-based solar cells: A Cu-rich preparation leads to a good performance of the photovoltaic devices, whereas a Cu-poor preparation yields a poor performance. An increase in performance for devices prepared in a Cu-poor regime can be achieved by doping the absorber layers with sodium. The origin of these performance differences may be found in the growth path, i.e. the phase transformation sequence, of the absorber layers. In order to clarify this difference *in-situ* Raman and EDXRD experiments have been performed simultaneously during the sulfurization (CTP process) of CuIn precursor layers with different Cu/In-ratios and additionally supplied sodium. The combination of both methods yields a detailed insight into the growth path of $CuInS_2$, as by EDXRD the entire absorber volume can be investigated, whereas Raman spectroscopy is sensitive to the surface-near region (information depth of around 150 nm). Further, by means of Raman spectroscopy, the different crystalline phases of $CuInS_2$, such as the chalcopyrite (CH) and the CuAu (CA) phase, can be distinguished (cf. **chapter 3.2**). For an unambiguous identification of the phase transformations and transitions during the growth it is necessary to separate these from temperature-induced effects. To this end, *in-situ* annealing experiments have been performed by means of Raman spectroscopy. Furthermore, as binary phases participate in the growth of $CuInS_2$ as intermediates the sulfurization of pure Cu and pure In layers has been investigated.

The main focus of this chapter is on *in-situ* Raman spectroscopy, which has been introduced for chalcopyrite growth monitoring within this thesis. At first the annealing experiments of already completed $CuInS_2$ layers with different precursor compositions are presented. The second part deals with the sulfurization of pure Cu and In layers in order to allow the identification of binary phases. In the last part the sulfurization of CuIn precursors is investigated by means of simultaneous *in-situ* EDXRD- and Raman experiments.

5.1 Annealing of $CuInS_2$ Absorber Layers

The Raman spectrum of crystals and crystalline films can change with temperature. If film growth at varying temperature is inspected by means of Raman spectroscopy, knowledge on these inherent changes is required. In this section the temperature dependence of the Raman lines of completed $CuInS_2$ films grown from precursor layers with three different Cu/In-compositions are compared. These have been chosen exemplary from a variety of samples in order to illustrate the differences between Cu-poor and Cu-rich grown films. The preparation under Cu-rich conditions results in a double-layer system: $CuInS_2$ + CuS.

In order to reveal a possible influence of the CuS top layer on the temperature dependence of the $CuInS_2$ Raman lines, Cu-rich films with and without this top layer are investigated. Additionally, the temperature dependence of Raman lines related to Cu-poor prepared films doped with sodium is investigated. All samples have earlier been sulfurized in a standard RTP process. **Tab. 5.1** gives a survey of the investigated samples (a) – (e).

Tab. 5.1: Cu/In-ratio of the precursor layers and amount of sodium introduced between the Mo and Cu metallic layers of the investigated set of samples.

Sample	Cu/In	Na [nm]	
(a)	1.8	0	KCN etched
(b)	1.8	0	as grown
(c)	1.0	0	as grown
(d)	0.8	0	as grown
(e)	0.8	30	as grown

The annealing profile of the samples consists of a heating period up to 500 °C within 20 minutes, a holding period of 10 minutes at 500 °C, and a passive cooling to room temperature. The peak of highest temperature is well below the transformation temperature between the ordered chalcopyrite structure and the disordered zincblende structure [71] (cf. **chapter 3.2**). All experiments have been carried out in vacuum (around $5 – 1 \cdot 10^{-04}$ Pa). According to theory (cf. **chapter 2.1.3.2**) a pressure reduction should lead to a shift of the peak position towards smaller wave numbers. However, the pressure range investigated here is too small to allow the detection of a significant change of the peak position. Usually a pressure range of some GPa is needed to observe a clear effect. In such a case one expects a linear relation between the shift of the peak position and the pressure, which allows the determination of the Grüneisen parameter **(Eq. 2.15)**. The annealing of the samples took place in sulfur atmosphere (10^{-2} Pa) in order to avoid evaporation of sulfur from the films at elevated temperatures.

In **Fig. 5.1**, a survey of Raman spectra of samples (a), (b), (d), and (e) taken at room temperature is presented. The Raman spectra have been corrected with the procedures outlined in **chapter 4.3**. The two peaks at 290 cm^{-1} and 305 cm^{-1} can be assigned to the A_1-mode of the CH- and the CA-phase, respectively [64,131]. A clear discrimination between these two peaks and therefore a separate fitting, however, is not always possible. If the spectral range of the two A_1-modes is fitted by a single line, different peak positions are obtained depending on the dominant crystalline phase. An intermediate peak position indicates that both crystalline phases are present in the sample. Certainly, the shape of the peak is also affected by the presence of these two contributions and a single line fit results for example in a larger line width. However, in some cases it is even possible to detect both peaks well separated, as can be seen for sample (e) in **Fig. 5.1**. In addition, for sample (b) two peaks at 260 cm^{-1} and 470 cm^{-1} can be discerned, which have been assigned to the phase CuS.

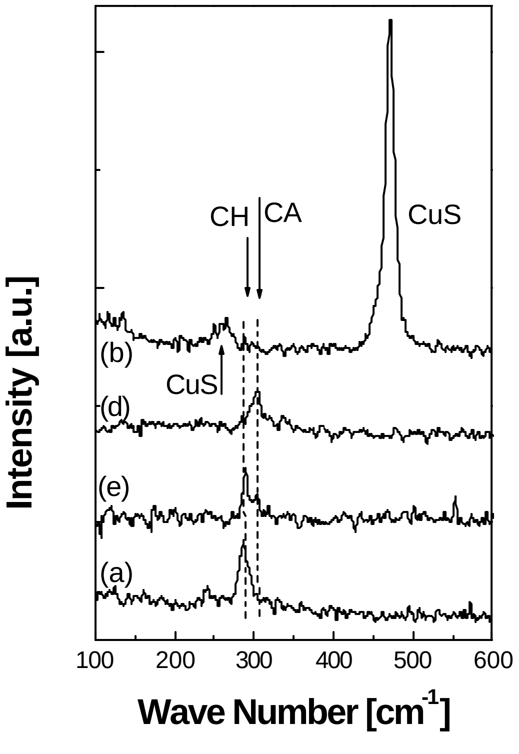

Fig. 5.1: Raman scattering intensities versus wave numbers for samples (a) Cu-rich (Cu/In = 1.8, etched), (b) Cu-rich (Cu/In = 1.8, as grown), (d) Cu-poor (Cu/In = 0.8, no Na) and (e) Cu-poor (Cu/In = 0.8, 30 nm Na). CH denotes the chalcopyrite phase of $CuInS_2$ and CA the CuAu-phase. The spectra are shifted vertically for sake of clarity.

The annealing experiments have been separated into three parts. At the beginning the temperature-induced effects observed for sample (a) are presented in detail as this sample reflects only the CH-phase of $CuInS_2$. This is followed by the presentation of the annealing experiments of samples (c) - (e). These will show the influence of different Cu/In precursor ratios and doping with sodium. In the last part of this section the annealing of an as grown $CuInS_2$ sample is presented, which will clarify the influence of the CuS top layer on the temperature dependence of the Raman bands related to $CuInS_2$.

5.1.1 Temperature Dependence of the Dominant $CuInS_2$ A_1-Mode

Fig. 5.2 a) shows six Raman spectra for sample (a) within the range of 200 and 400 cm^{-1} recorded during the heating period at different temperatures. The spectra are shifted vertically for sake of clarity. The high intense A_1-mode of CH-ordered $CuInS_2$ can be observed clearly at around 290 cm^{-1}, while the corresponding E- and B_2-modes appear weakly. Because of the short recording times of the spectra the E- and B_2-modes exhibit a low signal to noise ratio.

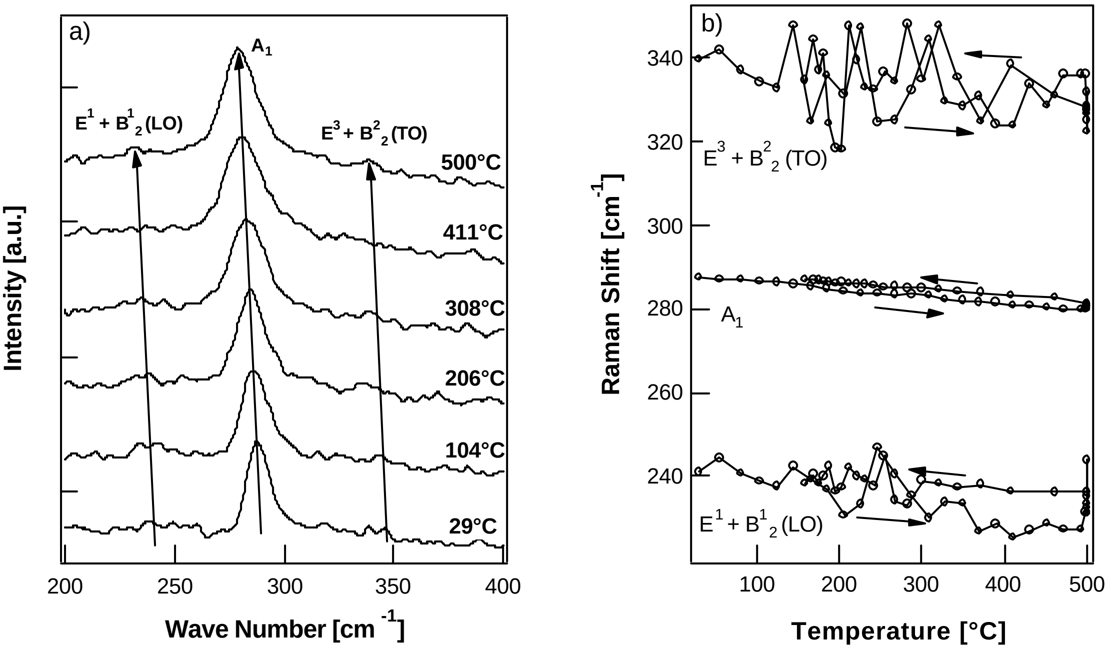

Fig. 5.2: a) Representative Raman spectra of sample (a) recorded at different temperatures in the heating period, the temperature-induced shift of the peak positions is indicated by the arrows. **b)** Raman shift of the line positions of the A_1-, B_2-, and E-mode for sample (a) as a function of temperature. The arrows represent the heating and the cooling periods.

In **Fig. 5.2 a)** a peak shift of all observed $CuInS_2$-modes can be seen as indicated by the arrows. Additionally, an increase of the temperature is accompanied by both, a broadening of the Raman line as well as an increasing intensity. In **Fig. 5.2 b)** the peak positions of the A_1-, B_2- and E-modes are presented as a function of the substrate temperature. The arrows indicate the heating and cooling period. Despite of considerable scattering of the peak positions for the B_2- and E-modes, all modes exhibit a shift of their peak position towards lower wave numbers with rising temperature. The resulting temperature coefficients for the different modes agree in their values and have been calculated to approximately $-5.7 \cdot 10^{-5}\,K^{-1}$. Thus, the different phonon modes of $CuInS_2$ exhibit the same temperature dependence. This means that we expect the same peak shift for the E- and B_2- modes as for the intense A_1-mode. Only small hysteresis can be observed for peak positions comparing the heating and cooling period.

Besides a temperature-induced peak shift, **Fig. 5.2 a)** also indicates effects on the Raman line width and the areal intensity. **Fig. 5.3** presents the FWHM and the areal intensity (in the following referred to as intensity) of the A_1-mode as a function of the substrate temperature for both the heating and the cooling period. A broadening of the line shape and an increase in intensity with rising temperature can be observed. For both trends (FWHM and intensity) a linear dependence on the temperature can be stated. An increasing intensity of the Raman modes is to be expected according to the Bose-Einstein statistics of phonons. The temperature-induced line broadening will be explained in the following.

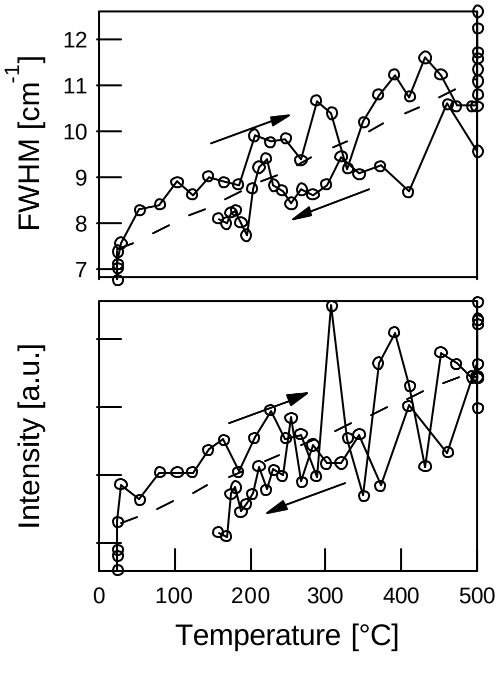

Fig. 5.3: FWHM and intensity of the A_1-mode versus the substrate temperature as obtained from a single Lorentzian fit for sample (a). The open dots are the measured data points, while the dashed line represents the linear temperature dependence. The arrows indicate the heating and cooling period.

The presented annealing experiment showed that an increase in temperature is combined with a shift of the peak position of the CH-ordered $CuInS_2$ A_1-mode towards smaller wave numbers. The amplitudes of the lattice vibrations increase with rising temperature and the influence of the crystal potential - modified by the anharmonicity of the lattice - on the atoms becomes stronger. From the temperature-induced frequency shift the Grüneisen parameter ? can be calculated using the relation $(\delta(\Delta ?_{q,f})/?_{q,f} = -\gamma(\delta V/V))$ (cf. **chapter 2.1.3.2**). It results from this relation that a decrease of the frequency position with rising temperature will occur if the Grüneisen parameter of the material has a positive value. With the thermal linear expansion coefficient of α ˜ $1.0\cdot10^{-5}\,K^{-1}$ for CIS (CH-phase) from Ref. [132] within the temperature range T = 200-600 °C γ has been calculated to 1.9 ± 0.1. Compared to the values of the Grüneisen parameters of related ternary compounds ($CuInSe_2$: $\gamma = 1.3$ [133], $CuAlS_2$: $\gamma = 1.6$ [134], $CuGaS_2$: $\gamma = 1.5$ [135]) this value appears to be slightly too high. This might be due to strain within the layers as the films are polycrystalline and attached to a substrate. Such a strain would be of dilatory character in the CH-ordered $CuInS_2$ layer, leading to an apparent increase of γ. For the intense E-mode of GaN Liu et al. [136] indeed found a slightly higher absolute frequency shift in a sample attached to a substrate than for a free standing sample. However, the value calculated here is still within the range between 1 and 2 as it is expected for semiconductors with a tetragonal structure [137-139].

The frequency shift can be assumed to be proportional to the temperature as the expansion within the investigated temperature range is relatively small. Nevertheless, such a linear correlation between the frequency shift and the temperature is an approximation. In this case only the first term of the Taylor expansion for the peak shift with temperature is taken into account. Terms of higher order, which describe phonon decay and 4-phonon processes, have been neglected so far in this calculation.

In the following a method to calculate the temperature dependence of the Raman frequency, which includes phonon decay processes, will be presented. The thermal coefficient of the Raman frequency can be described with perturbation theory (cf. **chapter 2.1.3.2**). Within this theory the self-energy of the phonons is expanded to varying orders in the phonon-phonon interaction. For silicon for example phonon-phonon interactions up to the forth order have been found [140,141].

Cui and coworkers [142] proposed an empirical expression which has been developed for the diamond structure:

$$w(T) = w_0 - \frac{A}{\exp(B\hbar w_0 / k_B T) - 1} \quad . \qquad \textbf{(Eq. 5.1 a)}$$

A and B are fitting parameters and $?_0$ is the phonon frequency at 0 K. This expression is based on the band gap renormalization by electron-phonon interaction in the Einstein approximation. This becomes clear, considering that renormalization of the gap by electron-phonon interaction also results in a renormalization of the phonon frequencies by the same mechanism.

The solid line in **Fig. 5.4** gives the simulation of the data points (open dots) according to **(Eq. 5.1 a)**, while the linear correlation is represented by the dashed line. Apparently, the expression developed originally for diamond can also be used to describe the temperature dependence of the $CuInS_2$ A_1-mode. **(Eq. 5.1 a)** results in $?_0$ = 289.78 cm^{-1}, A = 19.294 cm^{-1}, and B= 13.94. As can be seen in **Fig. 5.4** both, the fitting with **(Eq. 5.1 a)** and the linear regression as resulted from the Grüneisen approach describe the temperature dependence of the Raman mode frequency with good agreement. Thus, although the Grüneisen approach is a simplification, it can be used to describe the temperature-induced phonon shift.

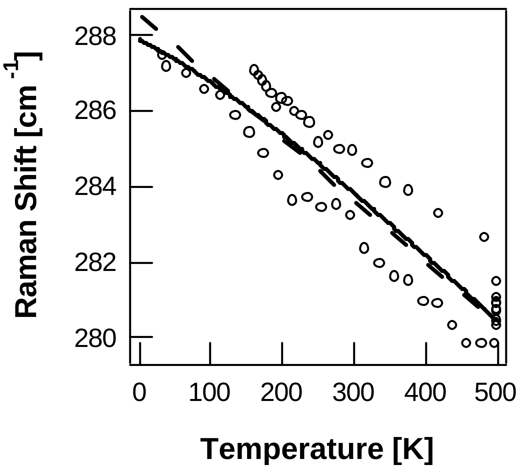

Fig. 5.4: Raman shift of the CIS A_1-mode versus the temperature. The open dots are the measured data points, the solid line gives the simulation using **(Eq. 5.1) a)** and the dashed line represents the linear correlation.

Using the here determined fitting parameters A and B, it is now possible to determine the temperature of CH-ordered $CuInS_2$ from the line position. Therefore **(Eq. 5.1 a)** must be inverted:

$$T = \frac{B\hbar w_0}{k_B \ln\{1 + A/[w_0 - w(T)]\}} \quad . \qquad \textbf{(Eq. 5.1 b)}$$

The values determined for the FWHM of the Cu-rich sample are higher (at least by a factor of 2) than those determined by *ex-situ* experiments (cf. Ref. [131]). This broadening might be caused by the experimental setup as well as the measurement procedure. Broadening due to the experimental setup can usually be removed by deconvoluting the Raman spectra, if the signal-to-noise ratio is above 100 [143]. Our short recording times for the spectra result in signal-to-noise ratios below 20. Thus, a deconvolution cannot be performed here. Nevertheless, a temperature-induced broadening of the phonon line shape can be observed. Assuming that the observed additional broadening is temperature independent, it can be described by an additive term G_{in}, cf. **(Eq. 2.14)**.

Underlying the Klemens model [36] (cf. **chapter 2.1.3.2**) the temperature dependence of the line width G is mostly determined by phonon decay processes of the first order. In this case the phonons decay into two phonons belonging to the same phonon branch with opposite wave vectors. Then G(T) can be expressed by

$$\Gamma(T) = \Gamma(0)[1 + n(w(\vec{q}, j_1)) + n(w(-\vec{q}, j_2))] = \Gamma(0)[1 + 2n(w_0/2)] \quad . \qquad \textbf{(Eq. 5.2 a)}$$

Here, n is the thermal Bose-Einstein occupation number, ?$_0$ corresponds to the Raman frequency at 0 K, and G(0) (2.0 cm^{-1}) is the FWHM at 0 K. ?$_0$ has been determined from **(Eq. 5.1 a)** to approximately 289.8 cm^{-1}. Considering the additional broadening then **(Eq. 5.2 a)** turns into

$$\Gamma'(T) = \Gamma(T) + \Gamma_{in} = \Gamma(0)\left[1 + \frac{2}{\exp(\hbar w_0/2k_B T) - 1}\right] + \Gamma_{in} \quad . \qquad \textbf{(Eq. 5.2 b)}$$

Fig. 5.5 shows the temperature dependence of the Lorentzian broadening parameter G for the A$_1$-mode of sample (a). The solid line represents the fit of the data points (open dots) which is based on the Klemens model and describes the temperature dependence of the line width of the A$_1$-mode within the investigated temperature range. Although the Klemens model reflects a more simplified approach than, for example, Cowley's approach [37], which considers more phonon decay channels, it is a good approximation for the investigated case.

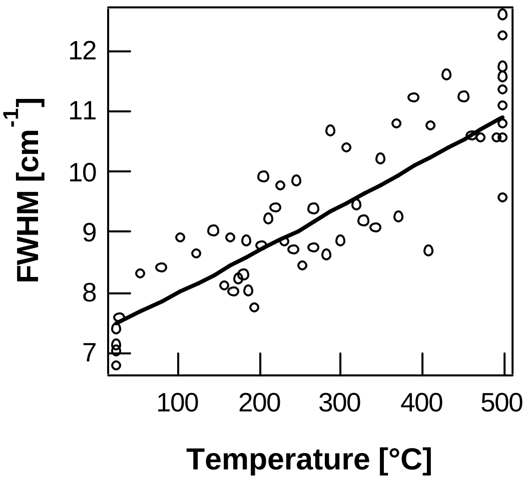

Fig. 5.5: Experimental temperature dependence of the line width G for the A_1-mode of the Cu-rich sample (a). The solid line gives the theoretical fit according to the Klemens model, while the open dots represent the measured data points.

In this section the temperature dependence of the chalcopyrite $CuInS_2$ A_1-mode has been investigated. This is important, as now effects purely caused by the temperature can be separated from the actual phase transitions for the *in-situ* growth experiments of $CuInS_2$ films. A temperature-induced shift of the A_1-phonon mode has been found. This has been explained by the Grüneisen approach and the Grüneisen parameter has been calculated from the experimental data. A reasonable agreement of this value with the Grüneisen parameters of related chalcopyrite materials has been found. Besides a shift as well a broadening and increase in intensity of this Raman line has been found with rising temperature. The temperature-induced broadening has been explained on the basis of a model considering first-order phonon decay.

5.1.2 Role of the Cu/In-Ratio and Na Doping

In the following the temperature dependence of the $CuInS_2$ A_1-mode is investigated for different Cu/In precursor compositions as well as the effect of doping with sodium. It should be mentioned at this point that the presented samples are indeed representative and have been chosen from a large set of investigated samples. **Fig. 5.6** presents the peak positions of the A_1-modes for samples (a), (c), (d), and (e) as a function of the substrate temperature. The peak positions (open dots) are obtained from a single Lorentzian fit as the signals belonging to the CH- and CA-phase are overlapping. Nevertheless, it is incorrect to assume an intermixing of these phases. TEM experiments have proven that the two crystalline phases appear in different domains [77,144].

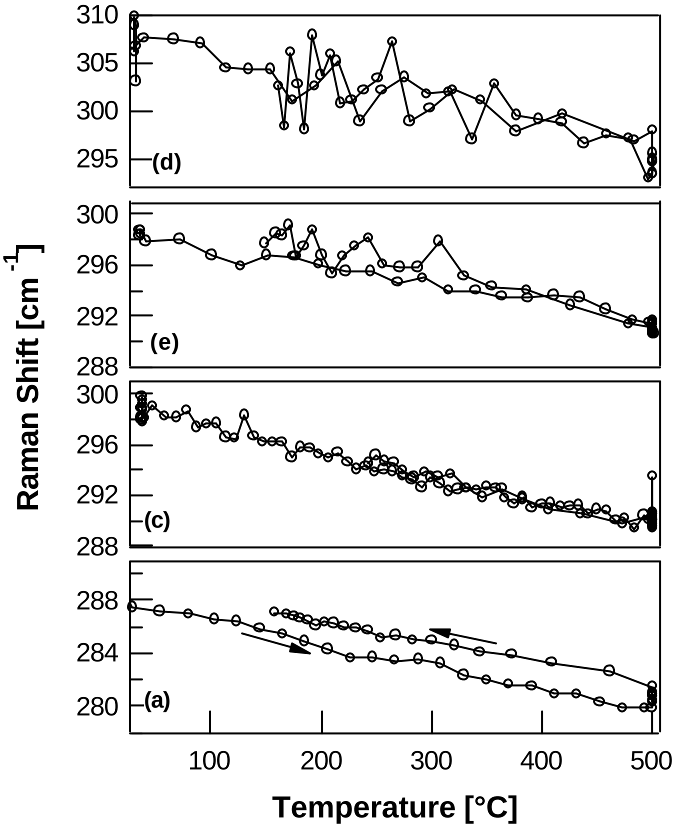

Fig. 5.6: A_1-mode peak position obtained from a single line Lorentzian fit as a function of the substrate temperature for samples (a), (c), (d), and (e). The open dots represent the experimental data, the arrows indicate the heating and cooling period.

The presented temperature-induced peak shifts are shown for the complete annealing process where the heating and cooling periods are indicated by arrows. All samples show a shift of the peak positions towards smaller wave numbers with rising temperature. A linear correlation is most obvious for the Cu-rich sample, while the data of the Cu-poor sample appear with more noise. In **Tab. 5.2** the A_1-mode peak positions at room temperature are given together with the corresponding temperature coefficients.

Tab. 5.2: A_1-mode peak position at room temperature (RT) and temperature-induced peak shift for samples (a), (c), (d), and (e)

Sample	Peak Position at RT [cm^{-1}]	Peak Shift [cm^{-1}/100K]
(a) (Cu/In = 1.8)	290	-1.65
(c) (Cu/In = 1.0)	298	-1.8
(d) (Cu/In = 0.8)	308	-2.4
(e) (Cu/In = 0.8, 30 nm Na)	298	-1.9

The following trends can be stated concerning the peak positions of the A_1-mode for the investigated samples:

- The lower the Cu/In-ratio of the precursor layers, the higher the peak position of the A_1-mode.
- Doping with sodium yields a peak position at significantly smaller wave numbers.

Tab. 5.2 shows that the annealed samples (a), (c), (d), and (e) differ in their absolute A_1-mode peak position if a single line fit is used. The value for the Cu-rich sample (a) (290 cm^{-1}) is in good agreement with the theoretical peak position of the A_1-mode of CH-ordered $CuInS_2$ (294 cm^{-1}). Other groups also found the peak position of the A_1-mode at around 290 cm^{-1} for Cu-rich prepared samples [84,131]. For the Cu-poor $CuInS_2$ layer (sample (d)) without Na the experimental value of 308 cm^{-1} is in good agreement with the peak position of the A_1-mode of CA-ordered $CuInS_2$ at around 305 cm^{-1}. The peak positions for samples (c) and (e) are between the values of the CH- and the CA-phase. Obviously, for these samples the two crystalline phases of $CuInS_2$ coexist. As indicated by the peak positions in **Tab. 5.2** a higher Cu/In-ratio and doping of Cu-poor $CuInS_2$ layers with sodium increase the amount of CH-ordered $CuInS_2$.

The investigated samples do neither show a systematic change of the A_1-peak position at the same temperature in the heating and the cooling period nor a pronounced temperature-induced hysteresis. Thus, no transition between the CH- and the CA-phase of $CuInS_2$ takes place during the annealing. In contrast, such a transition has currently been reported for $CuInS_2$ samples grown at significantly lower temperatures [145].

For samples (c) – (e) higher values of $\partial(\Delta?)/\partial T$ compared to sample (a) have been revealed. The differences in the temperature dependence of the “mixed” A_1-modes are up to 0.75 cm^{-1}/100K. With the above considerations it is likely that this is due to the coexisting CA-phase as the phonon frequencies of this crystalline phase might have a different temperature dependence. Thus, for samples with a Cu/In-ratio of 1.0 or samples which contain Na the experimental shift $\partial(\Delta ?)/\partial T$ can be interpreted by the coexistence of the two phases. Therefore **(Eq. 5.2 b)** cannot be applied to these cases.

The temperature dependence of the line width and of the intensity of samples (c) – (e) has been omitted at this point. However, a larger line width has been revealed for these samples compared to sample (a). This is a further indication for the coexistence of CA-ordered and CH-ordered $CuInS_2$. In consistence with the above results, the comparison of the values of the FWHM at the same temperature in the heating and cooling period do not indicate a phase transition between CH- and CA-ordered $CuInS_2$ for samples (c) – (e).

In summary, the peak positions of the presented samples revealed that the amount of CH- and CA-ordered $CuInS_2$ in the films depend on the type of samples: Cu-rich samples give less CA-phase than Cu-poor films, while Cu-poor films with Na have less CA-phase than those without Na. In order to clarify the mechanism behind, *in-situ* growth experiments have been performed (cf. **chapter 5.3.3**). Slightly higher temperature coefficients have been calculated for films which contain the CA-phase compared to films which are purely CH-ordered. However, the microscopic origin of this difference is unclear. A description of the temperature-induced peak shift and line broadening for CH- and CA- mixed samples with the models presented in **chapter 5.1.1** is not possible and further considerations are needed.

5.1.3 Influence of a CuS Top Layer

Fig. 5.7 shows the annealing process of the as grown Cu-rich sample. The peak positions of the CIS A_1-mode and the CuS modes at 260 and 470 cm^{-1} are plotted versus the temperature. The course of the process is indicated by the arrows. In the heating period both CuS signals disappear at a temperature above 230 °C. At a little higher temperature, the CIS mode appears and remains present up to the end of the process. CuS cannot be detected until in the cooling period the temperature falls below 200 °C. The peak position as well as the temperature-induced peak shift of the CIS A_1-mode determined for this sample agrees with the results for sample (a). Thus, the CuS top layer does not influence the CIS layer.

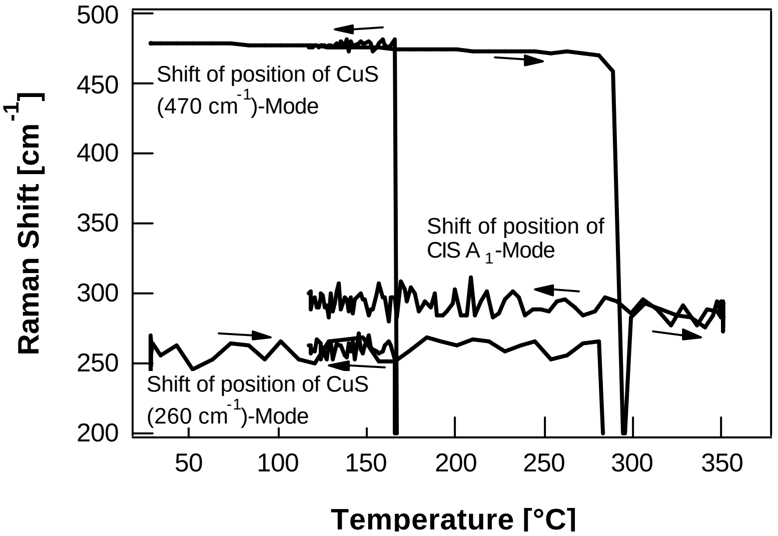

Fig. 5.7: Peak positions of the CIS A_1-mode and CuS modes versus the substrate temperature. The arrows indicate the heating and cooling period.

In **Fig. 5.8** the peak shift, FWHM and intensity of the intense CuS Raman mode at around 470 cm^{-1} is plotted versus the substrate temperature. Here, only the heating period is presented as the peaks in the cooling period occur with more noise, which might be caused by the reformation of this phase. In general a similar behavior as for $CuInS_2$ is observed: with rising temperature a shift of the peak position towards lower wave numbers occurs, while the value of the FWHM increases. In contrast, the intensity decreases. This may be an indication for a continuous transformation of the CuS phase, starting at around 100 °C up to 230 °C. The temperature-induced Raman peak shift of CuS is -3.4 cm^{-1}/100K, which is significantly higher than for $CuInS_2$ (cf. **Tab. 5.2**).

Peiris et al [146] investigated the pressure-induced amorphization of the CuS phase by means of XRD. Based on their results and using **(Eq. 2.24)**, the Grüneisen parameter for CuS can be calculated to $\gamma = 1.4$. The linear expansion coefficients for the a-axis and c-axis of CuS have been determined by means of XRD experiments by Fjellvåg and coworkers [147] to $a_a = 1.2 \cdot 10^{-5}\,K^{-1}$ and $a_c = 1.5 \cdot 10^{-5}\,K^{-1}$. According to the Grüneisen approach, the corresponding temperature-induced peak shift of the CuS frequency can be calculated: -2.54 cm^{-1}/100K (a-axis) and -3.04 cm^{-1}/100K (c-axis).

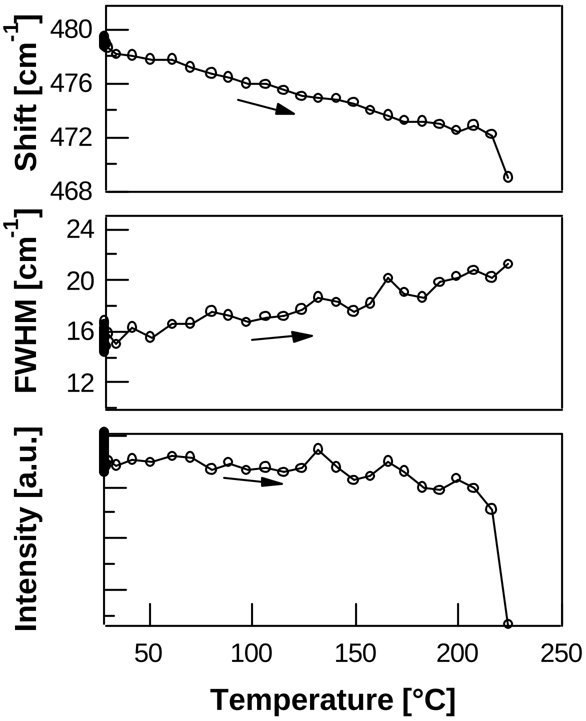

Fig. 5.8: Peak shift, FWHM, and intensity of the CuS Raman mode at 470 cm^{-1} versus the substrate temperature. The open dots are the measured data points and the arrows indicate the heating period.

The calculated value for the temperature-induced peak shift for the c-axis agrees well with the corresponding value determined experimentally within this thesis (-3.4 cm^{-1}/100K). The covellite phase CuS exhibits a hexagonal structure. The crystal structure consists of alternating CuS- and Cu_2S_2-layers, including an S-S bond between two S atoms in the Cu_2S_2-layer [148,149]. The S-S bond is directed along the c-axis. Thus, the observed temperature dependence of the CuS Raman lines may be explained by an increase of the S-S bond length with rising temperature. The Grüneisen approach represents well the temperature-induced peak shift of the intense CuS mode. Therefore it has been omitted at this point to show the fit according to **(Eq. 5.1 a)**. The temperature-induced line broadening is as well represented by Klemens' approach and therefore not shown here.

The annealing of an as grown $CuInS_2$ film reveals that the presence of the CuS top layer does not affect the temperature behavior of the modes related to $CuInS_2$. Furthermore, the CuS phase is not stable for temperatures above 230°C. This point will be investigated in detail when studying the sulfurization of a pure Cu-layer by means of Raman spectroscopy (**chapter 5.2.1**).

5.2 Sulfurization of Pure Cu and In Layers

The Gibbs phase triangle for the Cu-In-S system (cf. **Appendix A.3**) exhibits various Cu-S (cf. **Appendix A.1**) and In-S binary phases (cf. **Appendix A.2**). Tie lines between the binaries and $CuInS_2$ indicate the possible coexistence of $CuInS_2$ with other compounds at thermodynamical equilibrium. It is likely that during the $CuInS_2$ formation binary phases appear. Those phases may show low intense Raman peaks. In order to identify the binary phases which might form during the growth of $CuInS_2$ it is necessary to study their formation by means of Raman spectroscopy. To this end, the sulfurization of a pure Cu and a pure In layer have been investigated by means of *in-situ* Raman spectroscopy under similar conditions as the growth of $CuInS_2$. In the following the sulfurization of Cu and In is presented.

5.2.1 Sulfurization of a Cu Layer

A 500 nm thick Cu layer on glass/Mo has been sulfurized in a vapor beam of elemental sulfur. The following temperature profile has been used: 30 minutes heating to 550 °C, 10 minutes annealing at 550 °C, followed by passive cooling. The working temperature of the sulfur source was 160 °C. The temperature profile is depicted as top graph in **Fig. 5.9 b)**.

In **Fig. 5.9 a)** three characteristic Raman spectra are presented which have been recorded during the sulfurization process at different temperatures. At room temperature no Raman modes have been detected and therefore the corresponding spectrum is not shown here. Spectrum (a) has been recorded in the heating period at a substrate temperature of 200 °C. Three peaks at around 62 cm^{-1}, 260 cm^{-1} and 470 cm^{-1} can be observed. The signals at higher wave numbers are the same as for sample (b) in **Fig. 5.1** and the three Raman bands have been assigned to the CuS phase (covellite). Spectrum (a) is typical for the temperature range from around 160 to 220 °C. Above 220 °C no Raman peaks can be observed (spectrum (b)). In the cooling period the covellite phase can be detected again at a temperature of 200 °C (spectrum (c)) and remains present until the end of the process. The intensities of the Raman bands are smaller in the cooling period compared to the intensities in the heating period. In **Fig. 5.9 b)** the Raman intensities of the single modes are presented as a function of the process time. As the peak intensities can be considered to be representative for the relative amount of a phase, **Fig. 5.9 b)** is an example for the phase predominance sequence diagram derived within this work. Here, no other Cu-S binary phase than the covellite phase could be detected with Raman spectroscopy, although the Cu-S phase diagram [150] also includes Cu-S binary phases such as Cu_7S_4, $Cu_{31}S_{16}$, and $Cu_{2-x}S$.

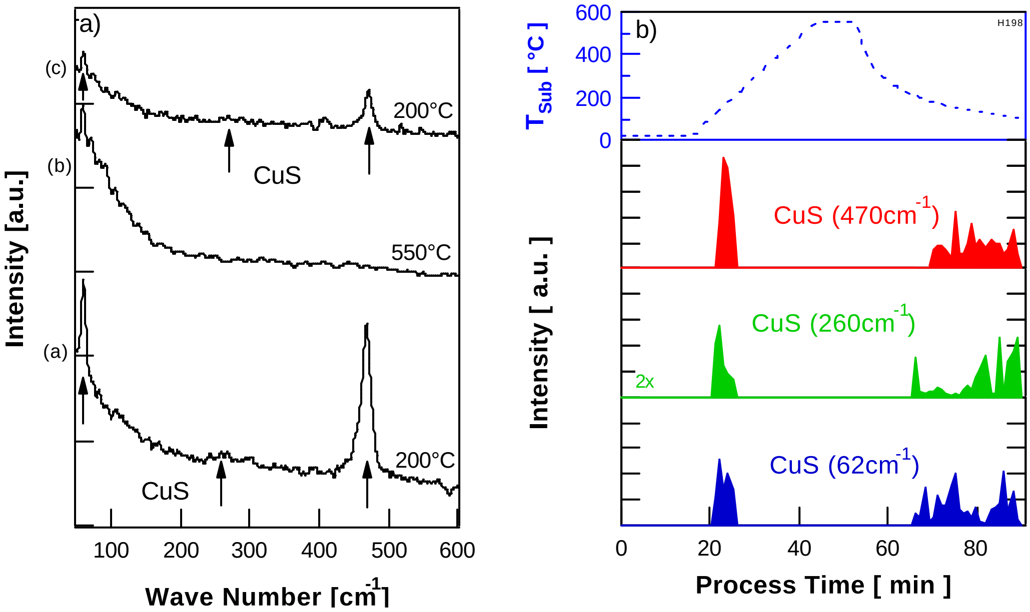

Fig. 5.9: a) Characteristic Raman spectra at different temperatures during the sulfurization of a Cu layer. **b)** Phase predominance sequence diagram of the same process: the intensities of the three CuS peaks at 62, 260 and 470 cm^{-1} are plotted versus the process time, while the substrate temperature is represented by the dashed line at the top of the graph.

XRD *in-situ* studies performed on the sulfurization of pure Cu layers [151] led to the following picture: The anilite phase (Cu_7S_4) forms already at room temperature and at a limited sulfur partial pressure. If the sulfur partial pressure increases, $Cu_{31}S_{16}$ (djurleite) will form additionally. These two phases coexist up to around 70 °C. For higher temperatures they begin to decompose and between 100 and 220 °C the covellite phase (CuS) can be observed. Then, the hexagonal CuS transforms into cubic $Cu_{2-x}S$ (digenite) under the release of liquid sulfur. This transformation occurs reversely during the cooling period at approximately the same temperature.

In consistence with this picture the transformation of covellite is observed at approximately the same temperature at 100 °C with *in-situ* Raman spectroscopy.

This temperature depends on the sulfur partial pressure [152] and is in accordance with thermodynamic calculations. The Cu-rich binary phases djurleite, anilite and digenite can not be observed with Raman spectroscopy. This may be due to their low Raman scattering cross section. However, it is likely that the same transformations occur as found from the XRD-experiments. Obviously, the transformation of CuS into $Cu_{2-x}S$ explains the vanishing of covellite as observed for the annealing experiment (b) in **chapter 5.1.3**. With the findings from **chapter 5.1.3** it can be assumed that the S-S bonds in the covellite phase weaken with rising temperature. As soon as a certain limit, in the present case a temperature of around 220 °C, is reached these bonds dissociate and the digenite phase forms out of covellite.

In summary, for the sulfurization of a pure Cu layer only the CuS-phase can be detected with Raman spectroscopy. This phase forms at a temperature of around 160 °C. In accordance to the previous section CuS is not stable for temperatures above 230 °C. Considering former XRD studies on the sulfurization of pure Cu layers this can be explained by the transformation of CuS into $Cu_{2-x}S$.

5.2.2 Sulfurization of an In Layer

The specimen under investigation was a 500 nm thick In film on glass/Mo. The sulfurization took place in a vapor beam of elemental sulfur. The same temperature profile as for the sulfurization of Cu was used (30 minutes heating to 550 °C, 10 minutes annealing at 550 °C and passive cooling). The working temperature of the sulfur source was 160 °C. The temperature profile is depicted as top graph in **Fig. 5.10 b)**.

A survey of characteristic Raman spectra recorded at different temperatures for the sulfurization of pure In is shown in **Fig. 5.10 a)**. As for the case of the Cu sulfurization no Raman peaks have been detected at room temperature. Spectrum (a) has been recorded in the heating period at a substrate temperature of 200 °C. This spectrum is characteristic for a temperature range between 160 and 270 °C. Peaks can be observed at approximately 140 cm^{-1}, 215 cm^{-1}, 260 cm^{-1}, and 315 cm^{-1}. Above 270 °C (spectrum (b)) the peaks at 140 and 215 cm^{-1} disappear, while a peak at approximately 355 cm^{-1} occurs. These three Raman signals can be detected down to 240 °C in the cooling period. Then, at 240 °C in the cooling period an additional peak occurs at around 175 cm^{-1}. All Raman peaks which are present at 240 °C in the cooling period can be detected until the end of the process, spectrum (c) recorded at 200 °C. For this process the phase predominance sequence diagram of the occurring In-S phases is shown in **Fig. 5.10 b)**.

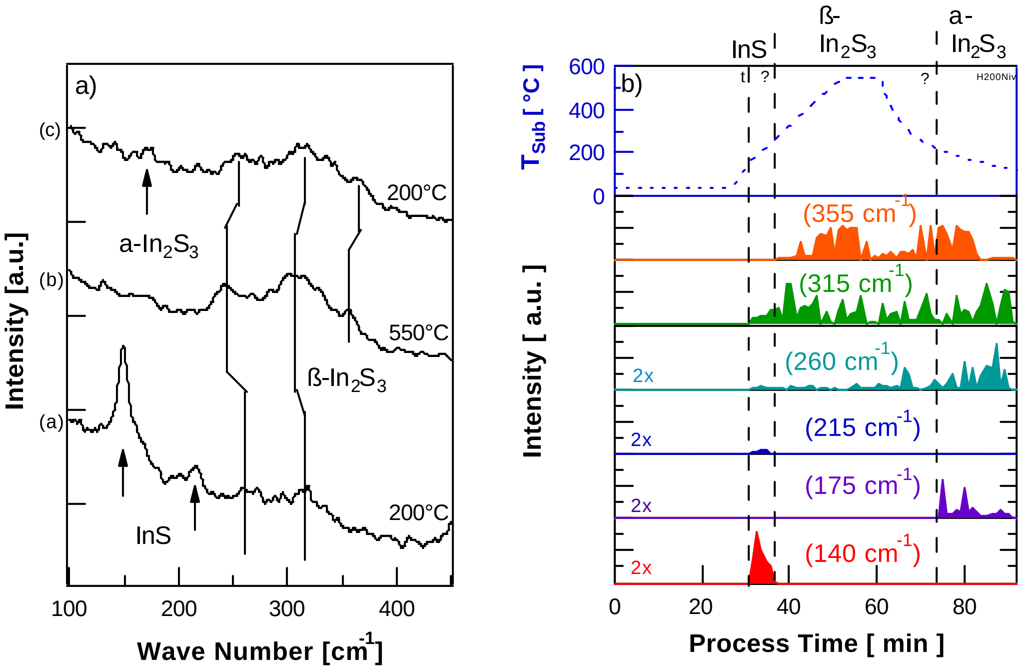

Fig. 5.10: a) Survey of characteristic Raman spectra at different temperatures during the sulfurization of an In layer. **b)** Intensities of the Raman peaks at around 140, 175, 215, 260, 315, and 355 cm^{-1} versus the process time. The substrate temperature is represented by the dashed line at the top of the graph. The Greek letters denote the characteristic transformations, see text for details.

The number of Raman modes reported in the literature on In-S binary phases is rather limited. Only Raman spectra of In_2S_3 phases in the temperature modifications a, ß, and ? are available [81]. However, the phase diagram of the In-S system [153] reveals the existence of orthorhombic a-InS and monoclinic In_6S_7. From XRD studies of the sulfurization of pure In films [151] the following phase transformations have been identified: At around 170 °C cubic In_5S_4 forms, which is a metastable phase. A further increase of the substrate temperature leads to the formation of InS at around 270 °C. Then, at around 410 °C the following transformation can be observed: $16InS + S_8\,(g) \rightarrow 16\,In_2S_3$. This In_2S_3-phase has been identified as the ß-modification, and remains present until 330 °C in the cooling period. At this temperature the transformation of the ß-modification into the a-modification has been observed. For the XRD studies, however, a faster heating ramp (5 minutes up to 550 °C) has been used. Thus, it is expected that for the case of a slower heating (20 minutes up to 550 °C) the phase transformations in the heating period take place at lower temperatures.

The occurrence and vanishing of the different Raman modes at certain temperatures is interpreted as follows: The peaks, which appear at point t in **Fig. 5.10 b)**, could, based on their positions, be assigned to Raman modes related to the low temperature a-In_2S_3 phase. However, in accordance to the XRD-experiment it is more likely to assign the observed Raman bands either to the In_5S_4- or to the InS-phase. At point ? a transformation takes place. At this point two Raman signals vanish and a new peak can be detected. With the help of Ref. [81] the peaks at around 260, 315 and 355 cm^{-1} are assigned to the ß-In_2S_3 phase. Based on this assignment, it is likely to interpret ? as the point of an InS → ß-In_2S_3 transformation. The Raman signals occurring at point t should be related to the InS-phase. Indicated by the appearance of the additional peak at around 175 cm^{-1}, point ? represents the transformation of ß-In_2S_3 into a-In_2S_3. The assignment of these peaks to a-In_2S_3 is in accordance with the findings of Kambas and coworkers [81]. As can be seen in **Fig. 5.10 a)** and **b)** the intense peak at 140 cm^{-1} appears in the heating period, but not in the cooling period. This is a further indication for the assignment of the Raman bands at 140 cm^{-1}, 215 cm^{-1}, 260 cm^{-1}, and 315 cm^{-1} to InS.

The investigation of the sulfurization process of a pure In layer with *in-situ* Raman spectroscopy gives an insight into the transformations of Raman-active phases. Three different In-S binary phases occur which have been identified as InS, ß-In_2S_3, and a-In_2S_3. The InS phase could be assigned with the help of previous performed XRD studies on the sulfurization of pure In layers.

In-situ Raman studies on the sulfurization of Cu- and In-binaries gives insight into possible Raman-active binary phases which may occur as intermediate phases during the growth of $CuInS_2$ films. All Raman modes could be identified, partially with the help of the literature and partially due to the comparison with previous XRD-studies. In addition, the sulfurization of Na/Cu and Na/In stacks has been investigated by means of *in-situ* Raman spectroscopy. For these experiments the same phases have been observed as for the presented experiments. This means that no Na-related phases, such as for example Na_2S or $NaInS_2$, occur during these processes.

5.3 Sulfurization of Cu-In Precursor Layers

In this chapter the results of the *in-situ* growth experiments of Cu-In-S layers are presented. As already mentioned the Cu/In-ratio of the precursor layers is known to influence the performance of $CuInS_2$-based devices: Cu-rich prepared samples yield photovoltaic devices with good performance, in contrast to Cu-poor ones. Cu-poor prepared samples exhibit only good solar cell performance in the case of doping with sodium. Previous performed *in-situ* XRD experiments showed that different phase transformation sequences result for the sulfurization of Cu-rich and Cu-poor precursor layers [154]. Furthermore, the *in-situ* Raman annealing experiments of completed $CuInS_2$ films indicated that the existence of CH- and CA-ordered $CuInS_2$ is influenced by the Cu/In-ratio and doping with sodium. Thus, in order to inspect the mechanisms behind combined XRD- and Raman *in-situ* studies were performed for a Cu-rich (Cu/In = 1.8) precursor layer, a Cu-poor (Cu/In = 0.8) precursor layer, and a Cu-poor (Cu/In = 0.8) precursor layer doped with sodium. Additionally, gradual changes of the growth paths for Cu/In-ratios between 1.8 and 0.8 are elucidated. These experiments will give a more detailed insight into the dependence of the different phases of $CuInS_2$ on the Cu/In-ratios. **Tab. 5.3** gives an overview of the investigated samples.

All films have been sulfurized with a ramp of 27.5 °C per minute from room temperature up to 550 °C, followed by an annealing of 10 minutes at 550 °C and passive cooling. The operation temperature of the sulfur source was around 160 °C and the maximum sulfur partial pressure around $2 \cdot 10^{-2}$ Pa.

Tab. 5.3.: Survey of the investigated samples with their corresponding Cu/In-ratios and Na Contents (given as layer thickness).

Sample	(a)	(b)	(c)	(d)	(e)	(f)	(g)	(h)	(i)	(j)	(k)
Cu/In	1.8	1.6	1.4	1.2	1.2	1.0	1.0	0.9	0.9	0.8	0.8
Na [nm]	0	0	0	0	30	0	30	0	30	0	30

5.3.1 Sulfurization of a Cu-rich Precursor Layer

Characteristic XRD and Raman spectra recorded at different temperatures during the sulfurization of a Cu-rich ($Cu_{1.8}In$) precursor layer are shown in **Fig. 5.12 a)** and **Fig. 5.12 b)**. The spectra reflect the observed phase transitions.

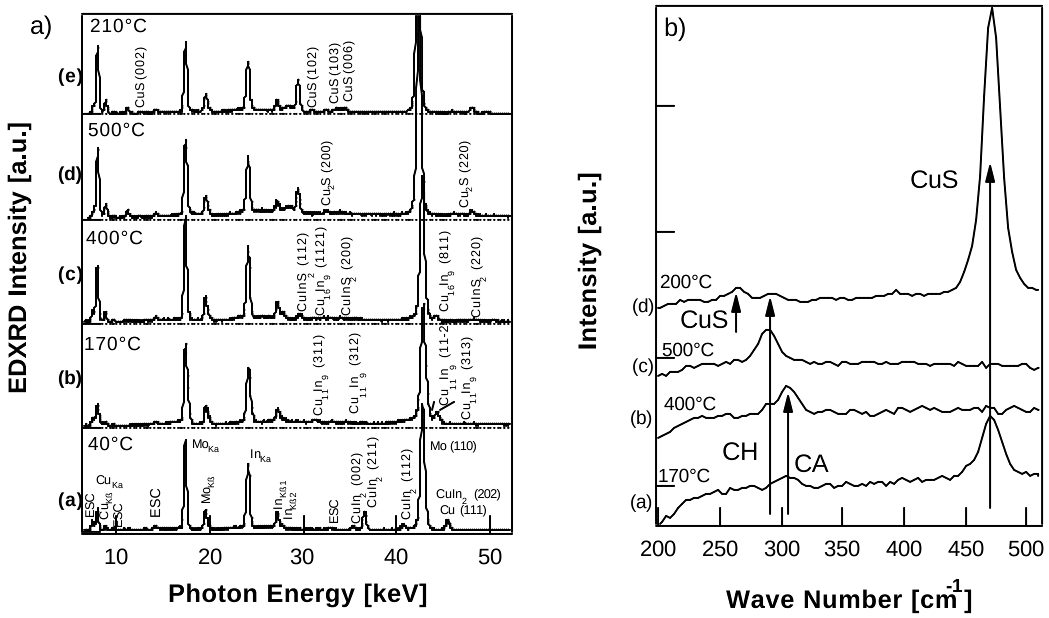

Fig. 5.11: Sulfurization of a Cu-rich ($Cu_{1.8}In$) precursor layer on Mo/glass. Survey of characteristic **a)** XRD and **b)** Raman spectra which have been recorded at different temperatures during the process. Details are given in the text.

In the XRD spectrum (a), recorded at 40 °C, several fluorescence lines of Mo (17 to 20 keV), Cu (8 to 9 keV) and In (24 to 28 keV) can be detected. The spectrum shows a dominant diffraction peak at 42.7 keV which is due to the Mo (110) diffraction. Additionally, diffraction peaks belonging to the phase $CuIn_2$ and one diffraction peak which has been assigned to Cu (111) can be detected. The Cu (111) reflection and the $CuIn_2$ (202) reflection at 45.34 keV are overlapping. Nevertheless, the identification of Cu (111) has been based on the fact that at around 140 °C the $CuIn_2$ (002), (211) and (112) disappear, while the peak at 45.34 keV can still be observed. XRD spectrum (b) – recorded at 170 °C in the heating period - is characteristic for a temperature range between 150 and 230 °C. No signals related to $CuIn_2$ can be detected, while the intensity of the Cu (111) diffraction decreases significantly. However, additional diffraction peaks assigned to the phase $Cu_{11}In_9$ can be observed. At 400 °C (cf. XRD spectrum (c)) peaks related to $Cu_{16}In_9$ occur. The discrimination between $Cu_{11}In_9$ and $Cu_{16}In_9$ was done on basis of the reflections (312) and (11-2) at 34.8 and 43.2 keV, respectively, which do not occur for $Cu_{16}In_9$. Additionally, reflections belonging to $CuInS_2$ can be observed at this temperature. XRD spectrum (d) has been recorded at 500 °C and shows besides the $CuInS_2$ diffraction peaks additional reflections related to a Cu-S compound (Cu_2S). The intensity of the $CuInS_2$ signals at this temperature has significantly increased. At a temperature of 200 °C in the cooling period of the substrate (cf. XRD spectrum (e)), the Cu_2S phase has vanished and reflections related to CuS can be identified. $CuInS_2$ remains present until the end of the process. A survey of all appearing diffraction peaks together with their energetic positions and d-spacings is given in **Tab. 5.4**.

Tab. 5.4: Observed X-ray diffraction peaks, together with the corresponding photon energies and d-spacings.

Diffraction Peak Assignment	Photon Energy [keV]	d-spacing [nm]
$CuIn_2$ (002), (211), (112), (202)	35.4, 36.6, 40.8, 45.3	0.265, 0.257, 0.23, 0.207
Cu (111)	45.5	0.206
$Cu_{11}In_9$ (311), (312), (11-2), (313)	31.3, 35.1, 43.3, 44.3	0.300, 0.268, 0.22, 0.21
$Cu_{16}In_9$ (1121), (811)	31.2, 44.2	0.301, 0.213
$CuInS_2$ (112), (200), (220)	29.6, 34.3, 48.5	0.317, 0.274, 0.194
Cu_2S (200), (220)	32.9, 46.8	0.286, 0.201
CuS (002), (102), (103), (006)	11.5, 30.8, 33.8, 34.3	0.817, 0.305, 0.278, 0.274

The Raman spectra have been taken at approximately the same temperatures as the XRD spectra. The Raman spectrum recorded at room temperature (not shown) exhibits no peaks. Raman spectrum (a) has been recorded at 170 °C. Here, two peaks can be detected at 470 and 305 cm^{-1}, which are related to CuS and CA-ordered $CuInS_2$, respectively. At 400 °C the Raman mode related to the CuS phase has vanished, while the Raman mode related to the CH-ordered $CuInS_2$ (290 cm^{-1}) can be revealed clearly (Raman spectrum (b)). At this temperature the CA- phase appears as the dominating contribution to the $CuInS_2$ signal. In Raman spectrum (c) at around 500 °C the CA signal has almost vanished, whereas the intensity of the CH-ordered $CuInS_2$ peak has increased. In the cooling period at around 210 °C two signals belonging to CuS at 260 and 470 cm^{-1} can be observed. Although exhibiting a smaller intensity, the CH-ordered phase can be observed until the end of the process (cf. Raman spectrum (d)).

In **Fig. 5.12** the results of the *in-situ* investigations of the Cu-rich experiments are summarized in form of phase predominance sequence diagrams. These plots give the intensity of the XRD-peaks normalized to the Mo_{Ka} fluorescence line as well as the intensity of the Raman lines as a function of the process time. The substrate temperature profile is plotted in the header of this figure. The $CuInS_2$ Raman signals are fitted using two Lorentzians by splitting the signal up into the CH- and CA- phase.

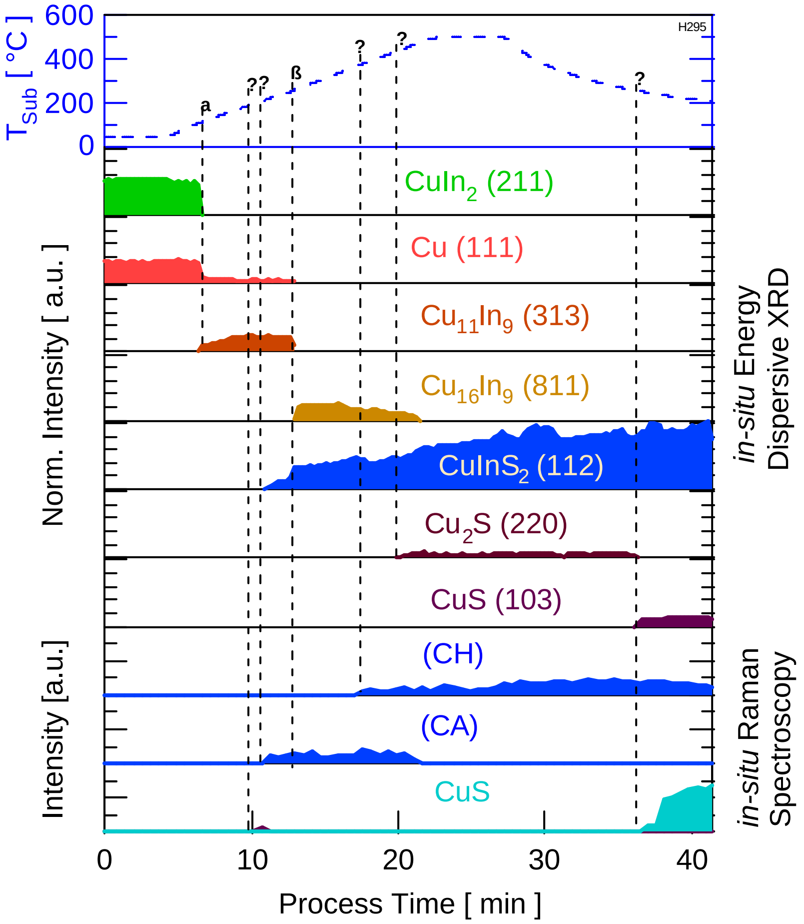

Fig. 5.12: Temperature profile and determined intensities of selected XRD reflections and Raman modes as a function of the process time. For sake of clarity the XRD intensity plots have a yellow and the Raman plots a light purple background. The XRD intensities are normalized to the Mo_{Ka} fluorescence. The Greek letters indicate the phase transitions. For details see text.

For the $Cu_{1.8}In$ precursor the starting metallic phases are $CuIn_2$ and Cu. $CuIn_2$ has already formed at room temperature due to storage of the CuIn precursor for more than 24 h and can be detected up to 140 °C (point a). At this point $CuIn_2$ transforms into $Cu_{11}In_9$ under the release of In. Further heating of the substrate (a ? ?) induces a decrease of the Cu (111) intensity, while the intensity of the $Cu_{11}In_9$ peak is increasing. The decrease of the Cu (111) reflection can be explained with the diffusion of In along the $Cu_{11}In_9$ grain boundaries into the Cu layer. Only by means of

Raman spectroscopy peaks related to CuS can be detected during the heating period at around 165 °C (?). As this phase is not visible in the XRD spectra, it is likely, that CuS forms near the surface with a relatively small volume percentage. At slightly higher temperatures at around 175 °C, indicated by the point ? in **Fig. 5.12**, the formation of $CuInS_2$ can be observed. The Raman data reveal that the $CuInS_2$ formation starts with the CA-phase only. Currently it is assumed that $CuInS_2$ initially forms from the intermetallic $Cu_{11}In_9$-phase and elemental sulfur. This reaction path implies the formation of CuS and the following reaction is proposed:

$$Cu_{11}In_9 + 20S \; ? \; 9CuInS_2 + 2CuS.$$

S_8-rings provided from the vapor are assumed to dissociate when reacting with the sample surface. CuS may alternatively be formed from the elemental Cu in case the latter is not completely covered by $Cu_{11}In_9$. However, the XRD experiments of pure Cu layers give rise to a reaction of Cu with sulfur to Cu_7S_4 already at room temperature, see **chapter 5.2.1**. This phase could not be detected in the presented sulfurization experiment, and therefore it is likely, that the Cu layer is completely covered and the reaction mentioned above takes place. It has been shown in **chapter 5.2.1** that CuS is not stable for temperatures above 220 °C. Two possible reactions can be considered to explain the vanishing of CuS. Based on the XRD results of pure Cu sulfurization the hexagonal CuS may transform into cubic Cu_2S above 220 °C. Due to the XRD signal overlap between Cu_2S and $CuInS_2$ the Cu_2S phase is difficult to detect in small quantities. As the amount of the CuS phase is rather small and so is the amount of Cu_2S, the latter might have too small volume percentage to be detectable with XRD. Alternatively, CuS may react with the released liquid In and the sulfur from the gas phase to $CuInS_2$. As both reactions are likely to take place, it is not possible to rule out one of the reactions.

Passing point ? up to point ß the intensity of the peaks belonging to $Cu_{11}In_9$ as well as the Cu (111) diffraction peak slightly decrease. As soon as a substrate temperature of around 260 °C (ß) is reached, $Cu_{11}In_9$ transforms into $Cu_{16}In_9$. A further rise of the temperature is accompanied by decreasing $Cu_{16}In_9$ signals and increasing $CuInS_2$ signals. Obviously, $Cu_{16}In_9$ serves as source for the $CuInS_2$ formation. At point ?, which corresponds to around 400 °C, the Raman data reveal that the formation of CH-ordered $CuInS_2$ starts. From approximately 460 °C on (point ?) Cu_2S can be detected. $CuInS_2$ and Cu_2S are formed out of the intermetallic phase

$Cu_{16}In_9$ and from the elemental sulfur until $Cu_{16}In_9$ is completely consumed. This takes place at around 500 °C. The vanishing of the CA-phase coincides with the end of the heating period. Due to the excess of Cu in this experiment the Cu_2S phase remains present up to point ? in the cooling period at around 220 °C. At this point, the transformation $Cu_2S + S$? CuS takes place. As already reported by several authors e.g. [156] the final layer only consists of two phases: CuS and CH-ordered $CuInS_2$. The Raman data confirm that the CuS phase is located on top of $CuInS_2$ and forms an almost complete coverage.

The experimental results clearly reveal that CA-ordered $CuInS_2$ forms first. The existence of the two different phases of $CuInS_2$ will be discussed later with respect to the different Cu/In-ratios.

5.3.2 Sulfurization of a Cu-poor Precursor Layer

To elucidate the sulfurization of a Cu-poor layer, a $Cu_{0.8}In$ precursor layer has been chosen. In **Fig. 5.13 a)** and **Fig. 5.13 b)** XRD and Raman spectra of this process recorded at different temperatures are shown. In the following only the differences between the sulfurization of a $Cu_{1.8}In$ and $Cu_{0.8}In$ precursor layer will be pointed out.

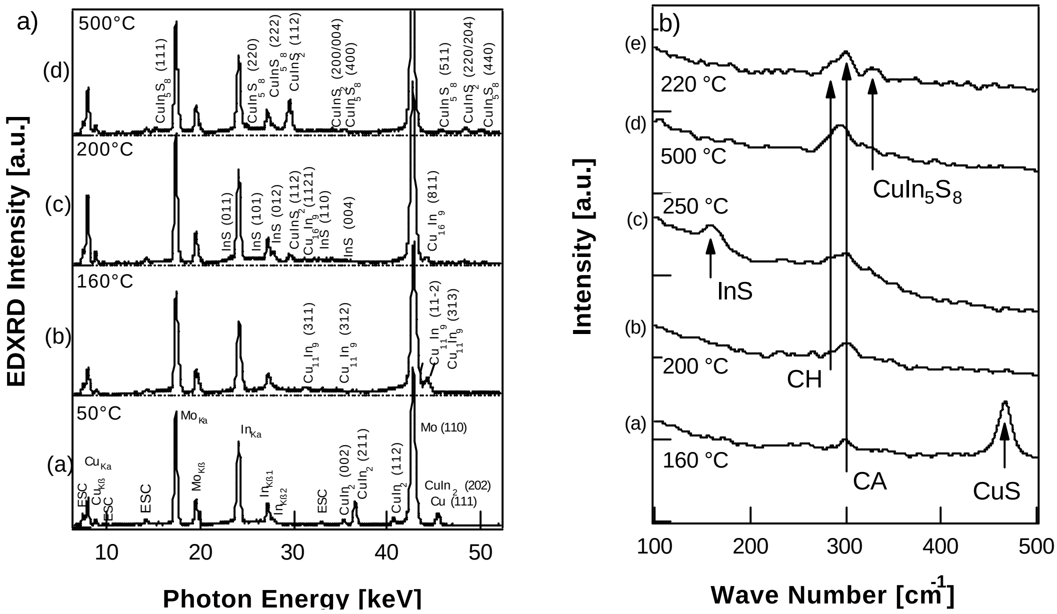

Fig. 5.13: Sulfurization of $Cu_{0.8}In$/Mo/glass. Selection of characteristic **a)** XRD and **b)** Raman spectra recorded at different temperatures during the process. For details see text.

It is visible in **Fig. 5.13 a)** that the same fluorescence lines as for the Cu-rich experiment occur as well as most of the diffraction lines. The main differences in the phase transformation sequence are the occurrence of XRD signals related to InS in spectrum (c) and $CuIn_5S_8$ in (d) and (e). No signals related to Cu_2S can be observed. The diffraction peaks of the additional phases InS and $CuIn_5S_8$ together with their photon energies and d-spacings are listed in **Tab. 5.5**.

Tab. 5.5: Observed XRD diffraction peaks of InS and $CuIn_5S_8$, their corresponding photon energies, and d-spacings.

Diffraction Peak Assignment	Photon Energy [keV]	d-spacing [nm]
$CuIn_5S_8$ (111), (220), (400), (511), (440)	15.3, 25.0, 35.4, 50.1	0.614, 0.376, 0.265, 0.188
InS (011), (101), (012), (110), (004)	23.4, 25.5, 27.9, 32.3, 35.6	0.402, 0.368, 0.337, 0.291,0.264

The Raman spectrum at room temperature does not reveal any phases and is not shown here. The Raman spectra in **Fig. 5.13 b)** show that the following modes differ from those in the Cu-rich experiment: at around 280 °C an additional mode at 140 cm^{-1} can be detected, which has been assigned to InS. For T > 360 °C a broad peak at 350 cm^{-1} is visible in spectra (c) and (d), which belongs to the $CuIn_5S_8$ phase. **Fig. 5.14** gives the normalized intensities of the XRD reflections and the intensity of several Raman lines as a function of the process time for the Cu-poor sulfurization. For reference purposes, the substrate temperature profile is plotted in the header of this figure. At room temperature we find $CuIn_2$ and Cu like in the Cu-rich experiment. Both phases are stable up to around 120 °C in the heating period. At this point (a) $Cu_{11}In_9$ is formed with the complete consumption of $CuIn_2$ and Cu. At around 170 °C the formation of CuS starts (?). CA-ordered $CuInS_2$ initially forms at point ? (around 190 °C). Shortly after the $CuInS_2$ formation, CuS vanishes. It is likely to assume that the CuS phase forms together with $CuInS_2$ out of $Cu_{11}In_9$ as in the Cu-rich experiment. Here, the formation of CuS from elemental Cu and sulfur can be excluded, as no abundant Cu is available to react.

At around 230 °C the transformation $Cu_{11}In_9$? $Cu_{16}In_9$ takes place (point ß) under release of liquid In. The intensity of the $CuInS_2$ (112) reflection increases, while the intensity of the $Cu_{16}In_9$ reflection decreases. This indicates the formation of $CuInS_2$ out of the intermetallic $Cu_{16}In_9$ phase. At a temperature of around 250 °C (point t) signals related to InS can be observed. Obviously, the formation of $CuInS_2$ consumes all Cu leaving no excess Cu for the In to react. Thus, at point t the released liquid In sulfurizes at the sample surface. The Raman peak at 140 cm^{-1} occurs at approximately the same temperature as the InS phase in the XRD spectra. This is a further indication to assign this Raman peak to InS. At 320 °C (point ?) the Raman mode related to InS disappears, while the diffraction lines belonging to InS can still be observed up to 360 °C. Additionally at point e, both the Raman and the XRD signals related to $CuIn_5S_8$ occur. Thus, the InS phase might be covered by the forming $CuIn_5S_8$ spinel phase. It is currently assumed [151] that at this point the spinel phase as well as $CuInS_2$, is formed out of the intermetallic $Cu_{16}In_9$ and InS, which is indicated by the further increase of the $CuInS_2$ signals. The CH-ordered $CuInS_2$ can be detected for temperatures above 400 °C (point ?). At 450 °C a decrease in intensity of the $CuIn_5S_8$ diffraction line can be stated, which might be due to Cu atoms diffusing into $CuIn_5S_8$ and its transformation into $CuInS_2$. At approximately the same temperature $Cu_{16}In_9$ vanishes. At a temperature of 550 °C the intensity of the $CuInS_2$ (112) reflection remains approximately constant until the end of the process. This indicates the end of the $CuInS_2$ formation. Up to the end of the process the $CuIn_5S_8$ phase and both CA- and CH-ordered $CuInS_2$ can be observed.

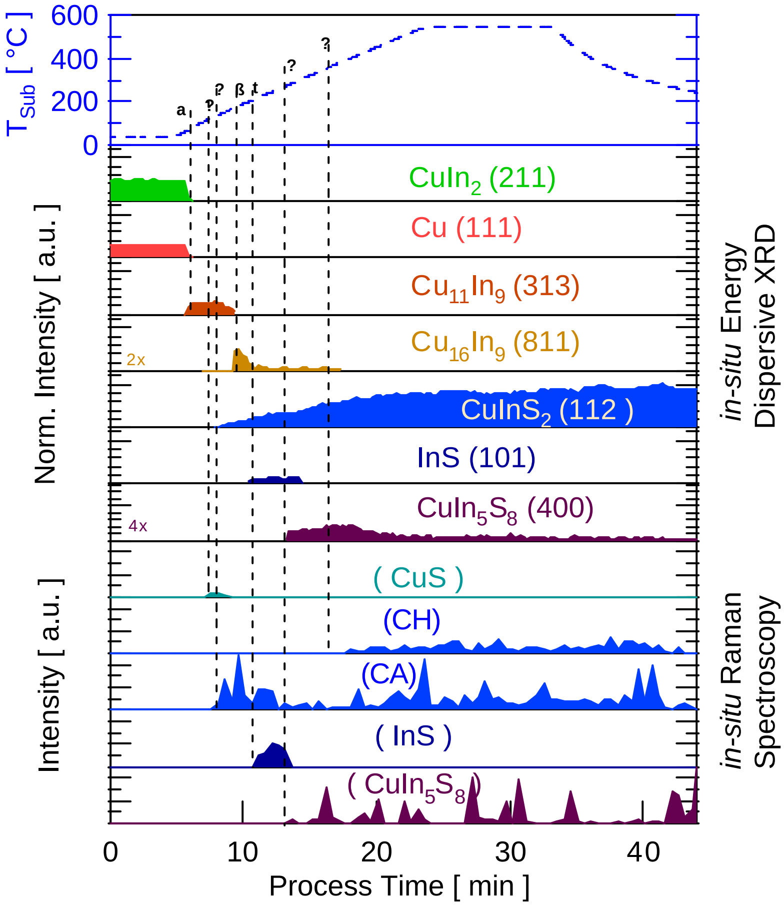

Fig. 5.14: Temperature profile and peak intensities of selected XRD reflections and Raman modes as a function of the process time for the sulfurization of a Cu-poor ($Cu_{0.8}In$) precursor. The Greek letters indicate the phase transitions. See text for details.

Thus, the main differences to the sulfurization of a $Cu_{1.8}In$ precursor layer are the occurrence of an additional InS phase in the heating period, the presence of CA-ordered $CuInS_2$ up to the end of the process and the spinel phase $CuIn_5S_8$, which forms in the heating period and remains present until the end of the process. Moreover, no Cu-S compounds can be identified.

5.3.3 Sulfurization of a Cu-poor Precursor Layer Containing Sodium

In order to study the influence of sodium on the sulfurization of Cu-poor precursor layers, a $Cu_{0.8}In$ precursor layer with 30 nm NaF has been studied. XRD and Raman spectra recorded at different temperatures during the process are shown in **Fig. 5.15 a)** and **Fig. 5.15 b)**, respectively. The XRD spectra, generally, exhibit the same diffraction lines compared to the sulfurization of a $Cu_{0.8}In$ precursor layer without sodium. Only a lack of the InS phase must be considered. Thus, no additional diffraction lines, e.g. related to any Na-containing phase, appear for this process.

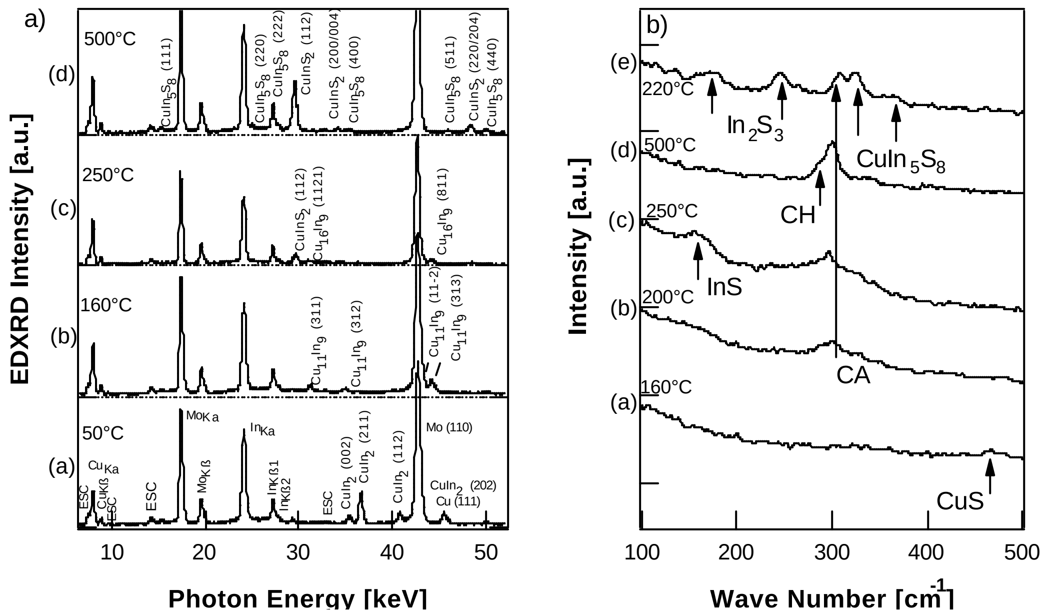

Fig. 5.15: Sulfurization of $Cu_{0.8}In$/NaF/Mo/glass. Selection of characteristic **a)** XRD and **b)** Raman spectra recorded at different temperatures during the process.

The Raman spectra show the following difference to the undoped Cu-poor sample: In the cooling period at around 230 °C an additional phase β-In_2S_3 can be detected. As for the XRD-spectra, no mode related to a Na-compound is observable.

Fig. 5.16 gives the phase predominance sequence diagram for the sulfurization of a $Cu_{0.8}In$ precursor layer with sodium. Up to point t, the same phase sequence can be observed as in samples without sodium. At this point, which corresponds to a temperature of 250 °C, a Raman line related to InS can be observed, while no XRD-signals belonging to this phase have been detected. Thus, this phase is assumed to form near the surface with a relatively small volume percentage. Point ? (at around 340 °C) marks the vanishing of the InS binary phase, accompanied by the formation of the spinel phase $CuIn_5S_8$. A possible explanation is that the sodium in the precursor leads to the formation of a Na-In-S compound. The volume percentage of this compound might be so small that it is below the detection limit. In this case, a Na-In-S compound can serve as a storage for the excess In and prevent the sulfurization of In. The formation of Na-In-Se compounds, such as $NaInSe_2$, has already been proposed for the selenization of CuIn layers doped with sodium [157].

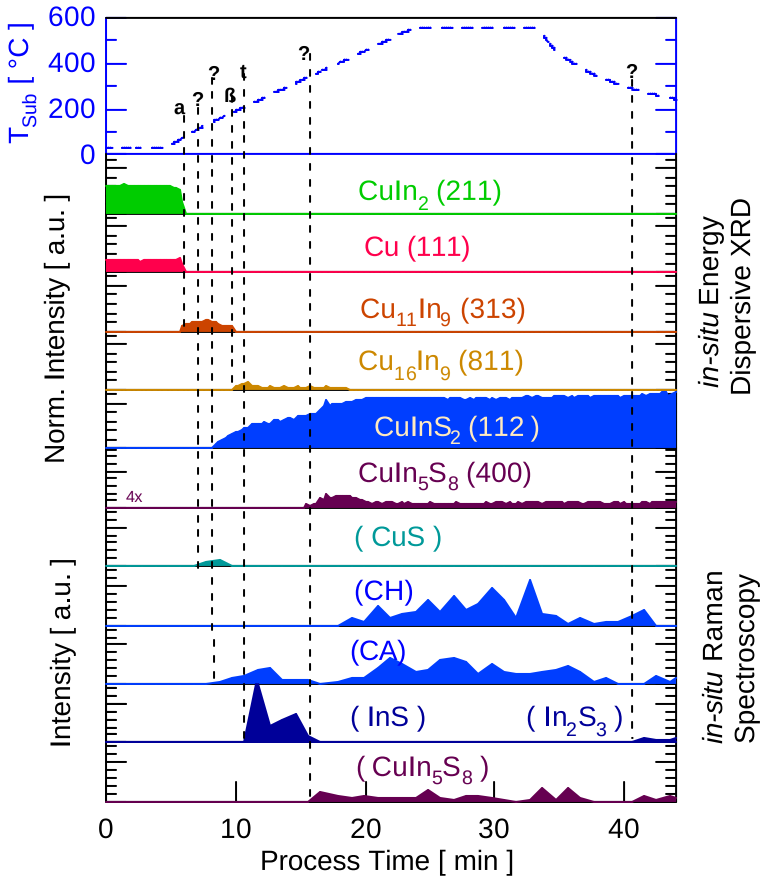

Fig. 5.16: Temperature profile and peak intensities of selected XRD reflections and Raman modes as a function of the process time for the sulfurization of a Cu_xIn/NaF/Mo/glass sample (x = 0.8). The Greek letters denote the phase transitions. For details see text.

Passing point ?, the further course of this process is similar to the process of the Cu-poor precursor layer without sodium. Only in the cooling period at around 230 °C (point ?) the additional formation of β-In_2S_3 can be observed by means of Raman spectroscopy. Assuming the presence of a Na-In-S compound, then β-In_2S_3 might form if Na evaporates from the surface. However, this subject requires further investigation. The final film consists of CA- and CH-ordered $CuInS_2$, $CuIn_5S_8$, and β-In_2S_3. The Raman intensities indicate a smaller amount of $CuIn_5S_8$ compared to the Cu-poor experiment without sodium. Thus, sodium in the form of Na-In-S might act as storage for the excess In. It is remarkable, that the investigated sample exhibits a higher amount of CH-ordered $CuInS_2$, compared to the case without sodium.

The *in-situ* growth experiments of a Cu-rich, a Cu-poor and a Cu-poor sample doped with sodium reveal different phase transformation sequences. For the sulfurization of a $Cu_{1.8}In$ precursor layer the excess Cu is stored in a CuS phase, while an InS phase due to the excess In occurs for a $Cu_{0.8}In$ layer. This InS phase further forms to the spinel phase $CuIn_5S_8$, which remains present up to the end of the process. The incorporation of sodium in Cu-poor films leads to smaller amounts of $CuIn_5S_8$ in the surface-near region and gives rise to an additional β-In_2S_3 phase in the cooling period of the process. It is remarkable, that the $CuInS_2$ formation starts for all the samples with the CA-phase. However, the amount of CA-ordered $CuInS_2$ at the end of the process is the highest for the undoped Cu-poor samples, while for the Cu-rich sample no CA-phase is observed. In order to detail this point, a systematic study for samples with a varying Cu/In-ratio is presented in the following.

5.3.4 CA- and CH-Phases in $CuInS_2$

The *in-situ* growth experiments revealed that different crystallographic phases occur depending on the stoichiometry of the precursor layers and additionally supplied sodium. Also the occurrence of different phases of $CuInS_2$ is influenced by these factors. As Raman spectroscopy allows the detection of these phases of $CuInS_2$, additional *in-situ* Raman growth experiments will detail these points. In the following the temporal development of the two phases of $CuInS_2$ during the sulfurization are studied for samples (a) - (k) (cf. **Tab. 5.3**). As the dominant Raman modes of CH- and CA-ordered $CuInS_2$ overlap, the Raman signal at around 300 cm^{-1} is interpreted as a combination of these two contributions and a single Lorentzian fit has been used. Then, the different phases can be visualized as the shift of the combined peak. In order to reveal this shift as an outcome of a phase transition, temperature-induced peak shifts have to be removed. To this end, the peak positions have been corrected by the linear temperature dependence of the corresponding annealing experiments from **Fig. 5.6**.

Fig. 5.17 shows the Raman A_1-mode positions of $CuInS_2$ versus the process temperature for the sulfurization of the precursors (a), (f), (j), and (k). The samples have been chosen to cover the range of different Cu/In-ratios and to reflect also the case of sodium doping. The course of the growth process is indicated by the arrows. The temperature of the initial formation of $CuInS_2$ can be judged from the first appearance of the corresponding Raman mode. In the Cu-rich experiment (a) the $CuInS_2$ formation starts at approximately 175 °C, and the Raman peak is located at around 305 cm^{-1}. At temperatures exceeding 400 °C a decrease of the Raman line position down to around 292 cm^{-1} can be observed. During the annealing and the cooling period no further change has been observed.

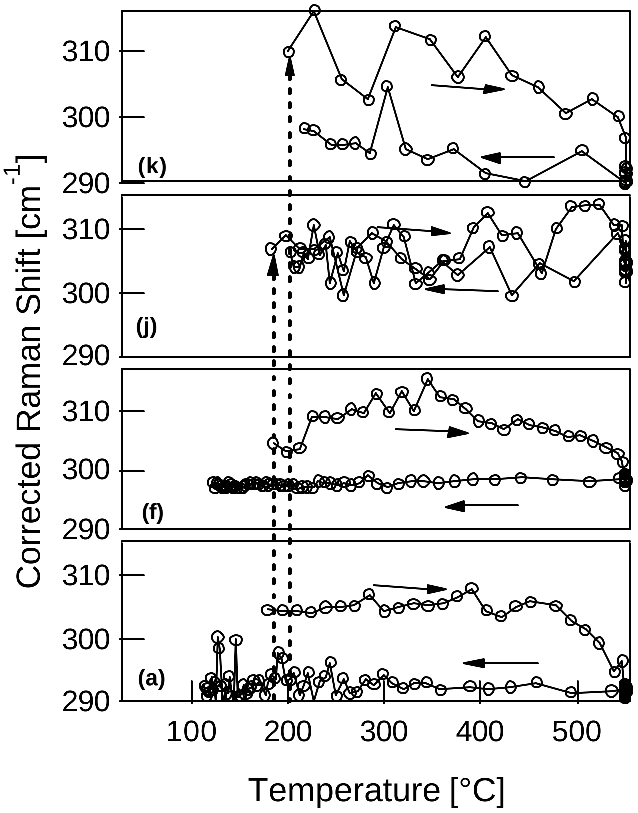

Fig. 5.17: Growth experiments for samples (a) Cu-rich ($Cu_{1.8}In$), (f) ($Cu_{1.0}In$), (j) Cu-poor ($Cu_{0.8}In$), and (k) Cu-poor ($Cu_{0.8}In$) with Na are presented as the peak shift of the $CuInS_2$ Raman A_1-mode versus the temperature. The peak position of this mode obtained from a single Lorentzian fit is given as a function of the substrate temperature. The peak shift has been corrected by the temperature dependence as revealed in the annealing experiments. The arrows indicate the process sequence.

For sample (f), which represents a $Cu_{1.0}In$ precursor, a similar behavior has been found. At around 175 °C the $CuInS_2$ formation starts with an A_1-mode peak position at around 305 cm^{-1}. From around 400 °C on, the peak position shifts to 297 cm^{-1}. As soon as a temperature of 550 °C has been reached, no further shift can be observed. For the Cu-poor experiment without Na, sample (j), the position of the $CuInS_2$ mode starting from its first appearance at around 180 °C remains at 308 cm^{-1} for both, the heating and the cooling period. For the $Cu_{0.8}In$:Na sample the behavior is similar to the behavior of samples (a) and (f): The $CuInS_2$ mode can be detected at a peak position of around 310 cm^{-1}. For temperatures higher than 400 °C a decline down to around 295 cm^{-1} occurs. While during the annealing period the mode does not shift significantly, a slight increase of the line position can be stated during the cooling period. The peak position of sample (k) at the end of the process is at around 297 cm^{-1}. For samples doped with sodium the initial formation of $CuInS_2$ is detected at around 200 °C, which is higher than for the cases without Na.

In order to summarize these findings the peak positions of the $CuInS_2$ Raman mode of the final Raman spectra, the corresponding Cu/In and the Na content are listed for all investigated samples in **Tab. 5.6**.

Tab. 5.6: Raman peak position obtained from a single Lorentzian fit for samples with different Cu/In precursor ratios and Na content.

Sample	(a)	(b)	(c)	(d)	(e)	(f)	(g)	(h)	(i)	(j)	(k)
Cu/In	1.8	1.6	1.4	1.2	1.2	1.0	1.0	0.9	0.9	0.8	0.8
Na [nm]	0	0	0	0	30	0	30	0	30	0	30
A_1-Peak Position [cm^{-1}]	292	293	293	296	296	297	296	302	298	308	298

In brief, for the sulfurization of Cu_xIn ($x > 1.2$) precursors the formation of the CH-ordered $CuInS_2$ starts at around 400 °C and no CA-ordered $CuInS_2$ can be detected any more when the peak of highest temperature is reached. The sulfurization of Cu_xIn ($1.2 = x = 1.0$) precursors and Cu_xIn ($x = 1$) precursors with Na also show a clear change from the CA-phase to the CH-phase. However, as indicated by the peak positions for these cases, CA-ordered $CuInS_2$ can be observed until the end of the process. Thus, the CH- and CA-phases are found to coexist. For the Cu-poor experiments without sodium the $CuInS_2$ signals are clearly dominated by the CA-phase during the entire process.

The intensity ratios CA/CH, $CuIn_5S_8$/CH, and CuS/CH determined from Raman spectra at the end of the process are plotted versus the different Cu/In precursor ratios in **Fig. 5.18 a)**, **b)**, and **c)**. The gray markers give the results for the samples containing sodium. It can be seen in **Fig. 5.18 a)** that for the undoped sample with $Cu_{0.8}In$ the CA-phase appears as the dominating contribution to the $CuInS_2$ signal, while an increase of Cu/In is combined with a gradual reduction of the CuAu signal. Finally, for Cu_xIn samples with x > 1.2 no CA-ordered $CuInS_2$ can be detected. $CuIn_5S_8$ can be identified for samples with x < 1.2, while for x = 1.2 no such signals occur (cf. **Fig. 5.18 b)**). **Fig. 5.18 c)** shows that for samples with x > 1.2 CuS is the dominating signal at the end of the sulfurization. As expected from the precursor composition, the intensity of CuS is increasing with an increasing amount of Cu in the precursor. For x < 1 no CuS appears in the final spectrum. From these plots it can be concluded that the phase transformation sequence of precursor layers with Cu_xIn (0.8 < x < 1.8) is between the two end cases $Cu_{1.8}In$ and $Cu_{0.8}In$.

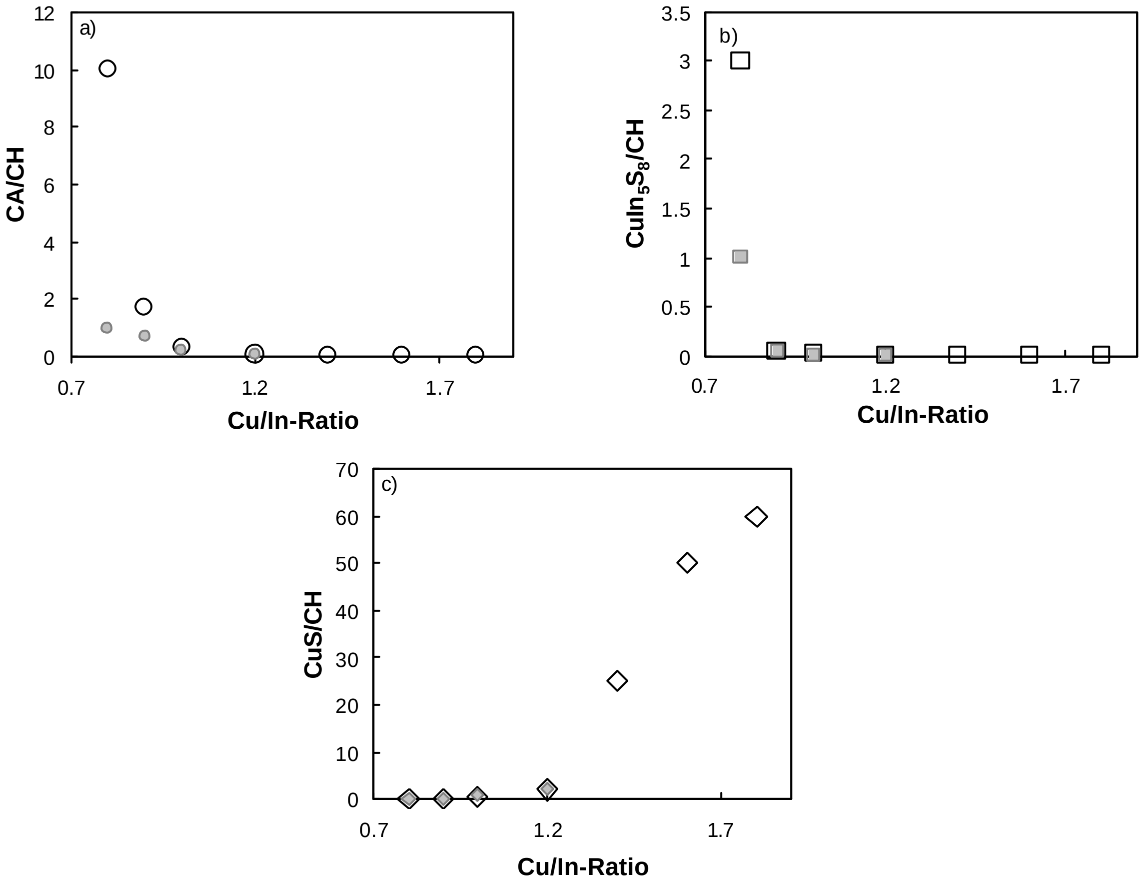

Fig. 5.18: Relative intensity ratios of **a)** CA-ordered $CuInS_2$, **b)** $CuIn_5S_8$ and **c)** CuS as a function of the Cu/In-ratio. The gray markers represent the samples containing sodium.

While the stoichiometric case (Cu_xIn, x = 1) is closer to the findings of the Cu-poor experiment, the sulfurization of Cu_xIn precursors with x > 1 resembles the reaction path of the $Cu_{1.8}In$ experiment. Depending on the Cu or In excess the amounts of the binary phases differ.

The introduction of sodium in the films has an influence on the peaks related to $CuIn_5S_8$ and CH-ordered $CuInS_2$: For x = 1.0 the peaks related to $CuIn_5S_8$ appear less intense, while the modes of the CH-phase are higher intense - compared to undoped samples. However, for x > 1.2 sodium does not appear to influence the Raman spectrum of the film.

The influence of the Cu/In-ratio as well as of doping with sodium on the presence of the different phases of $CuInS_2$ can be summarized with the following trends:

- The smaller the amount of Cu-S compounds during the process, the more CA-ordered $CuInS_2$ can be detected at the end of the process.
- The higher the amount of In-S compounds in the heating period, which directly results into higher amounts of $CuIn_5S_8$, the higher the contribution of the CA-phase to the $CuInS_2$ signal.
- The introduction of sodium in Cu_xIn with x = 1.0 precursors supports the formation of CH-ordered $CuInS_2$.

All growth experiments have in common that the $CuInS_2$ formation starts with the CA-phase, while CH-ordered $CuInS_2$ forms primarily at around 400 °C. The $CuInS_2$ formation proceeds at the very surface, this means that the growth front is in direction of the surface normal [120]. It may be argued at this point that initially formed CA-ordered $CuInS_2$ at the end of the growth is covered by newly grown CH-ordered $CuInS_2$. In order to assess the thickness of the newly grown $CuInS_2$ layer, it is necessary to have a look at the growth mechanism. It has been explained in **chapter 5.3.1** that the $CuInS_2$ formation proceeds out of $Cu_{16}In_9$. Even a linear relationship between the consumption of $Cu_{16}In_9$ and the formation of $CuInS_2$ has been found [151]. At 400 °C, when the CH-phase forms, about 75 % of $Cu_{16}In_9$ is already consumed by this reaction. Thus, around 400 nm $CuInS_2$ will be formed up to the end of the process. Therefore the primarily formed CA-phase will indeed be covered by newly grown $CuInS_2$. Based on the surface sensitive *in-situ* Raman experiments it is impossible to measure a transformation between CA- and the CH-ordered $CuInS_2$ within the bulk of the film. However, from Raman depth-dependent experiments of finished layers it is known that for the Cu-rich case no CA-phase is left at all [131]. Therefore the results can be interpreted in the sense of a transformation between the two phases.

The formation of CH-ordered $CuInS_2$ is energetically favored compared to CA-ordered $CuInS_2$. However, the difference in formation energy between these two phases is small (-7.8 meV/4 atoms) [11]. The presented results point out that the formation of the metastable CA-phase is favored at low temperatures. At this point the following questions arise: (1) Which mechanism promotes the CA-phase to form at lower temperatures, respectively the CH-phase not to form below 400 °C? (2) How can the Cu/In-ratio influence the formation of CH-ordered $CuInS_2$?

In order to explain the effect of temperature on the growth of the different $CuInS_2$ phases the following approach is possible. It has been theoretically shown for III-V semiconductor alloys that cation orderings, which generally are thermodynamically less stable, can occur due to lowest energy reconstruction of the surface [79]. As the $CuInS_2$ formation proceeds at the very surface, similar effects might promote an energetic minimum for the formation of CA-ordered $CuInS_2$ at lower growth temperatures. However, lower growth temperatures are inevitably combined with a higher number of defects in the film. Thus, the formation of CA-ordered $CuInS_2$ may be associated with the number of defects in the growing film. The presence of defect states might lead to an environment that enables the metastable CA-phase to be energetically favored. Accordingly, the formation of CH-ordered $CuInS_2$ requires a smaller grade of disorder, which means fewer defects.

The most obvious effect of different Cu/In-ratios on the growth of $CuInS_2$ is that the binary phases occur in different amounts. The incorporation of sulfur from the gas phase in the crystal is kinetically limited due to its high vapor pressure within the used temperature range [158]. However, Klenk [159] showed that if the chalcopyrite thin film growth is assisted by a copper-chalcogen binary phase such as Cu-S, then, the sulfur incorporation is enhanced. For the presented case, this can have the following consequences: The more sulfur is incorporated in the film, the smaller the density of sulfur vacancies (V_S) will be. Then, in accordance to the considerations above, a smaller number of defects can be assumed for such a Cu-S assisted sulfur incorporation and the formation of CH-ordered $CuInS_2$ is favored. However, an increased amount of In-S binaries exhibits the opposite behavior compared to an increased amount of Cu-S binaries. Thus, the InS phase, which is located on the surface, might reduce the incorporation of sulfur in the films.

On the other hand the presence of the InS phase during the growth might lead to the formation of further defects. It is possible that besides the formation of $CuIn_5S_8$, which serves as a storage for the excess indium, parts of the excess indium is incorporated in the $CuInS_2$ lattice by the formation of $(In_{Cu}^{2+}+2V_{Cu}^{-})$ cation neutral-defect-complexes (NDC). In the selenide system [160-162] these defect complexes form so-called ordered vacancy compounds. For the sulfide system ordered vacancy compounds have not been detected so far. However, the possibility of the existence of such structures cannot be excluded completely [163]. It can be assumed that with the presence of such defect complexes the CA-phase is stabilized. Obviously, such an effect will increase with a higher amount of indium released during the growth.

The influence of sodium on the growth of chalcopyrites is still discussed [164,165]. On the one hand Na has a similar electronic configuration as copper, and thus it is likely to assume that Na partially takes on the function of Cu. In this sense Na might imitate a Cu-rich environment by filling Cu vacancies. Additionally, enhanced sulfur incorporation in the films can be assumed which will reduce the number of defects. On the other hand the formation of a Na-In-S compound might store excess In. For the selenide system sodium has been found to influence the $CuInSe_2$ phases as well: sodium doped films exhibit less CA-ordered $CuInSe_2$ than films grown without sodium. Stanbery et al. [14] explained the role of sodium on the basis of NDCs. In this model sodium acts as a surfactant during the growth of $CuInSe_2$ by destabilizing the $(In_{Cu}^{2+}+2V_{Cu}^{-})$ defect complex and expelling excess indium from the bulk of the film. Furthermore, such ordering effects, like the CA-phase, can result from surface reconstruction during the growth. Surfactants like sodium have been found to interfere with the present ordering in those systems [166]. Thus, the suppression of the CA-phase suggests that a surface kinetic effect may play a role. Extending this model to the case of the sulfid-system, this fits well with the presented results, especially as in Cu-rich (Cu/In = 1.2) films sodium does not influence the presence of these phases.

Another effect of sodium is that both the beginning of the formation of the CA-ordered phase and the start of the transformation into the CH-phase require higher temperatures. This is in accordance with results obtained from calorimetric experiments on the selenide system [167].

As the XRD peaks related to the CA-ordered $CuInS_2$ are usually of small intensity and sometimes even under the detection limit, Raman spectroscopy has been used to identify this phase during the growth of $CuInS_2$ films. The presence of the CA-phase at different conditions such as a varying Cu/In-ratio of the precursors and doping with sodium was investigated. It was found that independent on the precursor composition the CA-ordered $CuInS_2$ forms at first. This has been explained with surface reconstruction and a temperature effect. It has been postulated that a high number of defect favors the formation of this phase. However, the transformation of CA-ordered $CuInS_2$ into CH-ordered $CuInS_2$ depends on the precursor composition. Three clear trends have been found:

- The higher the amount of Cu-S binaries during the growth the less CA-ordered $CuInS_2$ can be detected in the end of the process. This has been explained with a model of an enhanced sulfur incorporation in the films assisted by Cu binaries.
- An increasing amount of In-S compounds during the film growth results in the opposite. This finding has been embedded into the model of enhanced sulfur incorporation by extending this model to the lowering of sulfur incorporation in the films assisted by In binaries. Furthermore, the results indicate strongly that the CA-phase is stabilized by defect complexes which partially store the excess In.
- The introducton of sodium in Cu-poor precursors supports the formation of the CH-ordered $CuInS_2$. This behavior could also be introduced into the model of enhanced sulfur incorporation. Additionally, it is likely to assume that sodium acts as surfactant by destabilizing the defect complexes which are assumed to stabilize CA-ordered $CuInS_2$.

In summary, in this chapter annealing and growth of $CuInS_2$ films have been studied extensively. The *in-situ* Raman annealing experiments reveal several temperature effects, such as a temperature-induced peak shift and line broadening. On the basis of these results the temperature effect during the growth experiments could be separated. Additionally, the study of the sulfurization of pure Cu and In layers allowed the identification of the Raman active binary phases which partially occur as intermediate phases during the growth of $CuInS_2$. The growth experiments revealed clear differences due to different compositions of the precursor layers. Furthermore, the role of sodium during the growth process has been identified.

Chapter 6

Relating Structural Material Properties and Electric Device Performance of $CuInS_2$-based Thin Film Solar Cells

In this chapter the results of spectroscopic investigations on $CuInS_2$-based thin film solar cells by means of Raman scattering are presented. It is shown that there exists a relationship between the electronic quality of $CuInS_2$-based solar cells and the structural material properties of $CuInS_2$ as determined from Raman measurements. In addition, complementary photoluminescence measurements give insight into the defect structures and confirm the results from Raman spectroscopy. The empirical correlation between solar cell parameters and specific Raman features is the basis for a monitoring tool in a solar cell production line. To this end, a large sample set reflecting a wide range of process parameters has been investigated in order to obtain a broad statistical basis. The found correlation now allows a reliable forecast of the device performance in terms of the absorber quality.

This chapter is divided into two main parts: empirical relationships and discussion. In the beginning of this chapter the jV-characteristics under standard illumination conditions and the spectral photo response for a set of samples are presented. The same set of samples has been investigated with Raman spectroscopy. The correlation found between the structural properties deduced from the Raman investigations and the solar cell parameters is discussed with respect to recombination mechanisms of the heterojunction solar cells.

6.1. Sequentially Processed $CuInS_2$–based Thin Film Solar Cells

In order to compare the electric properties of photovoltaic devices and the structural properties of the corresponding absorber layers, all measurements were performed on completed $CuInS_2$-based photovoltaic devices, which have been prepared in a sequential process (RTP sulfurization). Details on the standard preparation process and the structure of a $CuInS_2$-based solar cell can be found in **chapter 4.1**. The so-called standard conditions of the preparation process have been determined empirically and reflect the optimal settings in the view of the solar cell performance. These refer to a certain sulfurization temperature (T_{sulf}), Cu/In-ratio of the precursor layer, and absorber thickness (d). One part of the samples has been prepared at these standard conditions. These samples reflect normal performance scattering. The other part of the samples has been prepared on purpose at non-standard conditions. Preparation at non-standard conditions means the variation of one of these parameters while the other parameters remain at their standard value. **Tab. 6.1** gives an overview of the investigated preparation conditions. In total a number of 45 samples has been investigated, which will reflect deviations of the absorber layer preparation. For clarity, the general behavior is shown for 3 representative samples, denoted in the following as (a), (b), and (c).

Tab. 6.1: Overview of the variation of the different process parameters.

Process Parameter	Standard Condition	Variation
T_{sulf} [°C]	500	440 – 520
Cu/In-Ratio	1.8	1.2 – 2.4
Absorber Thickness [µm]	2.1	1.0 – 3.0

6.1.1 Electric Properties

Current-voltage measurements and quantum efficiency calculation give very important information about the properties of photovoltaic devices. From the jV-measurements under illumination the characteristic solar cell parameters V_{oc}, FF, and j_{sc} are obtained. In **Fig. 6.1** three jV-curves of samples (a), (b) and (c) are presented which are representative for the investigated set of samples. The solar cell parameters of these cells as well as the fit results according to (**Eq. 3.10**) are given in **Tab. 6.2** Sample (a) has a high efficiency and high values of V_{oc}, FF, and j_{SC}, whereas the cells (b) and (c) exhibit lower values of efficiency, V_{oc}, FF, and j_{SC}.

In accordance to Ref. [87] it can be seen in **Tab. 6.2** that a worsening of the solar energy conversion efficiency is only to a minor degree induced by a reduction in j_{SC}. The dominating factors are V_{oc} and FF.

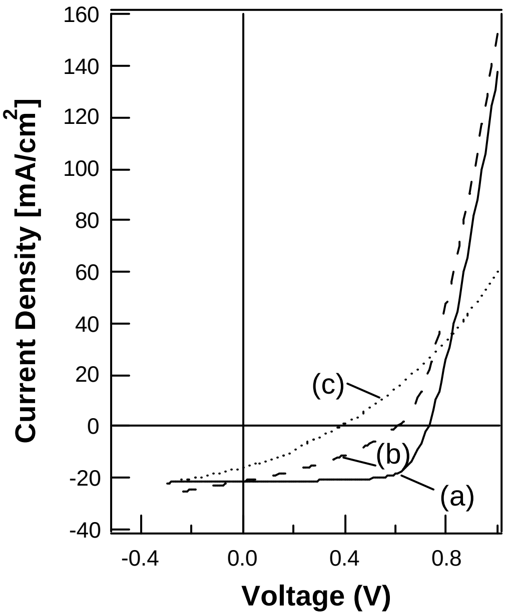

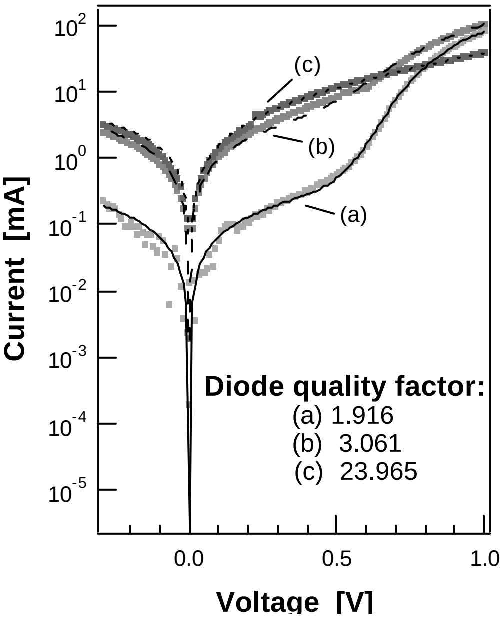

Fig. 6.1: jV-characteristics under illumination (simulated air mass 1.5) of three $CuInS_2$/CdS/ZnO devices, reflecting various energy conversion values.

Fig. 6.2: Semi-logarithmic plot of the corrected jV-curves from **Fig. 6.1** (markers) together with the fit results (lines). Each current is corrected by the short circuit current.

Tab. 6.2: Preparation conditions, solar cell parameters, and diode quality factors A as obtained from the jV-curve analysis of samples (a) – (c) of **Fig. 6.1**.

Sample	(a)	(b)	(c)
T_{sulf} [°C]	500	500	450
Cu/In	1.8	1.8	1.8
d [µm]	2.1	1.5	2.1
Efficiency [%]	11.1	4.6	1.5
V_{oc} [mV]	728	585	363
FF [%]	71.1	36.4	25.2
j_{SC} [mA/cm^2]	21.5	21.4	16
A	1.9	3.1	24

The jV-curves of the complete sample set have been analyzed using the “one-diode” model in order to determine the diode quality factors A under illumination. The analysis yields A values between 1.7 and 5.5 for most of the investigated samples. For some of the samples, which show a very low conversion efficiency (e.g. sample (c)), fitting with the “one-diode” model using (**Eq. 3.10**) results in significantly higher A values. In **Fig. 6.2** the jV-curves of the same three samples as in **Fig. 6.1** are presented in a semi-logarithmic plot together with the fit of the underlying one-diode model. Samples (a) and (b) clearly show the expected exponential current- voltage dependence in the range of around 0.5 – 0.7 V. In this voltage range the values of V_{oc} for $CuInS_2$-based heterojunctions are typically found. Sample (c) requires a high A value for simulation with the one-diode model. However, for such high A values a simulation with a one-diode or even with a two-diode model is not meaningful. From the fit results of all samples it clearly follows that a diminishing of the solar cell performance is combined with a significant increase in the diode quality factor A. The meaning of this result will be discussed later in detail (cf. **chapter 6.2.3**).

Quantum efficiency measurements have been performed in order to compare the spectral response of the $CuInS_2$-based solar cells with different solar cell performance. They reflect the charge carrier collection properties of the samples. Also, the effective band gap ($E_{g,eff}$) can be estimated from the onset of charge collection at high wavelength. **Fig. 6.3** shows the external quantum efficiency (EQE) versus the wavelength **a)** and its first derivative versus the energy **b)** for samples (a) – (c). The value of the effective band gap is given by the maximum of d(EQE)/d? and its determination should serve as a cross check of the samples. It has been calculated at around 1.5 eV and no change is observed for devices with inferior solar cell performance. All EQE characteristics (**Fig. 6.3 a)**) have in common that the generation of photoinduced charge carrier pairs takes place only for photons with an energy between the band gap of the ZnO-layer ($?_g$(ZnO) ˜ 375 nm) and the band gap of the absorber ($?_g$($CuInS_2$) ˜ 825 nm).

For all samples a reduced spectral response can be stated within the absorption range of the CdS ($?_g$(ZnO) < ? < $?_g$(CdS) ˜ 515 nm). For sample (a) only around 15 % of the photons do not create electron-hole pairs, which can further be collected. This is due to loss mechanisms such as reflection of photons and recombination of electron-hole pairs. The shift of sample (b) to lower values of EQE compared to (a) is an indication for shunt currents. Sample (c) exhibits even a lower spectral response.

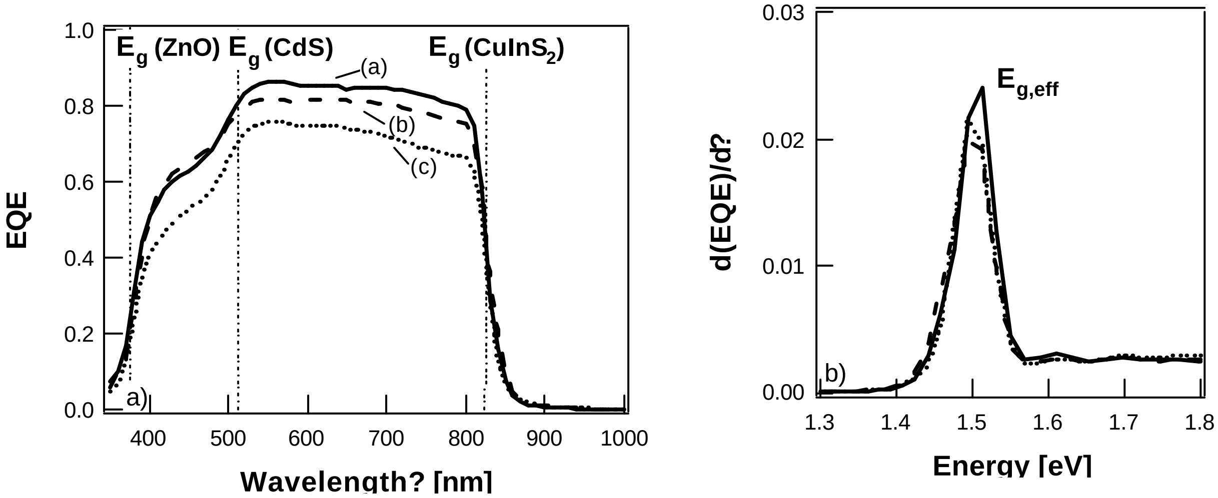

Fig. 6.3: a) External quantum efficiency versus the wavelength and **b)** the first derivative of the EQE versus the energy for the same samples as in **Fig. 6.2** (sample (a)*:* solid line, (b): broken line and (c): dotted line).

In brief, a deviation of the preparation conditions from the standard parameters results in changes of the electric properties and leads to a deterioration of the photovoltaic performance, which mainly results in lower V_{oc} and FF values. A worsening of the solar cell parameters is accompanied by high diode quality factors and results from a reduction of the collection of the charge carriers.

6.1.2 Structural Properties

The line shape of Raman peaks can be related to the coherent volume of scatterers and an asymmetric broadening is explained by the activation of non-centered phonons [168]. Therefore Raman spectroscopy was used to investigate the crystal quality of the same set of samples as analyzed with jV- and quantum efficiency measurements. The Raman spectra have been corrected with the background procedure as described in **chapter 4.2.3**. Thus, in the following figures (**Fig. 6.4** and **Fig. 6.5**) the Raman spectra are shown after the removal of disturbing signals on different wavelength scales.

6.1.2.1 Typical Raman Spectra: Absorber - Device

For the investigation of completed solar cells excitation light and scattered light from the absorber layer have to pass the ZnO/CdS window layer. For the red light excitation (632.82 nm) the light absorption in the ZnO- and CdS- layers can be estimated from the spectral response of the solar cells to be at most 15 % (cf. **Fig. 6.3**). This is valid for the wavelengths of the excitation as well as of the Raman scattered light.

In order to prove that the Raman signal of the absorber layer is not influenced by the ZnO/CdS top layers some of the samples have been investigated with Raman spectroscopy twice: first directly after the etching step, i.e. the pure $CuInS_2$ layer, and then again after the completion of the photovoltaic device. In **Fig. 6.4** the Raman spectra of the absorber layer (bottom curve) and the completed solar cell (top curve) of a representative sample are presented. The Raman spectrum of the solar cell is shifted on the intensity scale for sake of clarity. Basically the same Raman spectra have been obtained for the absorber layer and the device. As explained in **chapter 3.1** most of the $CuInS_2$ chalcopyrite-like related Raman peaks can be found in the wave number range between 220 and 380 cm^{-1}. Raman modes with smaller wave numbers could not be detected within this work. Both spectra in **Fig. 6.4** are dominated by a Raman band at approximately 291 cm^{-1}, which corresponds to the A_1-phonon-mode of $CuInS_2$. Underlying a Lorentzian profile the peak position and the FWHM have been determined. They are printed in **Fig. 6.4**. Apart from small deviations, the peak position and the FWHM are in accordance for both the absorber layer and the completed device. Close to the A_1-mode two broader peaks at the lower wave number side (at approximately 240 and 260 cm^{-1}) and two broader peaks at the higher wave number side (at approximately 320 and 340 cm^{-1}) appear in the spectra. According to **Tab. 3.4** in **chapter 3.1** these have been assigned to overlapping B_2 and E-modes, namely to B_2^2(TO)+E^3(TO), B_2^2(LO)+E^3(LO), B_2^1(TO)+E^1(TO) and B_2^1(LO)+E^1(LO). In **Fig. 6.4** the Raman bands belonging to the LO-phonon modes are slightly weaker for the completed device compared to the absorber layer. However, peaks related to the E- and B-modes are generally characterized by a low intensity. Due to its high intensity the investigation of the crystal quality of $CuInS_2$-based thin films will rely on the analysis of the dominant A_1-mode.

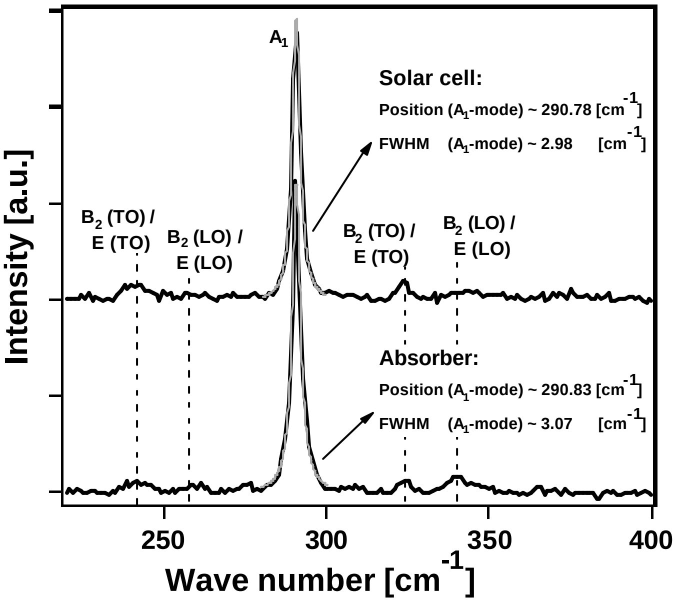

Fig. 6.4: Raman spectra of the absorber layer (bottom) and the completed device (top) of one representative sample after subtraction of disturbing signals. A Lorentzian has been used to determine the peak position and FWHM of the dominant A$_1$-mode. The Raman spectra are shifted vertically for sake of clarity.

6.1.2.2. Features of the CuInS$_2$ Raman Modes

In **Fig. 6.5** Raman spectra of samples (a), (b), and (c) (cf. **Fig. 6.1**) are shown together with the fit results. The plot presents an enlargement in the region of the A$_1$-phonon-mode of CuInS$_2$ from 280 to 305 cm^{-1}. For sample (c), a large asymmetry (a) of the A$_1$ mode towards larger wave numbers is clearly revealed. Although less pronounced, an asymmetric broadening can also be observed for spectra (a) and (b). In order to account for this non-symmetric widening, an asymmetric Lorentzian has been used for curve fitting. This asymmetric Lorentzian reads:

$$I(w)=\frac{I_0}{1+4\frac{\left(w_t\right)^2}{\left(\partial w\right)^2}} \qquad \text{with} \qquad w_t=\frac{w-w_0}{1-a\left(\frac{w-w_0}{\partial w}\right)} \quad , \qquad \textbf{(Eq. 6.1)}$$

where ?$_0$ is the center position of the A$_1$-mode, I_0 the intensity at ?$_0$, ∂? the FWHM, and a the asymmetry factor.

For the A$_1$-mode the fitting error for the peak position has been found to be less than 0.2 cm^{-1}, while the error for the FWHM values is around 5 %, and the error for the intensity is up to 10 %. The expressions in **(Eq. 6.1)** lead to negative values of a for peaks asymmetric towards larger wave numbers (higher energy side). As depicted in

Fig. 6.5 the lower wave number side is evaluated to deliver the parameter ½·FWHM. This side resembles the case of a symmetric broadening. Comparing the FWHM vales of **Fig. 6.5** and the solar cell data in **Tab. 6.2**, a relation between the cell data and the FWHM values of the A_1-mode is indicated: Cell (c) has the lowest V_{oc} and the highest FWHM value. This trend will be investigated in detail in **chapter 6.1.3**.

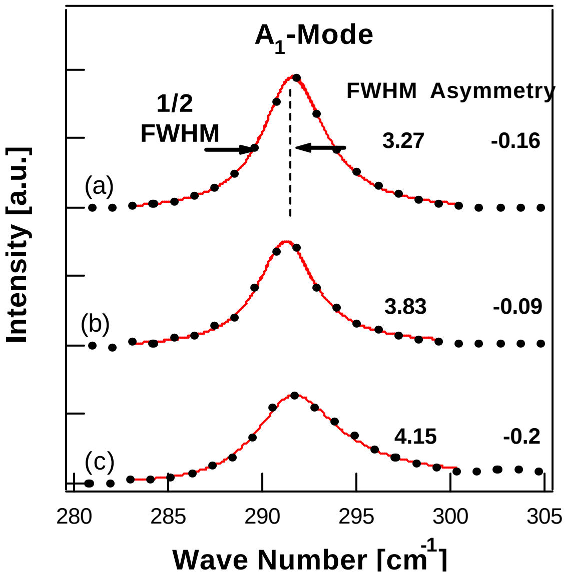

Fig. 6.5: Raman scattering intensities versus wave numbers for samples (a) – (c). The circles give the measured intensities. Full lines represent the fit using an asymmetric Lorentzian. Also the values of the FWHM and a are given for the respective curves. For sake of clarity the Raman spectra are shifted vertically.

Throughout the investigated sample set, FWHM values for the A_1-mode between 2.8 and 4.8 cm^{-1} have been determined. Furthermore, a has been assessed to values between around zero and –0.35. The asymmetry factors versus the FWHM for the A_1-modes of the complete sample set are shown in **Fig. 6.6**. A correlation is indicated between a and the FWHM despite of considerable scattering of the data. The following trend can be stated which is represented by the dash-dotted line: Larger values in FWHM are accompanied by larger values of |a|. The trend exhibits a negative slope which is due to the design of **(Eq. 6.1)**. Additionally, the increasing line width is accompanied by a slight blue shift. These two trends can be embedded into a model, which will be discussed in **chapter 6.2.1**.

It can clearly be seen in **Fig. 6.4** that besides the intense A_1-mode, less intense E- and B_2-modes related to $CuInS_2$ are present. The Raman spectra of the investigated set of samples have been analyzed with regard to the question, if a relationship exists between the intensity of the E- and B_2-modes and the intensity and FWHM of the A_1-mode.

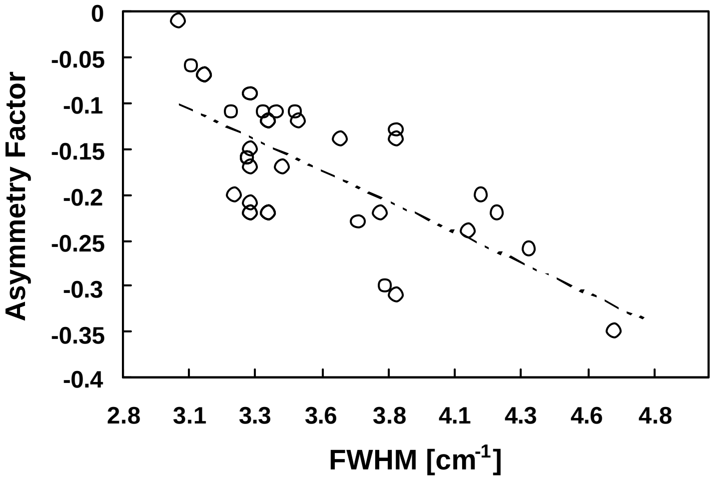

Fig. 6.6: Asymmetry factor a of the A_1-mode versus the full width half maximum (open dots). The dash-dotted line illustrates the linear regression over all data points.

In **Fig. 6.7 a)** the areal intensity of the overlapping B_2^1(LO)+E^1(LO)-modes at around 340 cm^{-1} versus the areal intensity of the A_1-mode is presented. The areal intensity, in the following referred to as intensity, has been determined by the area below the peaks. For sake of clarity, only one of the overlapping B_2^1(LO)+E^1(LO)-modes are plotted here. It follows from **Fig. 6.7. a)** that the intensities of the overlapping modes increase at around 340 cm^{-1} with increasing intensity of the A_1-mode. This means that the intensity of the E- and B_2-bands is directly related to the intensity of the dominant A_1-mode.

In **Fig. 6.7 b)** the intensity of the band at 340 cm^{-1} is plotted versus the FWHM of the A_1-mode. Obviously, no correlation can be found. Thus, the asymmetric broadening does not influence the Raman cross section of the B_2^1(LO)+E^1(LO) -modes.

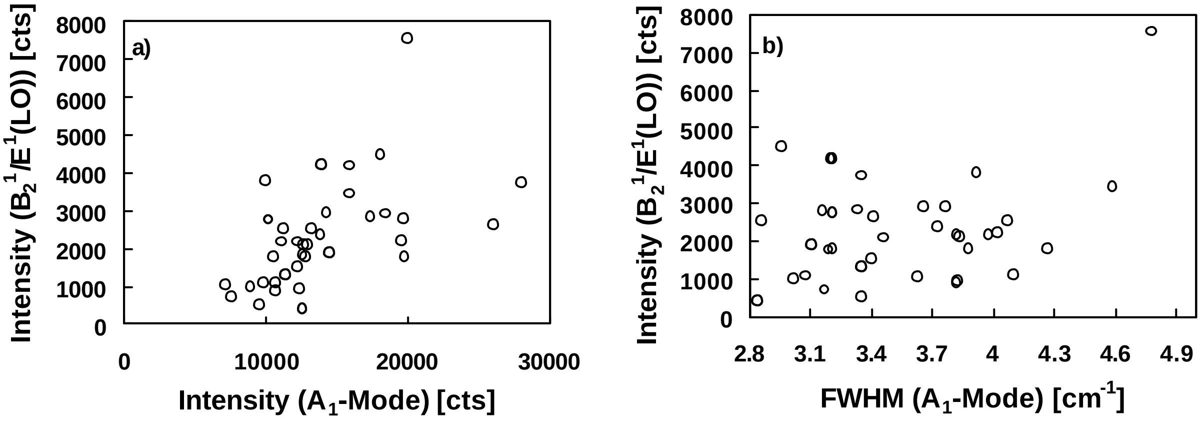

Fig. 6.7: Intensity of the B_2^1(LO)+E^1(LO)-modes at around 340 cm^{-1} versus **a)** the intensity and **b)** the FWHM of the A_1-mode.

The peak at around 260 cm^{-1}, which is assigned to overlapping B_2^2(LO)+E^3(LO)-modes, could not be observed for all the samples. The other modes found in **Fig. 6.4** exhibit the same behavior as shown here for the overlapping B_2^1(LO)+E^1(LO)-modes at 340 cm^{-1}.

The E- and B-modes show a low intensity and have been measured with a small signal-to-noise ratio. Therefore a meaningful interpretation of the line parameters of these side bands was not possible.

As discussed in **chapter 5.1** and **chapter 5.3** $CuInS_2$ can crystallize in a defect structure, the so-called CuAu phase (CA) with the space group P-4m2. The A_1-mode of this phase can be found at approximately 305 cm^{-1}. Some of the investigated samples exhibit a low intense Raman at this wave number. Therefore the relationship between the CuAu related Raman mode and the CH-ordered A_1-mode is investigated in the following. In **Fig. 6.8 a)** the shift of the chalcopyrite (CH) A_1-mode and in **Fig. 6.8 b)** the FWHMs of this mode are plotted versus the relative intensity of the mode related to CA-ordered $CuInS_2$. The latter is normalized to the intensity of the dominant CH A_1-mode. Throughout the investigated sample set a relative CuAu mode intensity between 0 and 0.16 has been determined. **Fig. 6.8** reveals that the normalized intensity of the CuAu Raman band is not related to a shift or a change in the FWHM of the chalcopyrite A_1-mode.

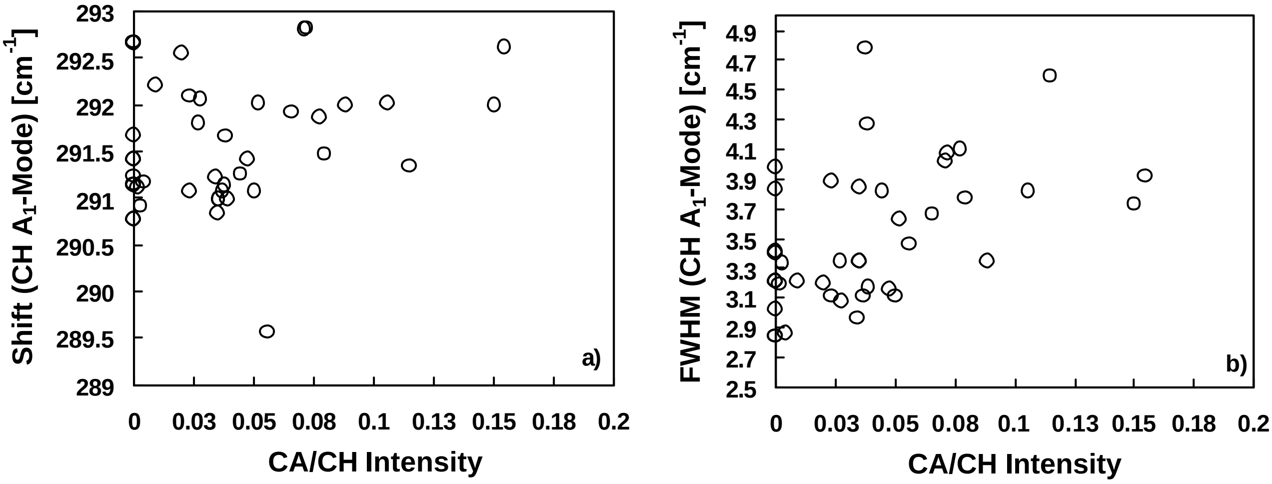

Fig. 6.8: a) Peak shift and **b)** FWHM of the CH A_1-mode versus the normalized intensity of the CuAu-related Raman band at around 305 cm^{-1}.

For larger relative intensities up to 3.5 of the CA-mode, Alvarez et al. [169] found a correlation between the intensity of this mode and a broadening and slight blue shift of the CH A_1-mode. As in the present work the CA-band at 305 cm^{-1} shows explicitly smaller relative intensities, there is no disagreement between the presented results and the findings of Alvarez et al.

Altogether, all investigated samples show only peaks related to $CuInS_2$ (cf. **Fig. 6.4**). No secondary phases which might be related to excess Cu or In atoms have been detected.

6.1.3 Link Between Structure and Device Performance by Means of Raman Spectroscopy

In this chapter it will be investigated if a relationship exists between the solar cell parameters and the crystal quality of the absorber layers as revealed by Raman measurements. Additionally, it will be asked if an indication can be found that the crystal quality does influence the diode quality factors A. The influence of the preparation conditions on the structural quality is investigated systematically. Data points at T_{sulf} = 500 °C, Cu/In = 1.8, and d = 2.1 µm correspond to samples which have been prepared at standard conditions. The aim is to introduce Raman spectroscopy as a process control.

In **Fig. 6.9** the FWHM of the dominant CH A_1-mode and the V_{oc} of the photovoltaic devices are plotted versus **a)** T_{sulf}, **b)** Cu/In, and **c)** d. The dash-dotted lines serve as guides to the eye. In **Fig. 6.9 a)** it can be seen that for $\mathbf{T_{sulf}}$ between 460 and 500°C the values of the FWHM are well below 3.5 cm^{-1}. Lower sulfurization temperatures (440 and 450°C) lead to FWHM values even larger than 4.0 cm^{-1}. The values of V_{oc} exhibit the inverse trend to the Raman FWHM. Rising T_{sulf} from 440 to 460 °C leads to a clear increase in V_{oc} - from approximately zero up to around 700 mV. Higher temperatures (up to 510 °C) are accompanied by almost constant values for V_{oc}.

The **Cu/In-ratio** has been varied from 1.2 to 2.4. Despite one value (Cu/In = 1.4 and FWHM = 2.9 cm^{-1}) it is visible in **Fig. 6.9 b)** that the Cu/In-ratios between 1.6 and 2.0 are combined with the smallest FWHM values (between 3.0 and 3.5 cm^{-1}). For smaller or larger Cu/In-ratios FWHM values of approximately 3.8 cm^{-1} are found.

However, the V_{oc} shows only for Cu/In = 2.4 a value of 650 mV. For all other Cu/In-ratios the open circuit voltages are in the range of 690 - 720 mV.

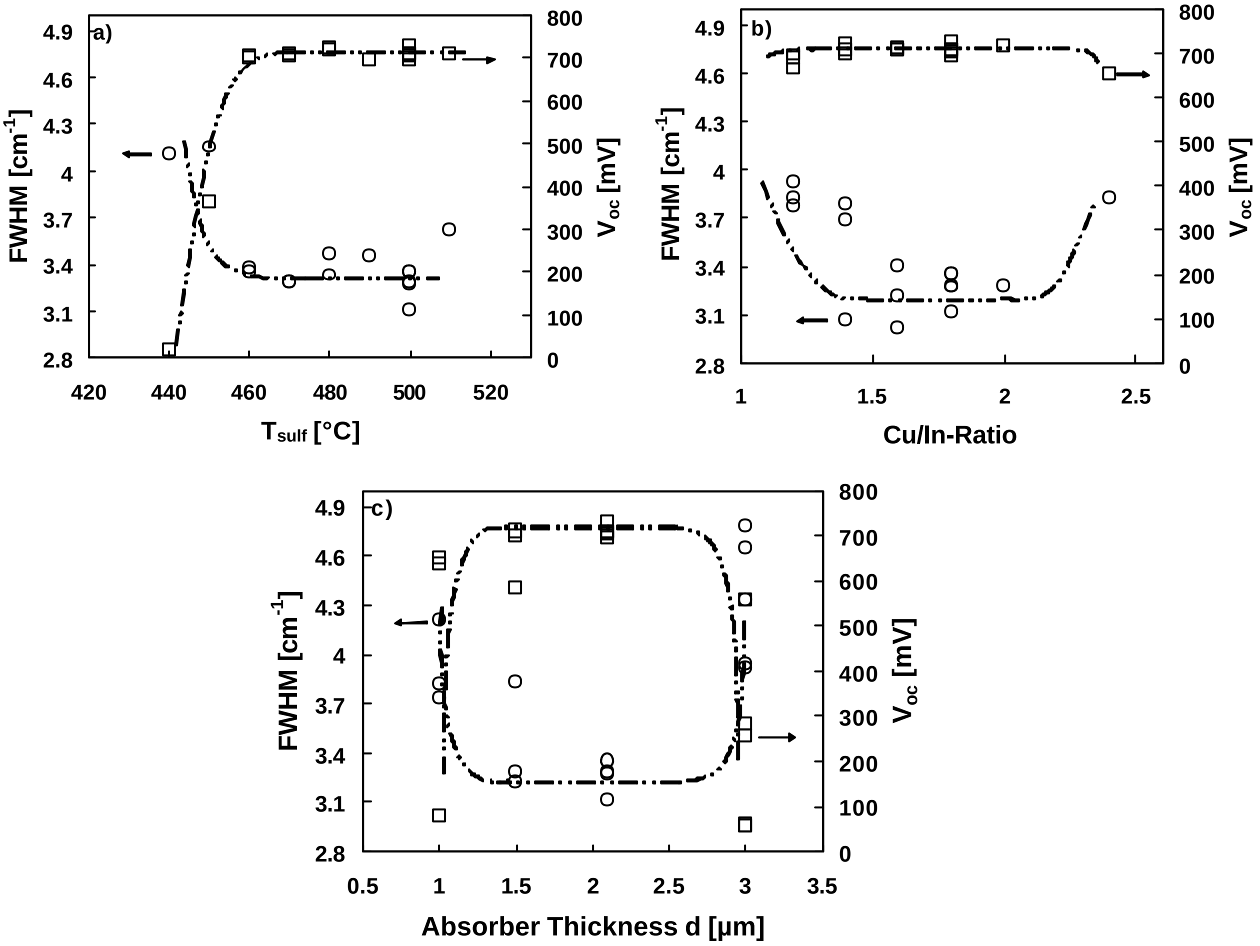

Fig. 6.9: FWHM of the Raman A_1-mode (left axis, circles) and V_{oc} of the device (right axis, squares) versus **a)** sulfurization temperature, **b)** Cu/In-ratio, and **c)** absorber thickness. The dash-dotted lines serve as guides to the eye.

The **absorber thickness** has been varied from 1.0 to 3.0 µm. The measured values of the Raman FWHM and cell V_{oc} are shown in **Fig. 6.9 c)**. For 1.5 µm > d and d > 2.1 µm FWHM values larger than 4.2 cm^{-1} are found. For 1.5 µm < d < 2.1 µm the FWHM values are around 3.3 cm^{-1}, only one value for d = 1.5 µm shows a line width of 3.8 cm^{-1}. The inverse behavior is found for the V_{oc} values: For 1.5 µm < d < 2.1 µm the V_{oc} shows values around 700 mV, apart from the one sample with 1.5 µm thickness at around 600 mV. For an absorber thickness below 1.5 and above 2.1 µm V_{oc} values below 300 mV are found.

Assuming a clear trend between the preparation conditions and the FWHM on the one hand and V_{oc} on the other hand in **Fig. 6.9**, it must be stated that for certain preparation parameters a significant scattering of the FWHM values as well as the V_{oc} values occurs. However, as repeated measurements of the same sample revealed approximately the same FWHM values within a relative error of 5 %, experimental errors of the Raman measurement can be excluded. The same is valid for the jV-measurements. Thus, the scattering appears to reflect on the one hand structural differences of samples prepared under identical conditions and on the other hand instability of the preparation process itself. Therefore it is necessary to discuss mean values.

Remarkably, a change of the sulfurization temperature and the absorber thickness has a more drastic effect on the structural as well as the electric properties – here represented by the V_{oc} - than a change of the Cu/In-ratio. Hence, it can be assumed that a variation of the Cu/In-ratio in the investigated range is tolerable in terms of both the structural and the electric properties.

Fig. 6.9 clearly shows a correlation between structural properties of the absorber layers – represented by the FWHM values of the CH A_1-mode - and the open circuit voltage of the photovoltaic device. In the following this correlation shall be analyzed in detail and extended to the solar cell parameters FF and j_{sc}. In **Fig. 6.10** the solar cell parameters **a)** V_{oc}, **b)** FF, and **c)** j_{sc} are plotted as a function of the FWHM values of the A_1-mode for all investigated samples. The dash-dotted lines illustrate the observed trends. **Fig. 6.10 a)** shows that for FWHM values up to 3.8 cm^{-1} the V_{oc} values scatter between 695 and 730 mV – these values are in the range where the best solar cell performances have been achieved (cf. **chapter 3.3**). Roughly at 3.8 cm^{-1}, a decrease in V_{oc} values – down to 20 mV – takes place. A similar behavior is found for the values of FF in **Fig. 6.10 b)**. Here, also a FWHM of around 3.8 cm^{-1} marks a boundary between a plateau (at approximately 70 %) and a decline (down to approximately 25 %). For the FF values a larger scattering must be stated compared to the V_{oc} values. For the values of j_{sc} (**Fig. 6.10 c)**) a similar behavior can be observed. An almost constant behavior is found for FWHM values < 3.8 cm^{-1}, while for FWHM values > 3.8 cm^{-1} a large scattering at lower values of j_{sc} (down to ~ 5 mA) can be found. From these plots it follows that a FWHM of around 3.8 cm^{-1} appears to be a critical point (indicated by the arrows) and is therefore interpreted in terms of a terminating condition. When the FWHM exceeds this value, the deterioration of the crystal structure starts to worsen the electric properties of the device drastically. The findings from **Fig. 6.9** and **Fig. 6.10** give a strong hint that Raman spectroscopy is indeed suitable as a process control.

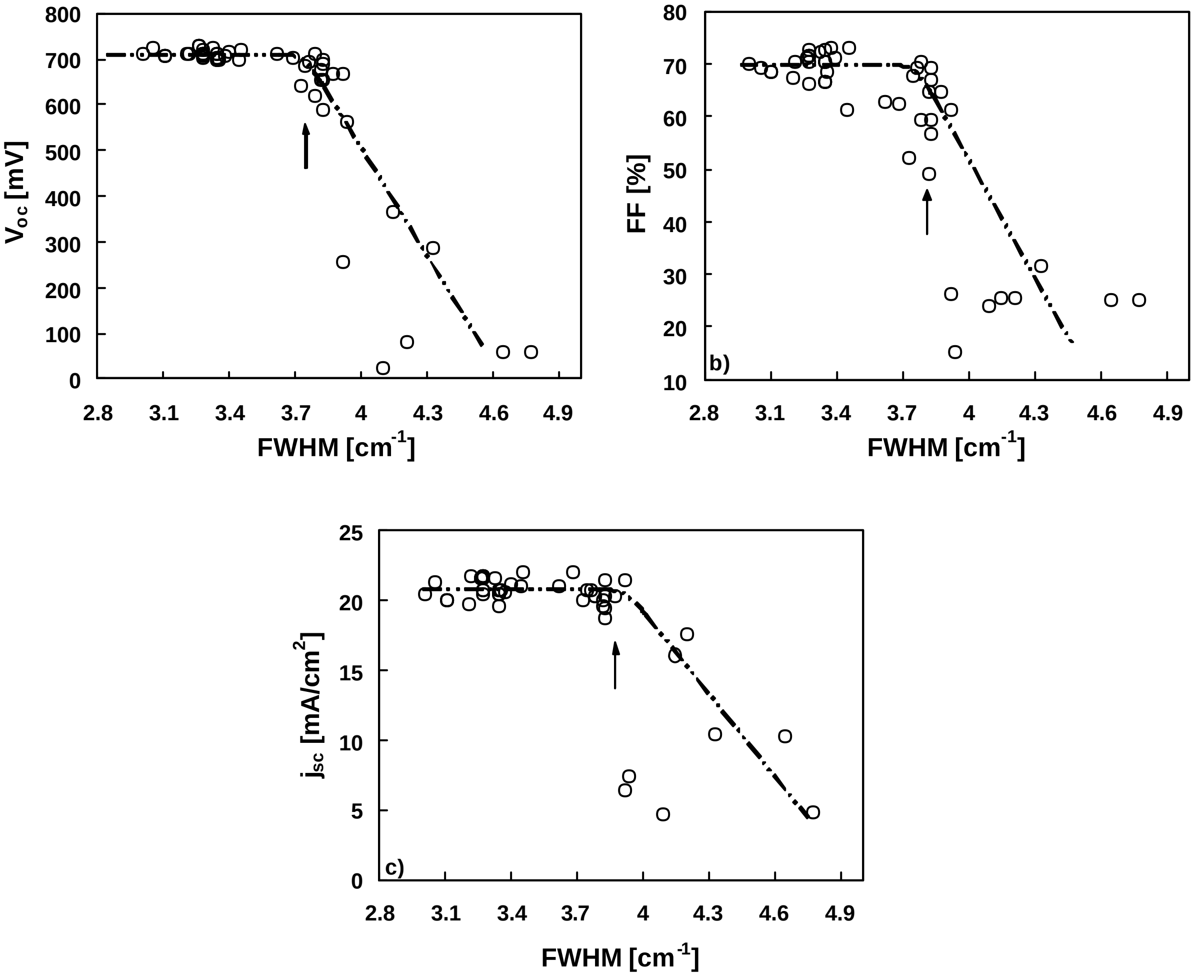

Fig. 6.10: Solar cell parameters versus the FWHM of the Raman A_1-mode, **a)** open circuit voltage, **b)** fill factor, and **c)** short circuit current density. The dash-dotted lines serve as guides to the eye, while the arrows indicate the critical FWHM values.

In the next step the results from the fitting analysis of the jV-curves under illumination using **(Eq. 3.10)** are combined with the FWHM values. The diode quality factor A as a function of the FWHM is plotted in **Fig. 6.11**.

The following trend, depicted by the dash-dotted line, can be observed: for FWHM values < 3.8 cm^{-1} a diode quality factor around 2 or even below has been determined. A further increase of the FWHM values is accompanied by A values larger than 2. Hence, at approximately the same FWHM value as for V_{OC} and FF a turning point (indicated by the arrow) occurs. Although some samples exhibit very large A values, which indicates that the investigated photovoltaic devices cannot be properly described by diode-models, these are also included in **Fig. 6.11**. **Fig. 6.11** clarifies that the deterioration of the crystal quality of the investigated samples is combined with larger A values. This indicates a change in the recombination mechanism and will be discussed in detail in **chapter 6.2.3**.

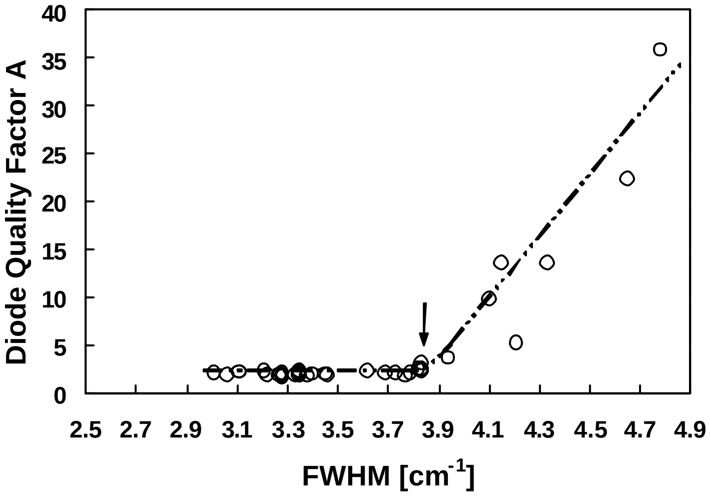

Fig. 6.11: Diode quality factor A, as determined from the analysis of the jV-curves under illumination, versus the FWHM of the Raman A_1-mode. The dash-dotted line serves as a guide to the eye, while the arrow indicates the critical FWHM value.

The presented results for V_{oc}, FF, j_{sc} and A as a function of the FWHM clearly show that there exists a border, from which on a worsening of the crystal quality induces a change of the recombination mechanism and leads to a deterioration of the solar cell performance. This relationship proves the capability of Raman spectroscopy as a process monitoring tool.

In order to investigate the role of the CA-phase on the presented sample set, the solar cell parameters have also been related to the relative amount of CA-ordered $CuInS_2$ Raman mode. This amount can be expressed by the intensity ratio of the A_1-mode of the CA-phase and the A_1-mode of the CH-phase (CA/CH). **Fig. 6.12** shows the relative intensity of the CA-mode versus various preparation conditions. In order to inspect the influence of the CA contribution on the solar cell performance, the V_{oc} values are shown additionally. The dash-dotted lines indicate the observed trends. At this point it should be stressed that the scattering of the CA/CH ratio might be due to process instabilities.

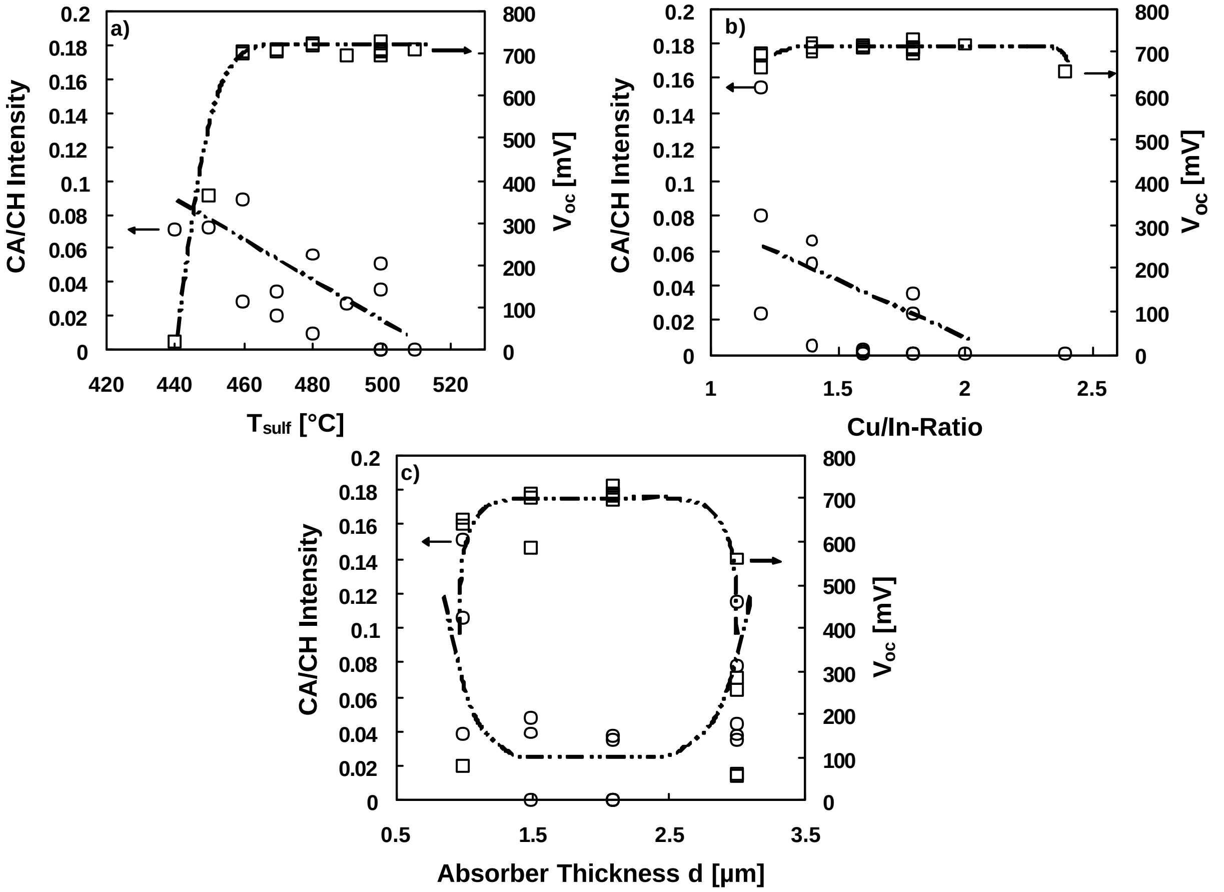

Fig. 6.12: Relative CA contribution to the CH A_1-mode (left axis, circles) and V_{oc} of the photovoltaic device (right axis, squares) versus **a)** sulfurization temperature, **b)** Cu/In-ratio, and **c)** absorber thickness. The dash-dotted lines serve as guides to the eye.

Three trends can be stated for the investigated samples between the relative CA contribution and the varied preparation conditions:

- The higher the sulfurization temperature, the smaller the amount of CA-ordered $CuInS_2$.
- The higher the Cu/In-ratio the smaller the CA-phase.
- For an absorber layer thickness between 1.5 and 2.1 µm the CA contribution exhibits a minimum.

The first two trends are also confirmed by the results of the growth experiments (cf. **chapter 5.3**) and the findings of other groups [170,171]. The influence of the thickness of the absorber layer, which has not been investigated so far, can be explained by a change in the kinetics of the CA- and the CH-formation. A kinetic limitation on the growth can result in the fact that samples with thicker precursor layers are not completely sulfurized.

No correlation can be observed between the V_{oc} values and the normalized CA-mode intensity. The same has been found when the relative CA contribution is plotted versus FF and j_{sc}, respectively. Within the investigated range of variation of the preparation conditions for $CuInS_2$ films the CA contribution does not influence the performance of the completed photovoltaic devices.

6.1.4 Combination of Structural and Electric Properties with the Results from Photoluminescence Measurements

Photoluminescence (PL) allows quantifying and qualifying defects in semiconductors. Here, it is investigated if there exists a correlation between the PL spectrum of $CuInS_2$ films and their crystalline quality assessed by Raman spectroscopy. **Fig. 6.13** represents the photoluminescence spectra measured at 10 K for the same samples (a), (b), and (c) as in **Fig. 6.1**. The intensity of the three spectra has been normalized to the peak at higher energy of the radiative recombination (PL3) and has been plotted versus the energy. All investigated samples show two strong luminescence signals. The broad peak (PL1) has a maximum at around 1.1 eV and is assumed to originate from an overlap of several peaks [172]. An indication that this luminescence signal is indeed due to an overlap of different peaks is given by the shifted center position of this signal (cf. **Fig. 6.13**). So far, these low energy signals could not be assigned to specific transitions. Siemer and coworkers [172] interpreted the signal at around 1.53 eV (PL3) as an excitonic transition. This interpretation seems questionable, as usually excitonic transitions are characterized by a line width of around 10 meV, while the peak observed here exhibits a significantly larger line width. An additional very low intense peak appears at around 1.45 eV (PL2). This emission has been assigned to a transition between a sulfur vacancy (V_S) state and a copper vacancy (V_{Cu}) state [108]. The signal at around 0.93 eV is an artifact of the laser.

In **Fig. 6.14 a)** the V_{oc} values are plotted versus the areal intensity ratio PL1/PL3 for the eight investigated samples which are considered to be representatives of the complete sample set. These samples have been chosen to cover the whole range of different solar cell performances. The following trend – indicated by the dash-dotted line - can be observed in **Fig. 6.14 a)**: A deterioration of the solar cell performance is accompanied by an increase of the broad luminescence at 1.1 eV (PL1).

In **Fig. 6.14 b)** the FWHM of the CH A_1-mode is presented as a function of the same normalized PL intensity (PL1/PL3). The dash-dotted line illustrates the observed trend. An increase of the normalized intensity is combined with increasing FWHM values.

In conclusion, the increase of the normalized intensity PL1 is an indication for an increased density of defect centers. This interpretation is also supported by the findings of Meeder and coworkers [173]. They found a correlation between the increasing intensity of a broad luminescence in $CuGaSe_2$, which supposedly corresponds to PL1, with an increased density of defect centers revealed by defect absorption measurements. As the FWHM and the PL1 intensity exhibit an almost linear relationship, it can be concluded that the broadening of the $CuInS_2$ Raman A_1-mode is associated with defects which can be revealed by PL experiments. However, the origin of the defects participating in the recombination path of PL1 is not clear yet.

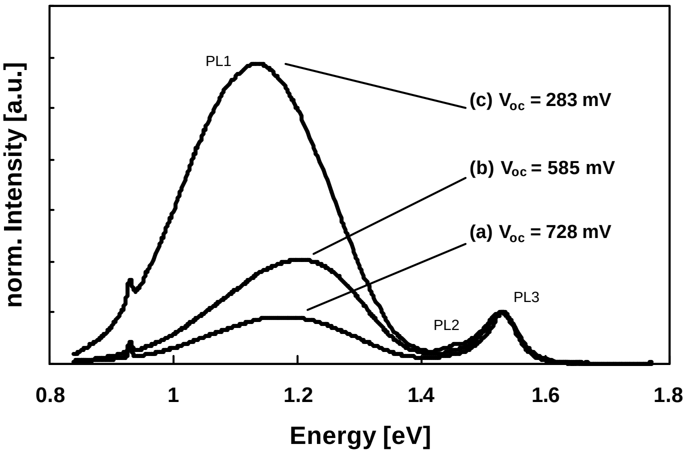

Fig. 6.13: Photoluminescence (normalized) intensity for samples (a), (b), and (c) of **Fig. 6.1**. The spectra were recorded at 10 K and have been normalized to the emission at around 1.53 eV (PL3). Additionally, the V_{oc} values of the corresponding samples are given.

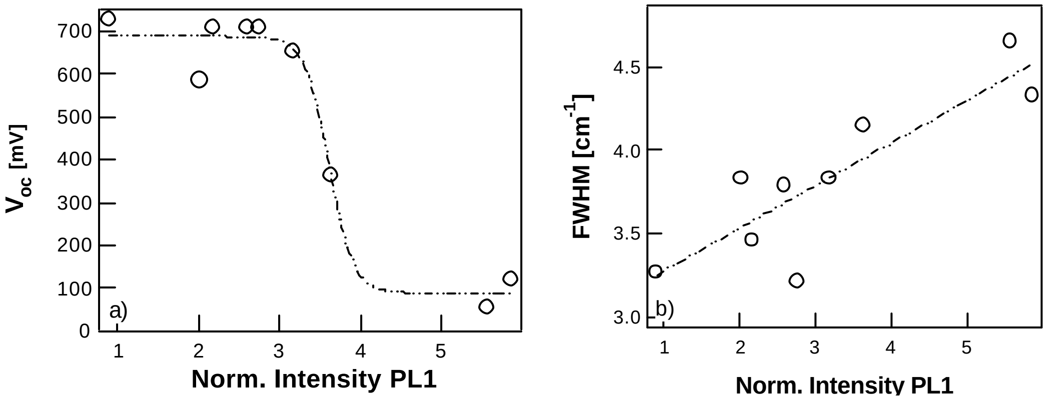

Fig. 6.14: V_{oc} **a)** and FWHM **b)** of the A_1-mode as a function of the normalized intensity of the PL1 band. The dash-dotted lines serve as guides to the eye.

6.2 Discussion

The subject of this part of this thesis was to find a relation between structural absorber qualities and device performance. It has been proven that for the used Raman excitation light of 632.82 nm neither the CdS buffer layer nor the ZnO window layer influence the Raman signal of the absorber layer. Obviously, this is due to the larger energy band gaps of CdS and ZnO compared to $CuInS_2$. Thus, the form of the Raman A_1-mode of $CuInS_2$ does not change as CdS/ZnO is deposited during the completion of the solar cells. This allows monitoring the crystalline quality of the absorber layers in completed devices.

All samples have been prepared with a Cu-rich composition ($1.2 < Cu/In < 2.4$). Previous studies showed [88] that the surface composition of the films becomes Cu-poor after the removal of the binary CuS phase (etching step). This Cu depleted region has been estimated to be around 200 nm [169], while deeper layers of the samples show a stoichiometric composition. Nevertheless, throughout the investigated sample set only Raman peaks related to $CuInS_2$ – in the chalcopyrite and the CuAu phase – have been observed. No additional In-rich phase has been detected. Thus, the Cu deficiency might be stored in electrically neutral defect complexes ($In^{2+}_{Cu}+2V^{-}_{Cu}$) [114] which exhibit a non-periodical distribution within the lattice [174].

The following discussion is divided into three parts. At first the characteristic features of the Raman spectra are discussed in detail with respect to the meaning of the increasing line width of the $CuInS_2$ A_1-mode. Then, the dependence of the growth and structure of $CuInS_2$ films on the preparation conditions is explained. In the last part the observed relationship between the Raman line width and the solar cell parameters is discussed in terms of defect densities and recombination in $CuInS_2$-based solar cells.

6.2.1 Broadening of the A$_1$-Mode of CuInS$_2$-based Solar Cells due to Defects

The analysis of Raman line shapes can yield important information about structural disorder in the investigated films [175]. In general structural disorder is a result of point defects or extended dislocations such as micro-crystalline grain boundaries. The investigated set of samples reveal an asymmetric broadening (up to ?(∂?) = 2 cm^{-1}, cf. **Fig. 6.6**) and a slight blue shift. As the data of the FWHM characterize the crystal quality of the absorber film after its preparation, it should be an indication for the density of localized and extended defects. As shown in **chapter 3**, the number of possible point defects in the ternary semiconductor CuInS$_2$ is 12 and accordingly very large is the number of possible mixed defect pairs and clusters. Only little is known about the densities of specific point defects and their formation energies. Thus, at that point an empirical approach appears to be most profitable: The reduction in crystal quality revealed by the increase in line width of the Raman A$_1$-mode of CuInS$_2$ gives rise to an increased density of defects. This approach is further supported by the findings from the PL experiments (cf. **Fig. 6.14 b)**).

Richter et al [168] explained the asymmetric broadening combined with a shift of the Raman signal by use of the so-called **phonon confinement** or **spatial correlation length model**: Phonons in imperfect crystals are confined in space by structural disorder. This confinement leads to an uncertainty of the crystal momentum, which causes a break down of the Raman selection rule. Thus, phonons at **q** ? 0 can be observed which contribute to the Raman signal. The correlation length L is understood as the length of a crystal region in which the phonons can propagate freely. Beyond L the phonons get scattered from crystal imperfections. Thus, the phonon lifetime is reduced by scattering at defect sites and a broadening of the Raman line takes place: The smaller the correlation length, the larger the Raman line width. Therefore the Raman line width is a sensitive indicator for the crystal quality of semiconductors. Mathematically, the Raman line shape is a superposition of Lorentzian line shapes, which are centered at ? (**q**) and weighted by the wave vector uncertainty, whereas the wave vector uncertainty is caused by the confinement. For the mathematical description of the confinement a Gaussian can be assumed.

Then, the line shape reads

$$I(w) \cong \int_0^1 \exp(\frac{-q^2L^2}{4}) \frac{dq^3}{(w - w(\vec{q}))^2 + (\partial w/2)^2} \quad , \qquad \textbf{(Eq. 6.2)}$$

where q is in units of 2p/a, a is the lattice constant of $CuInS_2$, ? (**q**) is the phonon dispersion curve, and ∂? is the natural line width. The integration takes place over the entire Brillouin zone. For L ? 8, the line shape turns into a Lorentzian centered at ? (**0**). Hence, the asymmetric broadening is dependent on the dispersion relation ? (**q**). If the phonon branches exhibit no dispersion, a homogeneous broadening would be expected. However, this is not the case for real crystals. Many semiconductors exhibit a negative slope of the phonon dispersion curves. As can be seen in **(Eq. 6.2)**, this results in an asymmetric broadening towards smaller wave numbers together with a red shift of the Raman signal. This has been found for different materials [17,18,168,176].

For the presented samples an asymmetric broadening of the Raman A_1-mode towards higher wave numbers and a slight blue shift have been observed. In order to explain this by phonon confinement a positive slope of the phonon dispersion curve of the $CuInS_2$ A_1-band is required. The theoretically determined dispersion relation for $CuInS_2$ [62] indeed shows that the phonon branch of the A_1-mode (8.14 THz, marked red in **Fig. 3.4**) exhibits a positive slope in the G ? Z direction. Furthermore, most of the phonon branches of the $CuInS_2$ A_1-mode appear to increase similarly in the vicinity of the G point. The three-dimensional integration over the entire Brillouin zone may be approximated by a one-dimensional integration in a spherical Brillouin zone using an averaged dispersion curve. In this case, the resulting Raman line shape is only determined by the averaged phonon dispersion with respect to the spherical Brillouin zone. Hence, the found asymmetric broadening and blue shift for $CuInS_2$-based solar cells can be explained by the phonon confinement model. At this point it is desirable to quantify the relation between the increasing of the line width of the $CuInS_2$ A_1-mode and the diminishing of the correlation length. Unfortunately, the data of the calculated phonon dispersion relation for this $CuInS_2$ was not available, so the integration in **(Eq. 6.2)** could not be done. However, with regard to the exponential term in **(Eq. 6.2)** the confinement is only noticeable for correlation lengths smaller than 200 Å. In the literature correlation lengths between 150 and 50 Å have been reported for various micro crystalline and single crystalline semiconductor materials [18,168,176-179]. Thus, it can be assumed that the L values are within the same range for the samples investigated here.

The phonon confinement model is based on the relationship between L and the density of defects (N_d). This relationship can be described quantitatively, if the correlation length is interpreted as the average distance between two crystal defects. Then, the correlation length is related to the defect density in a third root dependency:

$$\left(N_d\right)^{-\frac{1}{3}} = L \quad . \qquad \textbf{(Eq. 6.3)}$$

In **Tab. 6.3** different N_d values with the corresponding correlation lengths are given.

Tab. 6.3: Calculated values of L according to **(Eq. 6.3)**.

N_d [cm^{-3}]	1	$5\cdot10^{16}$	$1\cdot10^{17}$	$1\cdot10^{18}$	$5\cdot10^{18}$	$1\cdot10^{19}$	$5\cdot10^{19}$	$1\cdot10^{20}$	$5\cdot10^{20}$	$1\cdot10^{21}$
L [Å]	500	270	220	100	60	50	27	22	13	10

Typical defect densities in the bulk of $CuInS_2$ absorber layers, determined by admittance measurements [130] and Kelvin probe force microscopy [180], are between $1\cdot10^{16}$ and $1\cdot10^{17}$ cm^{-3}. In addition to this the analysis of jV-curves recorded in the dark revealed that the defect density increases in the vicinity of the absorber/buffer layer interface and typical values are around $1\cdot10^{19}$ cm^{-3} [119]. At this point it is likely that the defect densities, which cause the asymmetric broadening of the Raman signal, are between these values especially as the Raman signal is related to the surface near region. Therefore L values within the range of 150 – 50 Å are expected.

It has been shown in **Fig. 6.7** and **Fig. 6.8** that the asymmetric broadening of the A_1-mode does not influence the Raman cross section of the E- and B_2-modes of CH-ordered $CuInS_2$ or of the peak assigned to the A_1-mode of CA-ordered $CuInS_2$. Due to the low scattering efficiency of these bands no reliable statements concerning the line shapes of these modes could have been done. The E- and B_2-mode intensities correlate only with the intensity of the A_1-mode. No correlation has been found between the FWHM of the CH A_1-mode and the CA-related mode. The missing of any correlation between these two phases has a certain implication for the investigated set of samples: In principle, the CA-ordered $CuInS_2$ is understood as a defect phase of the chalcopyrite lattice due to the exchange of the cations of type I and III. Additionally, it has been found that this defect phase coexists with the chalcopyrite phase in the form of domains [69]. Thus, the presence of domains of different crystalline phases might lead to an increase of defects caused by the lattice mismatch between the CH- and the CA-phase. This mismatch can be accommodated by point defects such as antisites or vacancies, in the case of $CuInS_2$: Cu_{In}, In_{Cu}, V_{Cu}, and V_{In}. For samples containing a large amount of CA-ordered $CuInS_2$ indeed an increased number of defects has been observed [169]. However, for the investigated set of samples the amount of CA-ordered $CuInS_2$ is very small. Therefore, it can be concluded that defects which give rise to the asymmetric broadening of the chalcopyrite A_1-mode do not origin from the CuAu defect phase.

6.2.2 Influence of the Preparation Conditions on the Growth and Structure of $CuInS_2$

It has been found that the FWHM of the Raman A_1-mode of the $CuInS_2$-based absorber layers and the corresponding solar cell parameter V_{oc} of the completed PV devices are dependent on the preparation conditions. In the following the observed trends are discussed. In this context also the role of CA-ordered $CuInS_2$ shall be considered.

Variation of T_{sulf}

It has been shown (cf. **Fig. 6.9 a)**) that for the presented samples a sulfurization temperature between 460 and 500 °C leads to both, the best crystal quality and the best device performance. From the findings of **chapter 5.3** it is clear that a temperature exceeding 400 °C is required for the formation of CH-ordered $CuInS_2$. In general the formation of a crystal phase is accompanied by the formation of defects: the lower the growth temperature, the more defects are formed. Increasing the temperature up to the melting point temperature induces a healing of the defects. Thus, not only the formation of the material itself, but also the healing of defects is a kinetically limited process. On the other hand an increase of T_{sulf} above a certain temperature is accompanied by an increasing amount of defects. This can be explained by temperature-induced evaporation of sulfur atoms from the CIS-lattice and would result in an increased amount of sulfur vacancies. In other terms, equilibrium between the healing of defects and the formation of new defects has to be found for optimum growth conditions.

Variation of the Cu/In-Ratio

Compared to the variation of T_{sulf} and the absorber thickness, the absorber layer is more tolerant to a variation of the Cu/In-ratio, whereby Cu/In-ratios between 1.4 and 2.0 hold the best crystal quality. Two different layers – the $CuInS_2$ layer and on the top a CuS layer - are obtained after absorber preparation under Cu-rich conditions. As discussed in **chapter 5.3** the Cu excess and therefore the Cu-S phase promotes the chalcopyrite formation and lowers the probability for the formation of defects. Nevertheless, an increase of the Cu/In-ratio is not combined with a better structural quality of the $CuInS_2$ layer. Moreover, a deterioration of the crystal can be stated for Cu/In > 2.0. A possible explanation might be that the Cu-S phase still has its function as promoter, while simultaneously the significantly increased amount of CuS leads to more defects. Those defects can be generated if the CuS phase is not only located on top of the $CuInS_2$ layer, but also between single $CuInS_2$ grains in non negligible amounts. As a result smaller grain sizes might occur and more defects due to the increased number of grain boundaries. For Cu/In > 1.8 no CA-ordered $CuInS_2$ has been detected, thus this effect is not induced by this phase.

Variation of the Absorber Thickness (d)

The variation of the absorber thickness imposed a deterioration of both, the crystal quality and the solar cell performance, for d < 1.5 µm and d > 2.1 µm. The effect of this variation on the growth of $CuInS_2$ is kinetically based. For the growth of $CuInSe_2$ from Cu-In-Se stacks Wolf et al. [181] found: the thinner the precursor layer the lower the temperature of the endpoint of the formation during the heating period. This is explained by a diffusion limited growth process. In contrast, for the formation of $CuInS_2$ films Pietzker [182] proposed a stress induced growth mechanism: Due to the difference in the expansion coefficients of the intermetallic phases and $CuInS_2$ stress is induced during the heating period within the growing $CuInS_2$ layer. This leads to the formation of micro-cracks as soon as a critical value of stress is exceeded. Along these cracks Cu and In atoms diffuse to the surface and form further layers of $CuInS_2$. In order to explain the influence of the absorber thickness on the growth, both interpretations can be combined: For precursor layers thinner than 1.5 µm the formation of $CuInS_2$ is completed at significantly lower temperatures compared to thicker absorber layers. A further increase of the temperature might lead to the formation of sulfur vacancies, as discussed in the previous section, whereas precursor layers, which are significantly thicker than 2.1 µm, require higher temperatures. In this case $CuInS_2$ films are not completely sulfurized, and, consequently, thicker precursor layers correspond to the case of too low sulfurization temperatures.

The amount of the CA-phase was found to be smallest for 1.5 µm = d = 2.1 µm, while a significant increase can be stated for films thicker or thinner. However, purely kinetically based considerations imply that no CA-ordered $CuInS_2$ occurs for layers thinner than 1.5 µm. Thus, the presented model has to be extended by considerations related to the other phases occurring during the sulfurization: Thinner precursor layers yield a thinner Cu-S binary layer on top of the $CuInS_2$ film. Thus, the $CuInS_2$ may not completely be covered by Cu_2S during the growth. According to the defect model in **chapter 5.3**, a smaller amount of Cu-S can lead to an increased amount of defects during the formation of CH-ordered $CuInS_2$. This explains the presence of CA-ordered $CuInS_2$ in precursor layers thinner than 1.5 µm.

Changes of the preparation conditions influence both, the solar cell performance and the structural quality of the investigated samples. Furthermore, as indicated by **Fig. 6.9** a correlation between V_{oc}, FF, and j_{sc} of the solar cells and the FWHM of the A_1-mode of CH-ordered $CuInS_2$ originating from the absorber layer has been revealed. However, no correlation has been observed for the CA-phase. Thus, the correlation between the structural and electric properties of the investigated samples is discussed without considering this crystalline phase.

6.2.3 Defect Density-induced Change of the Recombination Mechanism in $CuInS_2$-based Solar Cells

It has been shown earlier that the dominant recombination of $CuInS_2$-based solar cells under illumination proceeds at the absorber/buffer interface [86,119]. This recombination path imposes the limitation of the open circuit voltage [183]. In addition to this, Reiss [184] found that the interface recombination mechanism is both thermally activated and tunneling enhanced.

The following discussion will be based on these findings and the model explained in **chapter 6.2.1**: an asymmetric broadening of the A_1-mode due to an increasing number of defects.

One of the main experimental results of this thesis is the connection between the FWHM of the A_1-mode and the solar cell performance. At a certain FWHM a decrease of the V_{oc} values as well as the FF values has been observed, which can be understood as a terminating condition or a controlling condition for the quality of the absorbers. Crystal defects which confine the phonon correlation length in the absorber layer can be considered to limit the V_{oc} in the range of large FWHM values. These defects may form trap states in the gap. A correlation between the structural quality and the device performance is expected, as the recombination rate depends on the density of defects. This interpretation is even supported by the findings of the PL experiments. On the other hand, not only crystal defects may limit the open circuit voltage and the fill factor. This is indicated by the saturation behavior of both quantities: At low FWHM values, the V_{oc} and FF values remain at approximately 0.7 V and 70 %, respectively, and are no longer dependent on the Raman line width. The relationship of the PL quantities and V_{oc} exhibits almost the same behavior. Thus, other factors must inhibit the open circuit voltage to take on its calculated ideal value of about 1000 mV [185].

The open circuit voltage V_{oc} of solar cells depends logarithmically on the saturation current J_0. Whether the transport mechanism of the pn-junction is governed by recombination in the space charge region or at the interface, the saturation current density is in direct correlation with the density of recombination sites N_d, this means that $J_0 \sim N_d$. Thus, V_{oc} should show the relationship $V_{oc} \sim \ln(N_d)$. This has indeed been confirmed by admittance spectroscopy evaluation for $CuInS_2$ samples [186] sulfurized in a CTP process. In principle, this logarithmic relationship describes both mechanisms, thermally activated and tunneling enhanced recombination. The relationship between the FWHM of the Raman signal and the density of trap states is not known as the integration of **(Eq. 6.2)** could not be done.

However, in order to find an explanation for the correlation between the solar cell parameter and the structural properties, two different models can be considered.

Both models are based on the fact that the recombination mechanism of cell (a) in **Fig. 6.1** is located at the absorber/buffer interface.

Model 1: Transition from Dominating Interface to Dominating Bulk Recombination

In the first model it is assumed that interface recombination initially determines photovoltaic properties. An increased density of defects may cause a change from interface recombination rate to bulk recombination assuming the interface recombination to remain constant. In order to explain this model, the saturation current is expressed as a sum of space-charge limited and interface recombination:

$$J_0 = q\Delta x \frac{n_i}{t} + qS_p N_V \exp(-\frac{\Phi_b}{k_B T}) \ . \qquad \textbf{(Eq. 6.4)}$$

Here, ?x is the width of the region, which is effective for recombination via a trap state, n_i is the intrinsic density of charge carries, t is the life time of n_i, S_p is the surface recombination velocity, N_V is the effective density of states in the valence band, and F_b is the effective band gap at the interface. F_b is defined as the difference between the Fermi level and the valence band. Let N_d be the density of defect states in the middle of the band gap $E_{g.}$ Then, t ~ N_d^{-1}. If F_b is smaller than E_g and the defect density is below $1{\cdot}10^{17}$ cm^{-3}, then the second term in **(Eq. 6.4)** dominates the saturation current. This case implies that for a low defect concentration the dominant recombination path is located at the interface. For a larger defect density N_d, however, the first term in **(Eq. 6.4)** becomes dominant. Then the main recombination path is in the space charge region. This change in the recombination mechanism requires that the defect density in the bulk exceeds usually determined defect densities of $1{\cdot}10^{16}$ – $1{\cdot}10^{17}$ cm^{-3} [183].

In order to evaluate, how a change of the location of the recombination mechanism might influence the solar cell parameters quantitatively a numerical simulation has been performed. The program SCAPS (Solar Cell Capacitance Simulator) [187] has been used for the simulation. Here, the effective band gap at the interface F_b was taken as 1.3 eV.

In **Tab. 6.4** the results of the numerical simulation are listed. If N_d is between $1{\cdot}10^{16}$ and $1{\cdot}10^{17}$ cm^{-3} then, interface recombination is the dominant recombination mechanism. For defect densities larger than $1 \cdot 10^{18}$ cm^{-3} the location of the recombination changes from the interface to the bulk. For N_d between $1 \cdot 10^{18}$ - $5 \cdot 10^{18}$ cm^{-3} the correlation length has been approximated to 100 - 60 Å. These values correspond well with correlation lengths simulated for micro crystalline Si or GaAs. However, the presented model shows that a change between interface and bulk recombination has a more dramatic effect on the values of j_{sc} than on the values of V_{oc} or FF. For example for $N_d = 5 \cdot 10^{18}$ cm^{-3} the j_{sc} value decreases by more than 40 %, while the decrease of the values of V_{oc} and FF is in the range of 5%. In contrast, for the investigated samples the decrease of both, V_{oc} and FF, is approximately 50% for a comparable diminishing of j_{sc}. The difference between the simulated and measured results might be due to the fact that the simulation is restricted only to the case of thermally activation without considering the effect of tunneling enhanced recombination. This is indeed a strong simplification especially as the results of the jV-analysis of the samples indicate that tunneling processes cannot be neglected (cf. **Fig. 6.11**). Actually, the SCAPS simulation does not reflect the experiments completely.

Tab. 6.4: Influence of the varied defect density on V_{oc}, FF, j_{sc}, and ? determined with SCAPS together with the location of the recombination.

N_d [cm^{-3}]	V_{oc} [mV]	FF [%]	j_{sc} [mA/cm^2]	? [%]	Location of the Recombination
$5 \cdot 10^{16}$	683	77	21.3	11.2	Interface
$1 \cdot 10^{17}$	681	75	20.3	10.4	Interface
$1 \cdot 10^{18}$	669	66	16.3	7.2	Bulk
$5 \cdot 10^{18}$	652	58	12.7	4.8	Bulk

Model 2: Transition from Thermally Activated to Tunneling Enhanced Recombination

In contrast to the first model, the second model describes the influence of an increasing defect density on the recombination rate at the interface. Analysis of the jV-curves revealed for the diode quality factors A and the solar cell parameters the same value of the FWHM as terminating condition. In the presented work diode quality factors A smaller and larger than 2 have been determined. Generally, it is accepted that A values larger than 2 can only be explained by tunneling enhanced recombination [188]. For A values smaller than 2 thermally activated recombination may be prevailing. Based on this background knowledge, we interpret the electric properties of the investigated samples as follows: Some samples show thermally activated interface recombination, while for others tunneling processes are dominant. In **Tab. 6.2** it can be seen that a deterioration of the solar cell performance is combined with increasing A values. Thus, the influence of tunneling is enhanced for devices, which exhibit an inferior solar cell performance. Additionally, the quantum efficiency measurements reveal that a deterioration of the solar cell performance is combined with a worsening of the charge carrier collection. This indicates higher defect concentrations. Moreover, it follows from the PL measurements that a deterioration of the solar cell performance is associated with an increased number of optoelectronic active defect centers. Thus, A values larger than 2 are combined with an increased number of defects. This means that a deterioration of the crystal quality – indicated by the broadening of the Raman line - is combined with an increasing tunneling probability – indicated by A values larger than 2. The saturation of the device quantities for narrow Raman lines can be explained by the same mechanism as for the first model: for these solar cells the effective band gap at the interface is smaller compared to the bulk. This reduced band gap limits the performance.

The main idea of model 2 is the following: For a certain critical density of defects the tunneling enhanced recombination prevails the thermally activated recombination. The contribution of tunneling increases further with an increasing density of defect.

The recombination current j_r can be written as the sum of thermally activated and tunneling enhanced recombination:

$$j_r = qS_p N_V (1+\Gamma)\exp(-\Phi_b / k_B T)\exp(qU / k_B T) \quad . \qquad \textbf{(Eq. 6.5)}$$

S_p is the recombination velocity at the interface, which is determined by the density of defects, N_V is the effective density of states in the valence band, G is the enhanced recombination due to tunneling, and F_b is the effective band gap at the interface. G, in principle, contains the probability of tunneling (P_T) expressed by the energy of the potential barrier for the tunneling process (E_d) and the electric field in the absorber (E). The latter can be expressed by the characteristic tunneling energy (E_{00}). Thus, an increased defect density changes the electric field in the absorber.

Equations **(Eq. 3.16)** and **(Eq. 3.17)** describe the diode quality factors for thermally activated and tunneling enhanced interface recombination. In the case of thermally activation typical values for the diode quality factor are between 1 and 2. For tunneling enhanced recombination A values larger than 2 are obtained. . The diode quality factor is determined by the characteristic tunneling energy (E_{00}). Based on the definition for E_{00} developed by Padovani and Stratton [189] and with **(Eq. 3.17)** it follows that the diode quality factor will exceed 2 if the effective density of acceptors (N_A*) at the interface near region is larger than $5{\cdot}10^{19}$ cm^{-3}. Then, G is significantly larger than 1 and determines j. This case describes the change of j due to additional space charges.

j_r is proportional to N_d/E. In order to describe the change of the recombination current dj_r/j_r caused by the variation of the density of recombination centers dN_d an additional term dN_d/N_d must be introduced. Then, dj_r/j_r is the sum of the spatial gradient of the defect density over all defects with respect to the region of effective recombination, the change of the electric field in the absorber and the absolute change of the defect density.

In **(Eq. 3.18)** an expression for the open circuit voltage for the case of interface recombination is given. The change of V_{oc} in dependence on the change of the density of defects can be expressed by

$$\Delta V_{oc} = -\frac{AkT}{q} \ln \frac{dj_r}{j_r} \qquad . \qquad \textbf{(Eq. 6.6)}$$

This expression is based on the assumption that dj_r/j_r is determined by the absolute change of N_d.

With **(Eq. 3.18)** and **(Eq. 6.6)** it is possible to calculate ?V_{oc} for increasing N_d. The calculated V_{oc} values together with the corresponding defect densities are listed in **Tab. 6.5**. As expected, a significant decrease of the V_{oc} values will occur if N_d increases.

Tab. 6.5: Change in V_{oc} dependent on an increasing defect density N_d.

N_d [cm^{-3}]	$1{\cdot}10^{20}$	$5{\cdot}10^{20}$	$1{\cdot}10^{21}$	$5{\cdot}10^{21}$
?V_{oc}·[mV]	36	103	173	224

In terms of the correlation length, these defect densities correspond to L values between approximately 30 and 10 Å. Compared to L values of other semiconductors these values are significantly too small [176-179]. However, at this point it has to be taken into account that the current interpretation of $CuInS_2$-based heterojunction involves the assumption of a non-homogeneous contribution from the defects. The density of defects is assumed to be around 2 magnitudes higher in the interface near region, i.e. the first 50 nm, than for the deeper part of the absorber. As the information depth revealed with Raman spectroscopy is around 150 nm, the defect densities calculated within the presented model are not the same as those - at least around one order of magnitude -, which determine in the correlation lengths. Therefore it is likely to reevaluate higher values of the correlation length in the range of 100 and 30 Å.

A better approach at this point is to consider multi-step tunneling. It has been shown by Riben and coworkers [190] that multi-step tunneling is more probable than tunneling over a single trap for recombination in the space charge region. For further considerations it is suggested to extend this model to the case of multi-step tunneling from the valence band to the interface. With the assumptions that all traps have the same energetic position within the band gap and the valence band profile remains constant, which means the traps are neutral, the last step of such a multi-step tunneling to the interface determines the entire tunneling process from the valence band to the interfaced. This results in a reduction of the effective tunneling barrier, what leads to an increase of the enhanced recombination due to tunneling G and a more drastic decrease of V_{oc}. Such a model may describe the behavior of V_{oc} more accurate than a one-step tunneling model. However, a quantitative analysis of a multi-step tunneling model would need numerical calculations of the reduced tunneling barrier and G in **(Eq. 6.5)**. In addition, a multi-step tunneling process is characterized by the fact that the diode quality factor is not a function of the temperature [191]. Therefore it is desirable for the future to perform extended numerical calculations and temperature-dependent jV-experiments in order to confirm the results of this study.

In summary, within this chapter the structural quality of absorber layers of $CuInS_2$-based solar cells has been investigated by means of jV-curves, QE, PL and Raman spectroscopy. The broadening of the Raman A_1-mode has been explained with phonon confinement and could be correlated to defect densities within the films. A clear correlation between the preparation conditions of the films and the so determined structural quality on the one hand and a clear correlation between the device performances and the structural quality on the other hand have been found. The later has been discussed on the basis of a defect-density-induced change of the recombination mechanism. The results of this chapter prove that Raman spectroscopy is a powerful tool for in-line quality assurance.

Chapter 7

Conclusion and Outlook

The major focus of this work was on the structural investigation of $CuInS_2$ thin films, which serve as absorber layers in thin film solar cells. Raman spectroscopy has been newly and successfully introduced as an *in-situ* method to investigate the chalcogenization of CuIn precursor layers. Due to its sensitivity for the surface-near region Raman spectroscopy allows the investigation of this region of the $CuInS_2$ absorber, which will determine the device performance after the completion of the device.

Raman experiments allow the identification of different phases within the films. Additionally, it is possible to distinguish between different crystalline phases of the material of interest, for $CuInS_2$ these are the CH- and the CA-phases. Furthermore, the line shape of the Raman bands provides structural information of the observed phase: a spectroscopic broadening of the Raman line is associated with an increasing number of defects in the film.

Earlier *in-situ* XRD experiments on the growth of $CuInS_2$ films revealed that different precursor compositions lead to different phase transformation sequences [154]. Due to the combination of simultaneously performed *in-situ* XRD and *in-situ* Raman measurements, it was possible to confirm and complete previous results. Major differences with respect to the participating phases have been revealed in the phase transformation sequences of Cu-rich and Cu-poor prepared samples. It is verified that the formation of $CuInS_2$ starts at temperatures of approximately 180 °C. Furthermore, it has been confirmed that the growth front of $CuInS_2$ indeed is in direction of the surface normal.

It also has been found that a Cu-S binary phase, which could not previously be detected by XRD, occurs as an intermediate phase directly before the formation of $CuInS_2$ independent from the precursor composition. It is likely that this phase participates in the $CuInS_2$ formation. Furthermore, for the first time experimental evidence is given that the formation of $CuInS_2$ begins with the metastable CuAu crystalline phase, while the formation of the chalcopyrite phase takes place at elevated temperatures only. This behavior has been assigned to a temperature-initiated effect and to the presence of defects in the growing crystals.

Depending on the precursor composition there is a varying amount of the CH-phase in the films and the presence of additional phases participating in the phase transformation sequences. It has been shown that the share of the CH-phase increases with an increasing Cu/In-ratio of the precursors until, for Cu_xIn ($x > 1.2$), no CA-ordered $CuInS_2$ can be detected at the end of the growth process. This has been explained on the basis of an enhanced incorporation of sulfur into the grown films. The main factors which promote the formation of CA-ordered $CuInS_2$ in the films are the temperature and the presence of defects.

A temperature-induced peak shift together with a line broadening of the A_1-mode of chalcopyrite-ordered $CuInS_2$ has been investigated. This allowed the calculation of the corresponding Grüneisen parameter of ? = 1.9 ± 0.1. The determined Grüneisen parameter is in the range of values for other chalcopyrite materials. Its slightly higher value is presumably due to stress within the deposited $CuInS_2$ layers.

For the first time the role of sodium within the growth of Cu-poor precursor layers has been investigated with *in-situ* methods. The following important differences compared to undoped films have been identified during the growth: Due to sodium doping the $CuInS_2$ formation takes place at higher temperatures while the formation of CA-ordered $CuInS_2$ is hindered. This behavior could also be included in the model of enhanced sulfur incorporation into the films. The suppression of the CA-phase due to Na incorporation agrees well with the results of *ex-situ* measurements on epitaxial $CuInSe_2$ thin films [14].

Earlier results showed that the existence of the CA-phase in $CuInS_2$-based solar cells limits the device performance [12]. Based on these results the device qualities of $CuInS_2$-based solar cells which exhibit no or only a small amount of CA-ordered $CuInS_2$ have been investigated with *ex-situ* Raman spectroscopy. The increase of the line width has been interpreted in terms of defect densities. This effect has been embedded in the so-called phonon confinement model developed for silicon [168]. Hence, line broadening is a sensitive indicator for the structural quality of the investigated films.

A clear relationship between the broadening of the Raman line of the $CuInS_2$ A_1-mode and various process parameters has been revealed. This has been included into a model concerning the kinetic limitation of the growth process. Furthermore, a clear relationship between the specific structural properties of $CuInS_2$ and the performance of the completed devices has been found: an increase of the line width of the A_1-mode is accompanied by a decrease of the device performance. This could be correlated with a change in the recombination mechanism. For the interpretation of these relationships two models have been developed which include the recombination mechanism of charge carriers. For the first time the experimental evidence for a relationship between the solar cell performance and the structural properties of the corresponding absorber layers is given.

The investigations presented here demonstrate convincingly the wealth of information that can be deduced from *in-situ* Raman spectroscopy. Besides its contactless and non-destructive character Raman spectroscopy offers the potential to be implemented into an industrial production line for quality assessment. As a result of this study such efforts are in progress.

The presented *in-situ* investigation methods have the potential to provide detailed insight into the reaction paths of the formation of chalcopyrite films. For the future it is an interesting task to investigate the influence of dopants such as Ga and Zn, which have recently been found to increase the open circuit voltage of $CuInS_2$-based solar cells. Also the broadening of the Raman line and its relation to the defect density within the films is a starting point for future research. It would be desirable to identify these defects for example via admittance spectroscopy and thus complete the results of this work.

Appendix

A.1

Cu-S Phase Diagram

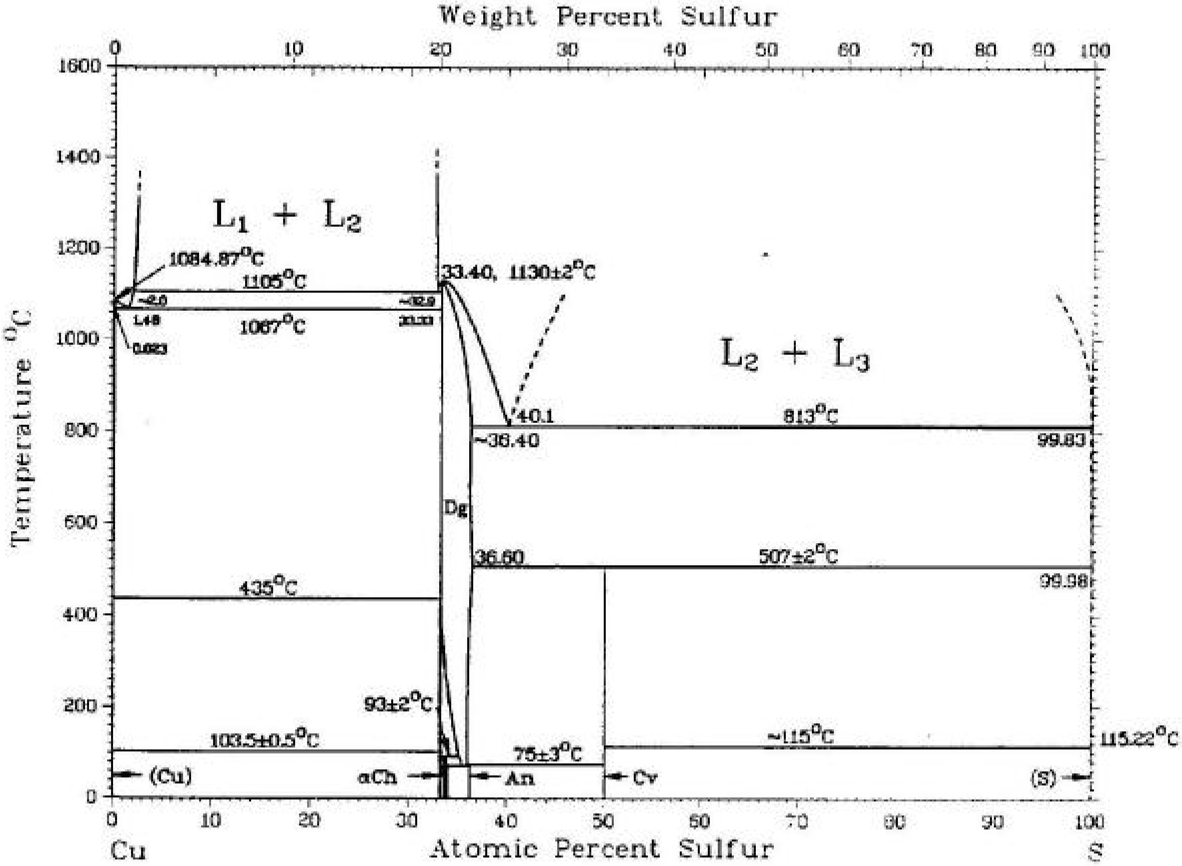

Cu-S phase diagram [192], Cv denotes the phase Covellite, Dg Digenite, An Anilite, Dj Djurleite, and Ch the Chalcocite phases.

A.2

In-S Phase Diagram

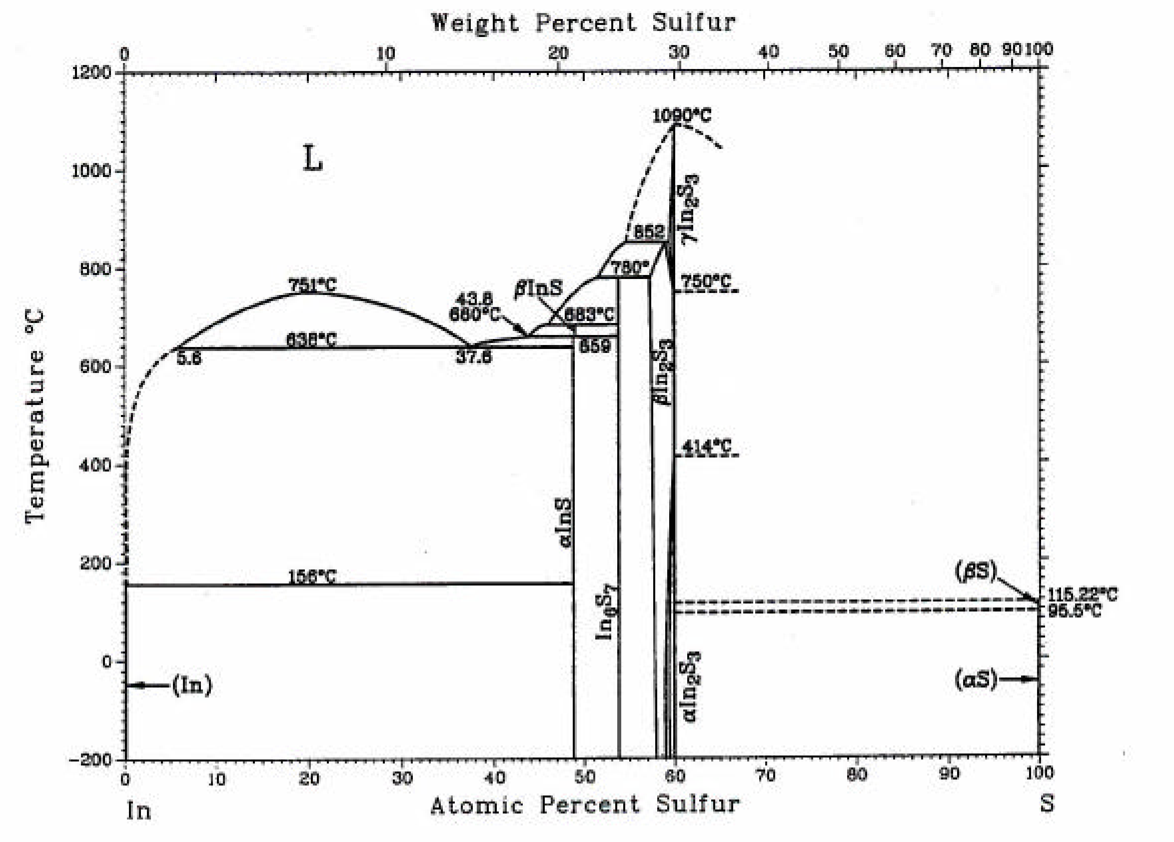

In-S-phase diagram [153]

A.3

Gibbs phase triangle

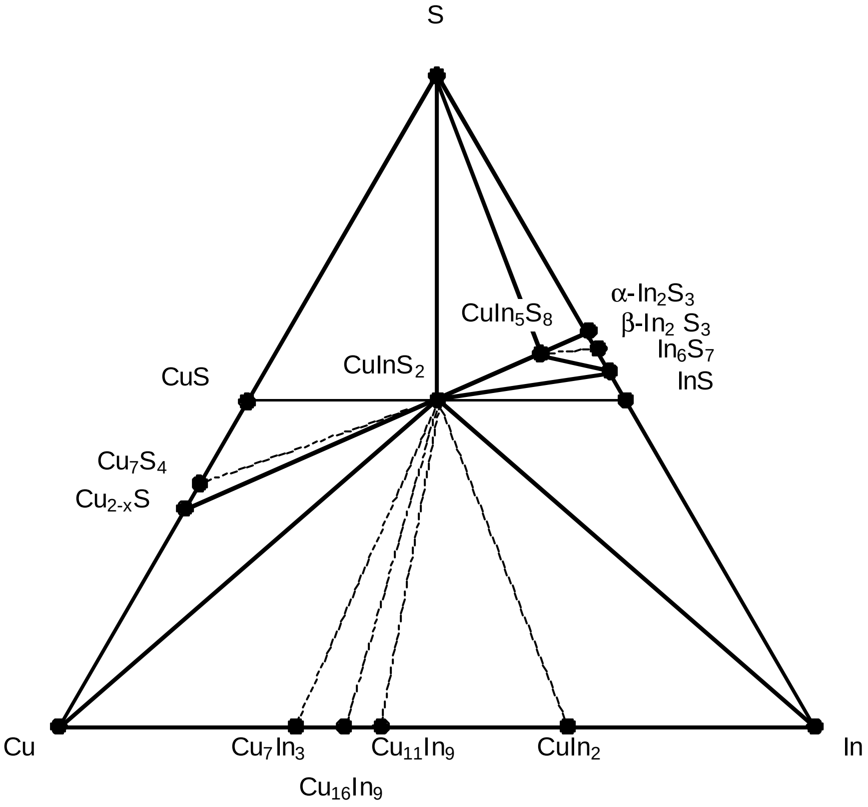

Gibb's phase triangle as projection of all phases between room temperature and 500 °C of the Cu-In-S system [69,70]. The full lines denote measured phase transitions, while the dashed lines denote the derived phase transitions.

Bibliography

1 W. K. Burton, N. Cabrera, and F. C. Frank, Philosophical Transactions of the Royal Society **A 243,** 299 (1951).

2 R. Gay, M. Dietrich, C. Fredric, C. Jensen, K. Knapp, D. Tarrant, and D. Willett, in *Efficiency and process improvements in CuInSe2 based modules*, Amsterdam, 1994 (H.S. Stephens & Associates), p. 935.

3 M. C. Lux-Steiner, A. Ennaoui, C. H. Fischer, A. Jäger-Waldau, J. Klaer, R. Klenk, R. Könenkamp, T. Matthes, R. Scheer., S. Siebentritt, and A. Weidinger, Thin Solid Films **361-362,** 533-539 (2000).

4 M. A. Contreras, personal communication; (2003).

5 V. Probst, F. Karg, J. Rimmasch, W. Riedl, W. Stetter, H. Harms, and O. Eibl, in *Advenced stacked elemental layer process for Cu(In,Ga)Se2 thin film photovoltaic devices*, San Francisco, USA, 1996 (MRS, Pittsburgh), p. 165.

6 J. Klaer, J. Bruns, R. Henninger, K. Siemer, R. Klenk, K. Ellmer, and D. Bräunig, Semiconductor Science and Technology **13,** 1456 (1998).

7 J. Klaer, I. Luck, A. Boden, R. Klenk, I. Gavilanez-Perez, and R. Scheer, Thin Solid Films **431-432,** 534-537 (2003).

8 Sulfurcell, www.Sulfurcell.de (2003).

9 I. Luck, J. Kneisel, K. Siemer, J. Bruns, R. Scheer, R. Klenk, N. Janke, and D. Bräunig, Solar Energy Materials and Solar Cells **67,** 151-158 (2001).

10 S.-H. Wei, L. G. Ferreira, and A. Zunger, Physical Review B **45,** 2533 (1992).

11 S.-H. Wei, S. B. Zhang, and A. Zunger, Physical Review B **59,** R2478 (1999).

12 J. Alvarez-Garcia, E. Rudigier, N. Rega, B. Barcones, R. Scheer, A. Pérez-Rodríguez, A. Romano-Rodríguez, and J. R. Morante, Thin Solid Films **431-432,** 122 (2003).

13 T. Watanabe, h. Nakazawa, and M. Matsui, Japanese Journal of Applied Physics **37,** L1370-L1372 (1998).

14 B. J. Stanbery, Kincal, S., Kim, S., Anderson, T.J., Crisalle, O.D., Ahrenkiel, S.P., Lippold, G., IEEE**,** 440-445 (2000).

15 J. Alvarez-Garcia, A. Perez-Roddriguez, B. Barcones, A. Romano-Rodriguez, J. R. Morante, A. Janotti, S.-H. Wei, and R. Scheer, Applied Physics Letters **80,** 562 (2002).

16 M. Kuball, Surface and Interface Analysis **31,** 987 (2001).

17 B. Roughani, M Kallergi, J. Aubel, and S. Sundaram, J.Appl.Phys. **66,** 4946 (1989).

18 T. Ganguli and A. Ingale, Physical Review B **60,** 11618 (1999).

19 C. V. Raman and K. S. Krishnan, Nature **121,** 501 (1928).

20 A. Smekal, Naturwissenschaften **16,** 557 (1923).

[21] M. Born and K. Huang, in *Dynamical Theory of Crystal Lattices* (Clarendon Press, Oxford, 1954).

[22] W. Hayes and R. Loudon, *Scattering of Light by Crystals* (Wiley, New York, 1978).

[23] A. Pinczuk and E. Burstein, in *Light scattering in solids I: Introductory Concepts*; *Vol. 2*, edited by M. Cardona (Springer, Berlin, 1982).

[24] D. P. Strommen and K. Nakamoto, in *Laboratory Raman Spectroscopy*, edited by Wiley (New York, 1984).

[25] W. Demtröder, *Atome, Moleküle und Festkörper*, Vol. 3 (Springer-Verlag, Berlin Heidelberg, 1996).

[26] G. F. Koster, in *Solid State Physics 5* (Academic Press, New York, 1957), p. 173.

[27] H. Callen, American Journal of Physics **36,** 735 (1968).

[28] J. Menendez, in *Raman Scattering in Materials Science*, edited by W. H. Weber and R. Merlin (Springer Press, Heidelberg, 2000).

[29] R. W. G. Wyckoff, *Crystal Structure*, Vol. 1, 2nd ed. (Wiley, New York, 1964).

[30] T. Hahn, (Ed.), in *International Tables for Crystallographiy*; *Vol. A*, 2nd ed. (Kluwer Academic Press, London, 1989).

[31] D. L. Rousseau, R. P. Baumann, and S. P. S. Porto, Journal of Raman Spectroscopy **10,** 253 (1981).

[32] A. Debernardi, Physical Review B **57,** 12847 (1998).

[33] A. Debernardi, S. Baroni, and E. Molinari, in *22nd International Conference on the Physics of Semiconductors*, edited by D. J. Lockwood (World scientific, Vancouver, 1994), p. 373.

[34] A. Debernardi, S. Baroni, and E. Molinari, Physical Review Letters **75,** 1819 (1995).

[35] S. Hunklinger, *Festkörperphysik* (Ruprecht-Karls University, Heidelberg, 1999).

[36] P. G. Klemens, Physical Review **148,** 845 (1966).

[37] R. A. Cowley, Journal de Physique **26,** 659 (1965).

[38] J. Menendez and M. Cardona, Physical Review B **29,** 2051 (1984).

[39] J. Serrano, M. Cardona, T. M. Ritter, B. A. Weinstein, A. Rubio, and C. T. Lin, Physical Review B **66,** 245202 (2002).

[40] E. Anastassakis and E. Burstein, Journal of Physics and Chemistry of Solids **32,** 563 (1971).

[41] E. Anastassakis and M. Cardona, in *High Pressure in Semiconductor Physics II*; *Vol. 55*, edited by T. Suski and W. Paul (Academic Press, New York, 1998).

[42] R. Merlin, A. Pinczuk, and W. H. Weber, in *Raman Scattering in Materials Science*, edited by W. H. Weber and R. Merlin (Springer Press, Heidelberg, 2000).

[43] A. S. Barker and A. J. Sievers, Reviews of Modern Physics **47,** Suppl. No. 2, S1 (1975).

[44] JCPDS, (Picot, Pierrot, Bull. Soc. Fr. Mineral. Cristallogr., 86 7 (1963)).

[45] J. E. Jaffe and A. Zunger, Phys.Rev.B **28,** 5822 (1983).

[46] J. E. Jaffe and A. Zunger, Physical Review B **27,** 5176 (1983).

[47] J. E. Jaffe and A. Zunger, Phys.Rev.B **29,** 1882 (1984).

[48] Alonso, Wakita, Pascual, Garriga, and Yamamoto, Physical Review B **63,** 1-13 (1984).

[49] W. Cochran, Journal of Physics and Chemistry of Solids **8,** 405 (1959).

[50] M. J. P. Musgrave and J. A. Pople, Proc. of the Royal Society (London) Seria A **268,** 474 (1962).

[51] M. Cardona and G. Güntherodt, *light scattering in solids II* (Springer Press Heidelberg, New York, 1982).

[52] H. Matsushita, S. Endo, and T. Irie, Japanese Journal of Applied Physics **31,** 18 (1992).

[53] J. Camassel, L. Artus, and J. Pascual, Physical Review B **41,** 5717 (1990).

[54] G. D. Holah, J. S. Webb, and H. Montgomery, Journal of Physics C **7,** 3875 (1974).

[55] W. Cochran, Philosophical Magacine **4,** 1082 (1959).

[56] G. Dolling and R. A. Cowley, Proc. of the Royal Society (London) **88,** 463 (1966).

[57] M. A. Nusimovici and J. L. Birman, Physical Review B **156,** 925 (1967).

[58] L. Artus, J. Pascual, J. Pujol, J. Camassel, and R. S. Feigelson, Physical Review B **43,** 2088 (1991).

[59] L. Artus and J. Pascual, Journal of Physics: Condensed Matter **4,** 5835 (1992).

[60] P. N. Keating, Physical Review **145,** 637 (1966).

[61] H. Neumann, Helvetica Physica Acta **58,** 337 (1985).

[62] J. Lazewski, P. T. Jochym, and K. Parlinski, Journal of Chemical Physics **117,** 2726 (2002).

[63] J. Lazewski, K. Parlinski, B. Hennion, and R. Fouret, Journal of Physics: Condensed Matter **11,** 9665 (1999).

[64] W. H. Koschel and M. Bettini, physica status solidi (b) **72,** 729 (1975).

[65] F. W. Ohrendorf and H. Haeuseler, Crystal Research and Technology **34,** 339-349 (1999).

[66] M. Saad, S. Bleyhl, T. Ohashi, Y. Hashimoto, K. Ito, B. Mertesacker, A. Jäger-Waldau, W. Woletz, and M.-C. Lux-Steiner, 2nd World Conference on Photovoltaic Solar Energy Conversion **1,** 1149 (1998).

[67] R. Bacewicz, W. Gebicki, and J. Filipowicz, Journal of Physics: Condensed Matter **6,** L777 (1994).

[68] C. Rincon, S. M. Wasim, G. Marin, J. M. Delgado, J. R. Huntzinger, A. Zwick, and J. Galibert, Applied Physics Letters **73,** 441 (1998).

[69] H. Metzner, M. Brüssler, K.-D. Husemann, and H. J. Lewerenz, Phys. Rev. B **44,** 11614 (1991).

[70] H. Metzner, Physical Review B **38** (1988).

[71] C. Rincon, Physical Review B **45,** 12716 (1991).

[72] A. Zunger and J. E. Jaffe.

[73] W. Borchardt-Ott, *Kristallographie* (Springer Press Heidelberg, 1997).

[74] D. S. Su and S. H. Wei, Applied Physics Letters **74,** 2483 (1999).

[75] S. H. Wei and A. Zunger, Applied Physics Letters **56,** 662 (1990).

[76] D. S. Su, W. Neumann, R. Hunger, P. Schubert-Bischoff, M. Giersig, H. J. Lewerenz, R. Scheer, and E. Zeitler, Applied Physics Letters **73,** 785 (1998).

[77] D. S. Su, W. Neumann, and M. Giersig, Thin Solid Films **361-362,** 218 (2000).

[78] A. Gomyo, T. Suzuki, K. Kobayashi, S. Kawata, and I. Hino, Appl. Phys. Lett. **50,** 673 (1987).

[79] S. Froyen and A. Zunger, Physical Review B **53,** 4570 (1996).

[80] G. Morell, R. S. Katiyar, S. Z. Weisz, T. Walter, H. W. Schock, and I. Balberg, Applied Physics Letters **69,** 987 (1996).

[81] K. Kambas, J. Spyridelis, and M. Balkanski, Physica Status Solidi (b) **105,** 291-296 (1981).

[82] H. Metzner, T. Hahn, J.-H. Bremer, and J. Conrad, Applied Physics Letters **69,** 1900 (1996).

[83] K.-I. Kondo, S. Nakamura, and K. Sato, Japanese Journal of Applied Physics **37,** 5728 (1998).

[84] T. Riedle, PhD-Thesis, Technical University, 2002.

[85] W. Shockley, Bell System Technical Journal**,** 435-589 (1949).

[86] I. Hengel, PhD Thesis, Freie Universität Berlin, 2000.

[87] U. Blieske, V. Dieterle, I. Hengel, C. Kaufmann, R. Klenk, and M. C. Lux-Steiner, in *Proccedings 14 th EPVSEC*, Barcelona, 1997 (H.S. Stephens & Associates), p. 2135.

[88] R. Klenk, P. Dobson, M. Falz, N. Janke, J. Klaer, I. Luck, A. Pérez-Rodríguez, A. Romano-Rodríguez, R. Scheer, and E. Terzini, in *SULFURCELL: Efficient Thin Film Solar Cells Based on CuInS2*, Glasgow, 2000 (James&James), p. 325.

[89] K. Siemer, J. Klaer, I. Luck, J. Bruns, R. Klenk, and D. Bräunig, Solar Energy Materials and Solar Cells **67,** 159-166 (2001).

[90] T. Watanabe, H. Nakazawa, and M. Matsui, Japanese Journal of Applied Physics **37,** L1370-L1372 (1998).

[91] T. Watanabe, H. Nakazawa, M. Matsui, H. Ohbo, and T. Nakada, Solar Energy Materials and Solar Cells **49,** 357-363 (1997).

[92] T. Watanabe and M. Matsui, Japanese Journal of Applied Physics **38,** L1379 (1999).

[93] R. Scheer, M. Alt, I. Luck, and H. J. Lewerenz, Solar Energy Materials and Solar Cells **49,** 423 (1997).

[94] D. Braunger, S. Zweigart, and H. W. Schock, in *Proccedings of 2nd WPVSEC*, Vienna, 1998.

[95] B. R. Pamplin, Journal de Physique Colloque C3, supplément au n° **9,** Tome 36, 53 (1975).

[96] S. B. Zhang, S.-H. Wei, and A. Zunger, Physical Review Letters **78,** 4059 (1997).

[97] S. B. Zhang, S.-H. Wei, and A. Zunger, Journal of Applied Physics **83,** 3192 (1997).

[98] A. Klein and W. Jaegermann, Applied Physics Letters **74,** 2283 (1999).

[99] I. Hengel, R. Klenk, E. G. Villora, and M. C. Lux-Steiner, in *Proceedings of 2nd WPVSEC*, Vienna, 1998 (Stephens), p. 545.

[100] N. G. Dhere and S. R. Ghongadi, in *Proceedings of Materials Research Society Symposium*, 2001, p. H3.4.1.

[101] A. Neisser, Dissertation Thesis, FU Berlin, 2001.

[102] I. Luck, Dissertation Thesis, Freie Universität, 1998.

[103] R. Klenk, Thin Solid Films **387,** 135-140 (2001).

[104] D. Braunger, T. Dürr, D. Hariskos, C. Köble, T. Walter, N. Wieser, and H. W. Schock, in *Proceedings of 25th PVSC*, Washington, D.C., 1996, p. 1001.

[105] D. Braunger, D. Hariskos, T. Walter, and H. W. Schock, Solar Energy Materials and Solar Cells **40,** 97-102 (1996).

[106] R. Bayón, J. Herrero, and J. Klaer, in *Proceedings of 16th EPVSEC*, Glasgow, 2000 (James&James), p. 875.

[107] A. Chaparo, R. Bayón, M. T. Gutiérrez, J. Herrero, J. Klaer, K. Siemer, and D. Bräunig, in *Proceedings of 16th EPVSEC*, Glasgow, 2000 (James&James), p. 867.

[108] H. Y. Ueng and H. L. Hwang, J.Phys.Chem.Solids **50,** 1297 (1989).

[109] H. J. Lewerenz and N. Dietz, Journal of Applied Physics **73,** 4975 (1993).

[110] H. Y. Ueng and H. L. Hwang, J.Appl.Phys. **62,** 434 (1987).

[111] J. J. M. Binsma, Journal of Physics and Chemistry of Solids **44,** 237-244 (1983).

[112] J. J. Binsma, L. J. Giling, and J. Bloem, J. Luminesc. **27,** 35 (1982).

[113] F. A. Kröger, *The chemistry of imperfect crystals*, Vol. 1 (North-Holland Publishing Company, Amsterdam, 1974).

[114] S. B. Zhang, S.-H. Wei, A. Zunger, and H. Katayama-Yoshida, Physical Review B **57,** 9642 (1998).

[115] S. M. Sze, *Physics of Semiconductor Devices* (Wiley-Interscience, New-York, 1981).

[116] U. Rau, Applied Physics Letters **74,** 111 (1999).

[117] U. Rau, A. Jasenek, H. W. Schock, J. Engelhardt, and T. Meyer, Thin Solid Films **361-362,** 298 (2000).

[118] V. Nadenau, U. Rau, A. Jasenek, and H.-W. Schock, Journal of Applied Physics **87,** 584-593 (2000).

[119] J. Reiss, PhD Thesis, Freie Universität Berlin, 2002.

[120] K. Siemer, J. Klaer, I. Luck, J. Álvarez-García, A. Pérez-Rodríguez, A. Romano-Rodríguez, and D. Bräunig, in *Growth monitoring of CuInS2 absorber layers prepared by a Rapid Thermal Process (RTP)*, Glasgow, 2000 (James&James), p. 895.

[121] J. Klaer, J. Bruns, R. Henninger, K. Töpper, R. Klenk, K. Ellmer, and D. Bräunig, in *A tolerant two step process for efficient $CuInS_2$ solar cells*, Vienna, 1998 (Stephens), p. 537.

[122] J. Klaer, J. Bruns, R. Henninger, M. Weber, R. Klenk, K. Ellmer, R. Scheer, and D. Bräunig, in *CuInS2 Solar Cells From Sputtered CuIn Precursors reacted in Sulphur Vapouer*, Barcelona, Spain, 1997, p. 1307-1310.

[123] J. Klaer, J. Bruns, R. Henninger, R. Klenk, K. Ellmer, R. Scheer, and D. Bräunig, in *CuInS2 solar cells prepared by a sequential process using sulphur vapour*, Salford, 1997 (Inst.Phys.Conf.Ser), p. 963-966.

[124] K. Ellmer, R. Mientus, V. Weiß, and H. Rossner, Nuclear Instruments and Methods in Physics Research A **467-468,** 1041-1044 (2001).

[125] J. W. Otto, Nuclear Instruments and Methods in Physics Research A **384,** 552-557 (1997).

[126] G. F. Knoll, *Radiation detection and measurement*, 2.ed ed. (Wiley, New York, 1989).

[127] C. L. Schoen, S. K. Sharma, C. E. Helsley, and H. Owen, Applied Spectroscopy **47,** 305-308 (1993).

[128] D. A. Long, *Raman Spectroscopy* (McGraw-Hill, New, York, 1977).

[129] R. L. McCreery, *Modern Techniques in Raman Spectroscopy, Instrumentation for dispersive Raman Spectroscopy* (J.J. Laserna, Wiley, New York, 1996).

[130] K. Siemer, PhD Thesis, Freie Universität Berlin, 2000.

[131] J. Alvarez-Garcia, PhD-Thesis, Universitat de Barcelona, 2002.

[132] I. V. Bodnar and N. S. Orlova, Physica Status Solidi (a) **78,** K59-K63 (1983).

[133] H. Tanino, T. Maeda, H. Fujikake, H. Nakanishi, S. Endo, and T. Irie, Physical Review B **45,** 13323 (1992).

[134] M. Bettini and W. B. Holzapfel, Solid State Communications **16,** 27 (1975).

[135] C. Carlone, D. Olego, A. Jayaraman, and M. Cardona, Physical Review B **22,** 3877 (1980).

[136] M. S. Liu, L. A. Bursill, S. Prawer, K. W. Nugent, Y. Z. Tong, and G. Y. Zhang, Applied Physics Letters **74,** 3125 (1999).

[137] J. Gonzalez, M. Quintero, and C. Rincon, Physical Review B **45,** 7022-7025 (1991).

[138] K. J. Bachmann, F. S. L. Hau, F. A. Thiel, and H. M. Kasper, Journal of Electronic Materials **6,** 431 (1977).

[139] S. Shirakata, Japanese Journal of Applied Physics **27,** 2113 (1988).

[140] T. R. Hart, R. L. Aggarwal, and B. Lax, Physical Review B **1,** 638 (1970).

[141] M. Balkanski, R. F. Wallis, and E. Haro, Physical Review B **28,** 1928 (1983).

[142] J. B. Cui, K. Amtmann, J. Ristein, and L. Ley, J.Appl.Phys. **83,** 7929 (1998).

[143] W. J. Borer, S. S. Mitra, and K. V. Namjoshi, Solid State Communications **9,** 1377 (19761).

[144] B. Barcones, personal communiaction; (2003).

[145] B. Barcones, E. Rudigier, J. Djordjevic, A. Pérez-Rodríguez, L. Calvo-Barrio, A. Romano-Rodríguez, J. R. Morante, I. Luck, and R. Scheer, submitted (2004).

[146] S. M. Peiris, J. S. Sweeney, A. S. Campbell, and D. L. Heinz, Journal of Chemical Physics **104,** 11 (1996).

[147] H. Fjellvåg, F. Grønvold, S. Stølen, A. F. Andresen, R. Müller-Käfer, and A. Simon, Zeitschrift für Kristallographie **184,** 111-121 (1988).

[148] B. J. Wuensch, *Determination, Relationships, and Classification of Mineral Structures*, Vol. 1 (Book Crafters, Chelsea, 1974).

[149] W. Liang and M.-H. Whangbo, Solid State Communications **85,** 405-408 (1993).

[150] D. J. Chakrabarti and D. E. Laughlin, Bulletin of Alloy Phase Diagrams **4,** 254 (1983).

[151] C. Pietzker, J. Djordjevic, E. Rudigier, and R. Scheer, submitted (2004).

[152] P. B. Barton, Jr., Economic Geology **68,** 455-465 (1973).

[153] Okamoto, Binary Alloy Phase Diagrams**,** 2283-2285 (1983).

[154] C. Pietzker, E. Rudigier, D. Bräunig, and R. Scheer, in *Laser Light Scattering and Real-Time XRD Studies on the Sequential Formation of CuInS$_2$ Films:Towards a Simple and Stable Process Control*, Munich, Germany, 2001 (WIP-Renewable Energies ETA), p. 1031-1034.

[155] W. Keppner, T. Klas, W. Körner, R. Wesche, and G. Schatz, Physical Review Letters **54,** 2371-2374 (1985).

[156] R. Scheer and H. J. Lewerenz, Journal of Vacuum Science and Technology A **13,** 1924 (1995).

[157] M. R. Balboul, Turcu, M., Kötschau, I. M., Rau, U., Schock, H.-W.,**,** (2003).

[158] R. Klenk, T. Walter, H. W. Schock, and D. Cahen, Solid State Phenomena **37-38,** 509 (1994).

[159] R. Klenk, PhD Thesis, Universität Stuttgart, 1993.

[160] A. J. Nelson, G. S. Horner, K. Sinha, and M. H. Bode, Appl. Phys. Lett. **64,** 3600 (1994).

[161] A. N. Tiwari, S. Blunier, M. Filzmoser, H. Zogg, D. Schmid, and H. W. Schock, Appl. Phys. Lett. **65,** 3347 (1994).

[162] H. Z. Xiao, L.-C. Yang, and A. Rockett, Journal of Applied Physics **76,** 1503 (1994).

[163] G. Morell, R. S. Katiyar, S. Z. Weisz, T. Walter, H.-W. Schock, and I. Balberg, Applied Physics Letters **69,** 987 (1996).

[164] T. Tanaka, Toshiyuki, Yamaguchi, Akira, Yoshida, in *Influence of incorporation of Na on CuInSe2 thin films*, Salford, 1998 (IOP Publishing), p. 329-332.

[165] K. Fukuzaki, S. Kohiki, H. Yoshikawa, S. Fukushima, T. Watanbe, and I. Kojima, Applied Physics Letters **73,** 1385 (1998).

[166] S. H. Lee and et al., J.Appl.Phys. **85,** 3590 (1999).

[167] D. Wolf and G. Müller, Japanese Journal of Applied Physics **39,** 173 (2000).

[168] H. Richter, Z. P. Wang, and L. Ley, Solid State Communications **39,** 625 (1981).

[169] J. Alvarez-Garcia, A. Perez-Rodriguez, A. Romano-Rodriguez, J. R. Morante, L. Calvo-Barrio, R. Scheer, and R. Klenk, Journal of Vacuum Science and Technology A **19,** 232-239 (2001).

[170] J. Álvarez-García, A. Pérez-Rodríguez, A. Romano-Rodríguez, T. Jawhari, J. R. Morante, R. Scheer, and W. Calvet, Thin Solid Films **387,** 216-218 (2001).

[171] T. Hahn, H. Metzner, B. Plikat, and M. Seibt, Thin Solid Films **387,** 83 (2001).

[172] K. Töpper, Diploma Thesis, Technische Universität, 1996.

[173] A. Meeder, D. Fuertes Marron, V. Chu, J. P. Conde, A. Jäger-Waldau, A. Rumberg, and M. C. Lux-Steiner, Thin Solid Films **403-404,** 495 (2002).

[174] C.-H. Chang, S.-H. Wei, S. P. Ahrenkiel, J. W. Johnson, B. J. Stanbery, T. J. Anderson, S. B. Zhang, M. M. Al-Jassim, G. Bunker, E. A. Payzant, and R. Duran, Materials Research Society Symposium Proceedings **V668** (2001).

[175] F. H. Pollak and R. Tsu, SPIE Proceedings **452,** 26 (1983).

[176] J. W. Ager III, D. Kirk Veirs, and G. M. Rosenblatt, Physical Review B **43,** 6491 (1991).

[177] Y. A. Pusep, M. T. O. Silva, J. C. Galzerani, N. T. Moshegov, and P. Basmaji, Physical Review B **58,** 10683-10686 (1998).

[178] Y. T. Hou, Z. C. Feng, M. F. Li, and S. J. Chua, Surface and Interface Analysis **28,** 163-165 (1999).

[179] A. K. Arora, T. R. Ravindran, G. L. N. Reddy, A. K. Sikder, and D. S. Misra, Diamond and related materials **10,** 1477-1485 (2001).

[180] S. Sadewasser, T. Glatzel, S. Schuler, S. Nishiwaki, R. Kaigawa, and M. C. Lux-Steiner, Thin Solid Films (2002).

[181] D. Wolf and G. Müller, Thin Solid Films **361-362,** 155-60 (2000).

[182] C. Pietzker, PhD Thesis, University of Potsdam, 2003.

[183] R. Klenk,; (2004).

[184] J. Reiss, J. Malmström, A. Werner, I. Hengel, R. Klenk, and M. C. Lux-Steiner, in *Current transport in CuInS2 solar cells depending on absorber preparation*, San Francisco, 2001.

[185] K. Ito, N. Matsumoto, T. Horiuchi, K. Ichino, H. Shimoyama, T. Ohashi, Y. Hashimoto, I. Hengel, J. Beier, R. Klenk, A. Jäger-Waldau, and M.-C. Lux-Steiner, Japanese Journal of Applied Physics **39,** 126 (2000).

[186] K. Siemer, J. Kneisel, I. Luck, J. Klaer, R. Scheer, R. Klenk, and D. Bräunig, Japanese Journal of Applied Physics **39,** 270 (2000).

[187] M. Burgelman, P. Nollet, and S. Degrave, in *Modeling Polycrystalline Semiconductor Solar Cells*, Strasbourg, France, 1999.

[188] U. Rau, Applied Physics Letters **74,** 111-113 (1998).

[189] F. A. Padovani and R. Stratton, Solid State Electron. **9,** 605 (1966).

[190] A. R. Riben and D. L. Feucht, Solid-State Electronics **9,** 1055 (1966).

[191] H. Matsuura, T. Okuno, H. Okushi, and K. Tanaka, J.Appl.Phys. **55,** 1012 (1983).

[192] P. K. Nair, M. T. S. Nair, H. M. K. K. Pathirana, R. A. Zingaro, and E. A. Meyers, Journal of the Electrochemical Society **140,** 754-759 (1993).

Abbreviations

CA	CuAu phase
CCD	Charge coupled device
CH	Chalcopyrite
CTP	Conventional thermal processing
DESY	Deutsches Elektron Synchrotron
EDXRD	Energy Dispersive X-Ray Diffraction
HASYLAB	Hamburger Synchrotron Laboratory
IR	Infra-red active
NDC	Neutral-defect-complexes
OVC	Ordered Vacancy Compound
R	Raman active
RTP	Rapid thermal processing
SPM	Semi-permeable membrane
XRD	X-ray diffraction

Publications

Parts of this work have been already published:

Journal Publications

- C. Pietzker, E. Rudigier, D. Bräunig, and R. Scheer, Munich, Germany, 2001 (WIP-Renewable Energies ETA), p. 1031-1034.
- J. Alvarez-Garcia, E. Rudigier, N. Rega, B. Barcones, R. Scheer, A. Pérez-Rodríguez, A. Romano-Rodríguez, and J. R. Morante, Thin Solid Films 431-432, 122 (2003).
- E. Rudigier, Pietzker, C., Wimbor, M., Luck, I., Klaer, J., Scheer, R., Barcones, B., Jawhari Colin, T., Alvarez-Garcia, J., Perez-Rodriguez, A., Romano-Perez, A., Thin Solid Films 431-432, 110-115 (2003).
- E. Rudigier, Alvarez-Garcia, J., Luck, I., Klaer, J., Scheer, R., Journal of Physics and Chemistry of Solids 64, 1977-1981 (2003).
- E. Rudigier, Luck, I., Scheer, R., Applied Physics Letters 82, 4370-4372 (2003).
- B. Barcones, A. Pérez-Rodríguez, A. Romano-Rodríguez, J. R. Morante, E. Rudigier, I. Luck, J. Djordjevic, and R. Scheer, Journal of Applied Physics submitted (2004).
- E. Rudigier, B. Barcones, I. Luck, T. Jawhari-Colin, A. Pérez-Rodríguez, and R. Scheer, Journal of Applied Physics 95, 51513 (2004).

Patent application:

- DE 10248504A1

Curriculum vitae

Eveline Rudigier

1994-2000	student of physics at the Karl-Ruprecht university Heidelberg
1997-1998	interdisciplinary supplement study Environmental Science, Heidelberg
December 2000	university graduation: Diplom-Physikerin, final thesis: *Entwicklung eines automatisierten Bildverarbeitungssystems zur Auswertung unregelmäßiger Bildpunkte auf DNA-Chips* at the DKFZ Heidelberg
2001-2004	PhD student at the Hahn-Meitner Institut Berlin